CHALMERS UNIVERSITY OF TECHNOLOGY

Two Equation Turbulence Models for Swirling Flow

by

Rickard Bergström

Thesis for the degree of
Master of Science in Engineering Physics
at
Chalmers University of Technology, Göteborg, Sweden

Göteborg, October 1997

Abstract

The aim of this work is to give a survey of some of the more popular two-equation turbulence models and to try to decide which of them that is the most suitable for swirling flow cases. The survey includes the standard $k - \epsilon$ model with and without wall functions, the Richardson number correction, the RNG-$k - \epsilon$ model with and without swirl modification, the Wilcox $k - \omega$ model and finally a non-linear $k - \omega$ model.

A brief theoritical background is given both for the treatment of the governing equations and for the different turbulence models. All equations, constants and different types of limiters needed to make the models work are also described.

The computations have been done for an idealized, axisymmetric LPP burner with annular inlet and outlet. Two flow cases are included, one with a moderate swirl number of 0.40 and one with relatively high swirl number of 0.95. The numerical method used is an explicit three stage Runge-Kutta time marching method with finite volume discretization in space. The code has been developed and validated at Volvo Aero Corporation.

Great care has been taken to isolate the effects of the models and minimize and document the numerical error.

The computations have shown that the RNG-$k - \epsilon$ model together with the $k - \omega$ models yield good results. The standard $k - \epsilon$ model without wall functions should not be used as it yields non-acceptible results. The use of wall functions improves performance, but not enough to compete with the RNG-$k - \epsilon$ or the $k - \omega$ models. The annular outlet has caused difficulties in the form of a central vortex that the models are not able to predict.

Acknowledgements

This work has been carried out at Volvo Aero Corporation in Trollhättan and all members of the CFD group has contributed by sharing their time and knowledge.

Especially, I would like to thank my advisors Lars-Erik Eriksson and Peter Emvin. Lars-Erik helped me getting started with the code and various aspects of implementing the models. Peter has assisted me with all kinds of practical problems. Both have had valuable comments and contributions concerning how the models and the numerics work and which conclusions to draw from the results.

At Chalmers University of Technology, I want to thank Jonas Larsson and Andrei Smirnoff at the Department of Thermo and Fluid Dynamics for their help with finding information concerning some of the more advanced models.

Nomenclature

C_p	Specific heat at constant pressure [J/kgK]
e	Internal energy [J/kg]
e_0	Total energy [J/kg]
h	Enthalpy [J/kg]
k	Turbulent kinetic energy [J]
Pr	Prandtl number [-]
q_i	Heat-flux vector [W/m^2]
R	Specific gas constant [J/kgK]
s_{ij}	Strain rate tensor [s^{-1}]
t_{ij}	Newtonian shear stress tensor [N/m^2]
u_i	Velocity vector [m/s]
u_τ	Friction velocity [m/s]
δ_{ij}	Kronecker's delta function [-]
ϵ	Dissipation of k [J/kgs]
μ	Dynamic viscosity [Ns/m^2]
μ_T	Eddy viscosity [Ns/m^2]
ρ	Density [kg/m^3]
τ_{ij}	Reynolds stress tensor [N/m^2]
ω	Specific dissipation rate [s^{-1}]
l	Characteristic length scale [m]
U	Characteristis velocity scale [m/s]
$\overline{\Phi}, \Phi$	Reynolds averaged quantity
$\tilde{\Phi}, \Phi$	Favre averaged quantity
Φ', ϕ	Reynolds fluctuating part
Φ'', ϕ	Favre fluctuating part

Contents

1 Introduction

The interest in low-emission gas turbines has grown recently, mostly for environmental reasons. The main goal is to develop burners for civilian applications that minimize the emissions of NO_X. Different forms of NO_X are important in many environmental problems, mainly the acid rains but also the increasing greenhouse effect and the ozone layer depletion. However, also for military aircraft engines there is an interest to minimize the emission because this affects the possibility to detect the aircraft. The hot emissions give the aircraft a characteristic IR signal which is not wanted.

One way to achieve this is to use a LPP combustor[1]. LPP is an abbreviation for Lean Premixed/Prevaporized which indicates that the fuel is mixed with air and vaporized before injected into the combustor. An important part in this type of combustor is the use of swirlers to set the fluid in rotation. The swirl has the effect of stabilizing the flame to prevent blow-out and it creates a recirculation zone which is important for lowering the NO_X emissions. The recirculation zone gives a longer residence time in the combustor which makes it possible to use a lower temperature which in turn yields less NO_X[2].

When developing new types of burners, the use of numerical calculations has become an important tool. Computational Fluid Dynamics (CFD) has made it possible to predict some effects of changing the combustor design and therefore diminish the need for high cost, time consuming component tests. As the computers become more powerful and the algorithms develop, CFD will become more accurate and it will become possible to use numerical predictions in more cases than today.

There are three main elements in CFD: grid generation, algorithm development and turbulence modelling[3]. The turbulence is an essential feature of almost all engineering flow cases and the need for a robust, fast and accurate turbulence model is crucial when using CFD as a design tool.

Historically, the concept of eddy viscosity introduced by Boussinesq in 1877 has been the foundation for most of the attempts made to model the physics of turbulence. Excluding the non-linear $k - \omega$ model, all the models tested in this work are based on this concept, even if they may differ strongly in other aspects. Attempts have been made to model the transport of the Reynolds stresses instead of using the eddy viscosity, but these models are still too cumbersome and prone to breakdone to use in engineering applications.

The flow in a LPP burner is dominated by the swirl which yields effects that the standard turbulence model, the $k - \epsilon$ model, cannot cope with. This model is tuned for plane flow with homogenoues turbulence. The aim of this work is to find a model that treats swirling flow better than the $k - \epsilon$ model and is yet fast, robust and simple to implement.

2 Modelling the Turbulence

2.1 Governing Equations

With the available computer power of today it is not possible to solve the instantaneous Navier-Stokes equations for high Reynolds number turbulent flow, the resolution needed is too high. Instead, the equations are averaged to get rid of the smallest scales of the flow. This can be done in two ways, according to Reynolds

$$\begin{aligned} \overline{\Phi} &\stackrel{def}{=} \frac{1}{T}\int_t^{t+T} \Phi(t)dt \\ \Phi' &\stackrel{def}{=} \Phi - \overline{\Phi} \end{aligned} \tag{1}$$

and according to Favre

$$\begin{aligned} \tilde{\Phi} &\stackrel{def}{=} \frac{\overline{\rho\Phi}}{\overline{\rho}} \\ \Phi'' &\stackrel{def}{=} \Phi - \tilde{\Phi} \end{aligned} \tag{2}$$

With this definition $\overline{\Phi'} = 0$, but $\overline{\Phi''} \neq 0$.

The Reynolds averaging is used to take care of fluctuations in velocity and in pressure, while the Favre averaging accounts for fluctuations in density and in temperature. For incompressible flow only Reynolds averaging is done, but in compressible flow the density and temperature fluctuations are large and Favre averaging is used.

Using this averaging procedure by decomposing the variables into mean and fluctuating parts and introducing the assumptions of a perfect, monoatomic gas, the Favre averaged equations governing compressible flow can be written[3]

$$\frac{\partial\overline{\rho}}{\partial t} + \frac{\partial}{\partial x_i}(\overline{\rho}\tilde{u_i}) = 0 \tag{3}$$

$$\frac{\partial}{\partial t}(\overline{\rho}\tilde{u_i}) + \frac{\partial}{\partial x_j}(\overline{\rho}\tilde{u_j}\tilde{u_i}) = -\frac{\partial\overline{P}}{\partial x_i} + \frac{\partial}{\partial x_j}\left[\overline{t_{ij}} + \tau_{ij}\right] \tag{4}$$

$$\begin{aligned} \frac{\partial}{\partial t}(\overline{\rho}\tilde{e_0}) + \frac{\partial}{\partial x_j}(\overline{\rho}\tilde{u_j}\tilde{h_0}) &= \frac{\partial}{\partial x_j}\left[-q_{L_j} - q_{T_j} + \overline{t_{ij}u_j''} - \overline{\rho u_j''\frac{1}{2}u_i''u_i''}\right] + \\ &\quad -\frac{\partial}{\partial x_j}\left[\tilde{u_i}(\overline{t_{ij}} + \tau_{ij})\right] \end{aligned} \tag{5}$$

where

$$t_{ij} = \mu(2s_{ij} - \frac{2}{3}\frac{\partial u_k}{\partial x_k}\delta_{ij}) \tag{6}$$

$$\begin{aligned}
\tau_{ij} &= -\overline{\rho u_i' u_j'} && (7)\\
\tilde{e_0} &= \tilde{e} + \frac{1}{2}\tilde{u_i}\tilde{u_i} + k && (8)\\
\tilde{h_0} &= \tilde{h} + \frac{1}{2}\tilde{u_i}\tilde{u_i} + k && (9)\\
q_{L_j} &= -C_p \frac{\mu}{Pr_L}\frac{\partial \tilde{T}}{\partial x_j} && (10)\\
q_{T_j} &= C_p \overline{\rho u_j'' T} && (11)\\
P &= \overline{\rho} R \tilde{T} && (12)\\
& && (13)
\end{aligned}$$

Neglecting the terms arising due to small density fluctuations, i.e. the third and fourth terms of the right hand side of (5), two terms in these equations remain unknown and need to be modelled.

- The Reynolds stress tensor, τ_{ij}, which is discussed in the following section.
- The turbulent transport of heat, q_{T_j}, which is usually modelled with a gradient approximation, analogous to the laminar heat transport

$$q_{T_j} = -C_p \frac{\mu}{Pr_T}\frac{\partial \tilde{T}}{\partial x_j} \tag{14}$$

where the turbulent Prandtl number is set to 0.9.

For simplicity, the overbars and tildes will be omitted and averaged quantaties will be written in capital letters while fluctuating quantities will be indicated with a prime.

2.2 Boussinesq Hypothesis

The most used way to model the Reynolds stress tensor is to write it as the product of a turbulent eddy viscosity and the mean strain rate tensor, i.e.,

$$\tau_{ij} = \mu_T(2S_{ij} - \frac{\partial U_k}{\partial x_k}\delta_{ij}) - \frac{2}{3}\rho k \delta_{ij} \tag{15}$$

where the third term on the right is included to get the right trace.

This idea is known as the Boussinesq hypothesis. To understand the motivation of this approximation, one can study the analogy between turbulent and molecular momentum transport as presented by, e.g., Tennekes and Lumley[4]. However, this analogy must be considered with caution as molecules and turbulent eddies are fundamentally different physical phenomena. The most obvious difference is that the molecular viscosity is a property of the fluid, and as such known a priori, whereas the turbulent viscosity depends on the particular flow.

Therefore, this assumptions does not seem to help much as the constant μ_T depends on the flow and is still unknown. Different assumptions concerning μ_T have been made over the years to close the averaged equations and in this work I have studied the family of models that are known as two-equation models.

2.3 Two-equation Turbulence Models

By dimensional analysis, one sees that one way to obtain an expression for μ_T is by combining suitable length and velocity scales to get

$$\mu_T = C_\mu \rho l U \tag{16}$$

Two things need to be known to be able to calculate μ_T: a characteristic velocity and a characteristic length. The most common choice for the velocity scale is to choose

$$U = \sqrt{k} \tag{17}$$

where k is the kinetic energy of the turbulent velocity fluctuations

$$k = \frac{1}{2}(\overline{u'^2} + \overline{v'^2} + \overline{w'^2}) \tag{18}$$

Deriving an exact transport equation for k is a rather straightforward matter of algebra[5][4]. The resulting equation is

$$\rho\frac{\partial k}{\partial t} + \rho U_j \frac{\partial k}{\partial x_j} = \tau_{ij}\frac{\partial U_i}{\partial x_j} - \rho\epsilon + \frac{\partial}{\partial x_j}\left[\mu\frac{\partial k}{\partial x_j} - \frac{1}{2}\overline{\rho u_i' u_i' u_j'} - \overline{p' u_j'}\right] \tag{19}$$

The quantity called ϵ is the dissipation per unit mass and is defined by

$$\rho\epsilon = \mu\overline{\frac{\partial u_i'}{\partial x_k}\frac{\partial u_j'}{\partial x_k}} \tag{20}$$

In order to be able to solve this equation we need to model several of the terms.

The Reynolds stress tensor is usually modelled by the Boussinesq approximation (15) for the two-equation models studied in this work. The exception is the non-linear $k-\omega$ model which models this term with a more complex expression. Using this, we can model the first term on the left, the production term.

Assuming the dissipation and the turbulent length scale to be functions of turbulent quantities only and not of the mean flow quantities, the dissipation ϵ can be expressed as

$$\epsilon \sim \frac{k^{3/2}}{l} \tag{21}$$

Hence, an expression for the length scale l is still needed to model this term.

The last two terms on the right hand side are still unknown and are modelled by a gradient diffusion assumption for the turbulent transport, while the pressure diffusion is neglected as direct numerical simulations has shown it to be small. Thus, we get

$$\frac{1}{2}\overline{\rho u_i' u_i' u_j'} + \overline{p' u_j'} = -\frac{\mu_T}{\sigma_k}\frac{\partial k}{\partial x_j} \tag{22}$$

where σ_k is a closure coefficient.

The resulting equation needed to solve thus becomes

$$\rho\frac{\partial k}{\partial t} + \rho U_j \frac{\partial k}{\partial x_j} = \tau_{ij}\frac{\partial U_i}{\partial x_j} - \rho\epsilon + \frac{\partial}{\partial x_j}\left[(\mu + \frac{\mu_T}{\sigma_k})\frac{\partial k}{\partial x_j}\right] \tag{23}$$

where τ_{ij} is given by (15).

In order to obtain a second equation, several suggestions on the choice of variable equivalent to l have been presented in the literature. The two most common variants are to solve for the dissipation, ϵ, or the specific dissipation rate, ω. On dimensional grounds, the eddy viscosity μ_T, dissipation ϵ, turbulent kinetic energy k, dissipation rate ω and turbulent length scale l are related as

$$\mu_T \sim \frac{\rho k}{\omega}, \quad l \sim \frac{k^{1/2}}{\omega}, \quad \epsilon \sim \omega k \tag{24}$$

More details concerning the different variants of the second equation are given in the following sections.

The two equations discussed above, equation (23) for k and one equation for l or an equivalent variable, together with a constituitive relation for the eddy viscosity, e.g. (15), form a two-equation turbulence model.

2.3.1 Swirl Modifications

Due to the rotation of the fluid, the swirl affects the turbulence by imposing an additional rate of strain. In flows with sudden changes in the mean rate of strain, certain history effects causes the Reynolds stresses to adjust slower than the mean strain rate, they react to this so called extra rate of strain. Models based on the Boussinesq hypothesis cannot, as the Reynolds stresses are modelled to be proportional to the mean strain rate, catch these effects. Therefore, these models generally show a rather poor behaviour for flows with curvature effects.

Consequently, modifications to the popular $k-\epsilon$ model have been proposed which deal with this kind of problems. These corrections consist of modifying either the source term of the ϵ-equation or the constant of proportionality, C_μ , between μ_T and l and U. Examples of both are included in the work through the Richardson number correction, which modifies the ϵ-equation source term, and the RNG-$k-\epsilon$ with swirl modifications to C_μ.

2.3.2 $k-\epsilon$ Model

This model, first introduced in this form by Jones and Launder, has become a standard in turbulence modelling. It is robust and gives quite good results in some flow cases. One drawback is that it is tuned for homogeneous turbulence, which is not the case in many flows, e.g. swirling flow. Another thing that this model has been critized for is the lack of physical basis in the assumed closure approximations for the ϵ-equation. However, this model will be considered the basic two-equation model and used for comparison with the other models. The model is:

$$\rho\frac{\partial k}{\partial t} + \rho U_j\frac{\partial k}{\partial x_j} = \tau_{ij}\frac{\partial U_i}{\partial x_j} - \rho\epsilon + \frac{\partial}{\partial x_j}\left[(\mu + \frac{\mu_T}{\sigma_k})\frac{\partial k}{\partial x_j}\right] \tag{25}$$

$$\rho\frac{\partial \epsilon}{\partial t} + \rho U_j\frac{\partial \epsilon}{\partial x_j} = C_{\epsilon 1}\frac{\epsilon}{k}\tau_{ij}\frac{\partial U_i}{\partial x_j} - C_{\epsilon 2}\rho\frac{\epsilon^2}{k} + \frac{\partial}{\partial x_j}\left[(\mu + \frac{\mu_T}{\sigma_\epsilon})\frac{\partial \epsilon}{\partial x_j}\right] \tag{26}$$

$$\mu_T = \rho C_\mu\frac{k^2}{\epsilon} \tag{27}$$

C_μ	σ_k	σ_ϵ	$C_{\epsilon 1}$	$C_{\epsilon 2}$
0.09	1.0	1.3	1.44	1.92

Table 1: Constants of the standard $k-\epsilon$ model.

In this form, the model is not valid close to a solid surface. In order to overcome this deficiency, many implementations uses wall functions to specify the values in the cells closest to the wall. This is done by matching the law of the wall

$$\frac{U}{u_\tau} = \frac{1}{\kappa}\ln\frac{u_\tau y\rho}{\mu} + 5.0 \tag{28}$$

with the mean velocity which yields for k and ϵ

$$k = \frac{{u_\tau}^2}{\sqrt{C_\mu}} \tag{29}$$

$$\epsilon = {C_\mu}^{3/4}\frac{k^{3/2}}{\kappa y} \tag{30}$$

where u_τ is the friction velocity and $\kappa = 0.41$ is the von Kármán constant.

This has been implemented in the model and evaluated together with the other models.

2.3.3 $k - \omega$ Model

The variable ω can be interpreted in more than one way. When Kolmogorov developed the first two-equation model in 1942, he chose k and ω as parameters and described ω as the rate of dissipation of energy per unit volume and time. Later, it has been identified as the enstrophy, i.e. the RMS value of the fluctuating vorticity. In the most used form of this model, Wilcox regards ω as the ratio of ϵ to k, i.e., the rate of dissipation per unit turbulent kinetic energy. This standard $k - \omega$ model is:

$$\rho\frac{\partial k}{\partial t} + \rho U_j\frac{\partial k}{\partial x_j} = \tau_{ij}\frac{\partial U_i}{\partial x_j} - \beta^*\rho k\omega + \frac{\partial}{\partial x_j}\left[(\mu + \sigma^*\mu_T)\frac{\partial k}{\partial x_j}\right] \tag{31}$$

$$\rho\frac{\partial \omega}{\partial t} + \rho U_j\frac{\partial \omega}{\partial x_j} = \alpha\frac{\omega}{k}\tau_{ij}\frac{\partial U_i}{\partial x_j} - \beta\rho\omega^2 + \frac{\partial}{\partial x_j}\left[(\mu + \sigma\mu_T)\frac{\partial \omega}{\partial x_j}\right] \tag{32}$$

$$\mu_T = \rho\frac{k}{\omega} \tag{33}$$

α	β	β^*	σ	σ^*
5/9	3/40	9/100	1/2	1/2

Table 2: Constants of the Wilcox $k - \omega$ model.

It is not necessary to use wall functions as this model can be used also in the boundary layer close to a surface. However, wall functions reduce the number of nodes and therefore also the computation time. In this work, resolved boundary layers have been used and not wall functions.

2.3.4 Richardson Number Correction

Originally, the Richardson number was used to represent the ratio of buoyancy to inertia forces, but due to the analogy between buoyancy and streamline curvature forces the expression is used also in this context. The idea is then to use the fact that for a confined swirling flow the solid body rotation stabilizes the turbulence intensity, while a free vortex profile acts destabilizing[6]. Thus, the Richardson number correction is designed to modify the source in the ϵ-equation of the standard $k-\epsilon$ model in a way that reflects these effects. The Richardson number used in this work has the form

$$\mathrm{Ri} = \frac{2(\frac{1}{r}\frac{\partial}{\partial r}(rW))\frac{W}{r}}{\frac{\partial U}{\partial r}^2 + (\frac{\partial W}{\partial r} + \frac{W}{r})^2} \tag{34}$$

This results in the following new ϵ-equation

$$\rho\frac{\partial \epsilon}{\partial t} + \rho U_j \frac{\partial \epsilon}{\partial x_j} = C_{\epsilon 1}\frac{\epsilon}{k}\tau_{ij}\frac{\partial U_i}{\partial x_j} - C_{\epsilon 2}(1 - C_g \mathrm{Ri})\rho\frac{\epsilon^2}{k} + \frac{\partial}{\partial x_j}\left[(\mu + \frac{\mu_T}{\sigma_\epsilon})\frac{\partial \epsilon}{\partial x_j}\right] \tag{35}$$

which together with (25),(27) and (34) yields the model. The constant C_g is recommended to lie in the interval [0.002,0.008].

However, we can see that the Richardson number becomes unbounded on the singular line and that the source term may change sign for large values of Ri, which is not realistic. Hence it is necessary to take care of these problems by some kind of limiters on Ri.

2.3.5 Renormalisation Group Theory

The RNG methods form a group of models where complex dynamics of a system is described by equations governing the large-scale, "coarse-grained" behaviour of the system. Thus, the RNG methods describe how to systematically remove the small scales in the system. In terms of turbulence modelling this means that we filter the small, turbulent scales and get a description of the physics on a level where the phenomena are resolvable with the computer power available. The resulting model is very similar to the standard $k-\epsilon$ model, but the constants are slightly modified and an extra source term in the ϵ-equation has been added. The set of equations is

$$[h]\rho\frac{\partial k}{\partial t} + \rho U_j \frac{\partial k}{\partial x_j} = \mu_{eff} S^{*2} - \rho\epsilon + \frac{\partial}{\partial x_j}\left[\alpha\mu_{eff}\frac{\partial k}{\partial x_j}\right] \tag{36}$$

$$\rho\frac{\partial \epsilon}{\partial t} + \rho U_j \frac{\partial \epsilon}{\partial x_j} = C_{\epsilon 1}\frac{\epsilon}{k}\mu_{eff} S^{*2} - C_{\epsilon 2}\rho\frac{\epsilon^2}{k} - R + \frac{\partial}{\partial x_j}\left[\alpha\mu_{eff}\frac{\partial \epsilon}{\partial x_j}\right] \tag{37}$$

$$\tag{38}$$

where

$$\mu_{eff} = \mu\left[1 + k\sqrt{\frac{\rho C_\mu}{\mu\epsilon}}\right]^2 \tag{39}$$

$$R = \frac{C_\mu \eta^3 (1-\eta/\eta_0)}{1+\beta\eta^3}\frac{\epsilon^2}{k} \tag{40}$$

$$\eta = S^* \frac{k}{\epsilon} \tag{41}$$

$$S^* \stackrel{def}{=} \sqrt{2 S^*_{ij} S^*_{ij}} \tag{42}$$

$$S^*_{ij} \stackrel{def}{=} S_{ij} - \frac{1}{3} S_{ij}\delta_{ij} \tag{43}$$

C_μ	β	η_0	$C_{\epsilon 1}$	$C_{\epsilon 2}$	α
0.0845	0.012	4.38	1.42	1.68	1.39

Table 3: Constants of the RNG-$k-\epsilon$ model.

Please note that μ_{eff} replaces the sum $\mu + \mu_T$ also in the momentum equations.

The advantages using this this model are two. First, the ϵ-equation is given a more firm theoretical basis than in the standard $k-\epsilon$ formulation, and second, the extra source term makes the model more sensitive to rapid straining flows. The R term catches some of the history effects mentioned earlier and is responsible for a large improvement for a wide range of more complex flows.

The model can be further modified for swirling flow by using an expression for C_μ that includes the effects of the streamline curvature. The expression used in this work has the following form[2][7][8]

$$C_\mu = \frac{0.09}{\left[1 + 8{K_1}^2 \frac{k^2}{\epsilon^2}(\frac{\partial U_s}{\partial n} + \frac{U_s}{R_c})\frac{U_s}{R_c}\right]} \tag{44}$$

where $K_1 = 0.2667$, R_c is the local radius of curvature and s and n refers to the local streamline coordinate system as the streamline and normal directions. In order to avoid unphysical equations, a bound on C_μ is needed. Thus the constant is limited to the interval [0.025,0.09].

This modification is extracted from an algebraic stress formulation and simplified to isolate the effect of the extra curvature-strain rate on C_μ. One starts from the equations governing the transport of the Reynolds stresses. By assuming local stress equilibrium one can omit all transport terms and get an algebraic stress equation. This relation is transformed to the local streamline coordinate system and simplified to represent only the relation between the shear stress and the mean rate of strain, giving (44)[7].

2.3.6 Non-linear Models

One basic deficiency of the discussed models is that they all are based on the linear Boussinesq hypothesis. An approach of dealing with this problem is to work with a non-linear relation between the Reynolds stresses and the velocity gradients. The model considered here is developed by Larsson[9] following the methods of Shih and Reynolds[10]. A truncated second order expression for the Reynolds stresses is obtained using dimensional analysis. This expression is then simplified using different mathematical and physical constraints. This model, cast in a $k-\omega$ framework, becomes

$$\begin{aligned}
\rho\frac{\partial k}{\partial t}+\rho U_j\frac{\partial k}{\partial x_j} &= \tau_{ij}\frac{\partial U_i}{\partial x_j}-\beta^*\rho k\omega+\frac{\partial}{\partial x_j}\left[(\mu+\sigma^*\mu_T)\frac{\partial k}{\partial x_j}\right] && (45)\\
\rho\frac{\partial \omega}{\partial t}+\rho U_j\frac{\partial \omega}{\partial x_j} &= \alpha\frac{\omega}{k}\tau_{ij}\frac{\partial U_i}{\partial x_j}-\beta\rho\omega^2+\frac{\partial}{\partial x_j}\left[(\mu+\sigma\mu_T)\frac{\partial \omega}{\partial x_j}\right] && (46)\\
\mu_T &= C_\mu\rho kT && (47)\\
\tau_{ij} &= -\frac{2}{3}k\delta_{ij}+C_\mu\rho k2TS^*_{ij}+ \\
&\quad -C_2\rho k2T^2(-S^*_{ik}\Omega^*_{kj}+\Omega^*_{ik}S^*_{kj}) && (48)\\
T &\stackrel{def}{=} \frac{1}{\beta^*\omega}=\frac{k}{\epsilon}
\end{aligned}$$

$$\begin{aligned}
S^*_{ij} &\stackrel{def}{=} S_{ij}-\frac{1}{3}S_{ij}\delta_{ij} & \Omega^*_{ij} &\stackrel{def}{=} \Omega_{ij}\\
U^* &\stackrel{def}{=} \sqrt{S^*_{ij}S^*_{ij}+\Omega^*_{ij}\Omega^*_{ij}} & S^* &\stackrel{def}{=} \sqrt{S^*_{ij}S^*_{ij}}\\
\Omega^* &\stackrel{def}{=} \sqrt{\Omega^*_{ij}\Omega^*_{ij}} & W^* &\stackrel{def}{=} \frac{S^*_{ij}S^*_{jk}S^*_{ki}}{(S^*)^3}\\
C_\mu &= \frac{1}{A_0+A^*_sU^*T} & C_2 &= \frac{\sqrt{1-(3C_\mu S^*T)^2}}{C_0+6S^*\Omega^*T^2}\\
A^*_s &= \sqrt{6}\cos\phi_1 & \phi_1 &= \frac{1}{3}\arccos\sqrt{6}W^*
\end{aligned}$$

3 Numerical Method

The solver used in this work is developed by Lars-Erik Eriksson at Volvo Aero Corporation[11]. The numerical method is an explicit three stage Runge-Kutta time marching method that uses an optimized local time-step. Third and second order finite volume schemes are used for the Euler and the viscous parts respectively, with upwind corrections based on characteristic variables. A limiter is used when solving for the more sensitive turbulent quantities. For a more detailed discussion of the codes, see [11] and [12].

3.1 Finite Volume Formulation of the Equations

When working with finite volume methods, it is suitable to write the equations on conservative form. A compact notation of the equations is

$$\frac{\partial Q}{\partial t} + \frac{\partial F_j}{\partial x_j} = S \tag{49}$$

where Q is the state vector to be solved for, F_j is the flux vector and S is the source term vector. They have the form

$$Q = \begin{bmatrix} \rho \\ \rho U_i \\ \rho e_0 \\ \rho k \\ \rho \epsilon \end{bmatrix}, F_j = \begin{bmatrix} \rho U_j \\ \rho U_i U_j + P\delta_{ij} - (T_{ij} + \tau_{ij}) \\ (\rho e_0 + P)U_j + q_j - u_i(T_{ij} + \tau_{ij}) \\ \rho k U_j + d_j^{(k)} \\ \rho \epsilon U_j + d_j^{(\epsilon)} \end{bmatrix}, S = \begin{bmatrix} 0 \\ 0 \\ 0 \\ s^{(k)} \\ s^{(\epsilon)} \end{bmatrix} \tag{50}$$

The Reynolds stress tensor (τ_{ij}), the diffusion terms ($d_j^{(k)}$ and $d_j^{(\epsilon)}$) and the source terms ($s^{(k)}$and $s^{(\epsilon)}$) are specified according to the different turbulence models described in the previous section.

These seven equations are discretized on a non-orthogonal block-structured boundary fitted mesh using a cell centered finite volume scheme. Integrating equation (49) over a control volume yields

$$\int_\Omega \frac{\partial Q}{\partial t}\, dV + \int_\Omega \frac{\partial F_j}{\partial x_j}\, dV = \int_\Omega S\, dV \tag{51}$$

Assuming a stationary grid, Gauss' theorem makes it possible to rewrite the equation as

$$\frac{\partial}{\partial t}\int_\Omega Q\, dV + \int_{\partial\Omega} F_j \cdot dS_j = \int_\Omega S\, dV \tag{52}$$

This equation tells us that the rate of change of the state vector is equal to the sum of the fluxes over the boundaries plus the source term. Defining the cell centered averages of Q and S as

$$\overline{Q} \stackrel{def}{=} \frac{1}{V} \int_{\Omega} Q \, dV \tag{53}$$

$$\overline{S} \stackrel{def}{=} \frac{1}{V} \int_{\Omega} S \, dV \tag{54}$$

where

$$V = \int_{\Omega} dV \tag{55}$$

the equation becomes

$$V \frac{\partial}{\partial t}(\overline{Q}) + \int_{\partial\Omega} F_j \cdot dS_j = V\overline{S} \tag{56}$$

Using the approximation

$$\overline{S} = S(\overline{Q}) \tag{57}$$

and assuming F_j to be constant on each cell wall the discretized equations become

$$V \frac{\partial}{\partial t}(\overline{Q}) + \sum_{faces} F_j^{faces} \cdot S_j^{faces} = V\overline{S} \tag{58}$$

3.1.1 Convective Terms

For these terms a theoretically third order upwind scheme has been used. By working with the characteristic variables the direction of the upwinding is determined by the sign of the eigenvalues. A TVD limiter is used for the k and the ϵ equations. The TVD limiter and use of a non-cartesian mesh yield in practice a lower order scheme than a third order.

3.1.2 Diffusive Terms

In order to calculate the diffusive flux, approximations of the primitive variables, as well as their derivatives, are needed at the cell faces. The primitive variables are estimated by a simple average of the two neighbouring cell values, and the gradients are calculated with a scheme centered around the face. Theoretically these approximations are of second order.

3.1.3 Source Terms

To calculate the source terms the approximation (57) is used. Besides this, the gradients that are needed are approximated using the cell-centered finite volume scheme

$$\left(\frac{\partial q}{\partial x_i}\right)^{cell} = \frac{1}{V}\int_\Omega \frac{\partial q}{\partial x_i}\, dV = \frac{1}{V}\int_{\partial\Omega} q\, dS_i = \frac{1}{V}\sum_{faces} q \cdot S_i \tag{59}$$

Also in this case, the scheme is of second order.

3.1.4 Time Integration

To march in time, a three stage explicit Runge-Kutta scheme with optimized local time-step is used. The described space-discretization yields a set of equation that can be written

$$V \cdot \frac{\Delta Q}{\Delta t} = S_{term} - F_{term} \tag{60}$$

where S is the source terms and F is the fluxes. From Q^n, Q^{n+1} is calculated in three steps according to

$$Q^* = Q^n + \Delta t \cdot V \cdot (S_{term} - F_{term})|_{Q^n} \tag{61}$$

$$Q^{**} = \frac{1}{2}Q^n + \frac{1}{2}Q^* + \frac{1}{2}\Delta t \cdot V \cdot (S_{term} - F_{term})|_{Q^*} \tag{62}$$

$$Q^{n+1} = \frac{1}{2}Q^n + \frac{1}{2}Q^* + \frac{1}{2}\Delta t \cdot V \cdot (S_{term} - F_{term})|_{Q^{**}} \tag{63}$$

The local time step is determined from a local stability estimate.

3.2 Implementing the Turbulence Models

In most cases the different variations to the $k-\epsilon$ model only needed small modifications in the code. The only exceptions were the non-linear $k-\omega$ model and the swirl modification used in RNG $k-\epsilon$. When implementing the non-linear $k-\omega$ model Mathematica was used to get the complicated non-linear terms correct. The possibility to generate Fortran code in Mathematica was invaluable when working with this model. The swirl correction needed a transformation to the local streamline coordinate system to obtain the local radius of curvature and the derivative normal to the streamline. A fair amount of vector analysis was needed to calculate this transformation, but the implementation caused no problems.

3.3 Stability Aspects and Accuracy of the Solutions

In order to avoid divergence caused by stability problems certain care may need to be taken during the first iterations, especially in the equations for the turbulence model. In most cases I used the standard $k-\epsilon$ model to reach an acceptable solution and then used this solution when starting to use the other models. The non-linear $k-\omega$ model is roughly as stable as the standard $k-\omega$ model[9].

To be sure of convergence, consecutive solutions were plotted with a certain number of iterations between and when the differences were no longer noticable, they were considered converged. The effect of the swirl is significant on the convergence rate, it was necessary to increase the number of iterations by a factor of five to ten to what could be expected otherwise.

Mesh dependence was tested by comparing the converged solution to one made on another grid. To be able to make a correct evaluation of the models it is important to know wether observed differences are caused by numerical errors and not by the models themselves. Assuming that the error is of second order, which is reasonable since the viscous terms dominate in the equations, a detailed analysis using Richardson extrapolation gives an expression for the error E_h as[3]

$$E_h \approx \frac{1}{3}|(u_h - u_{2h})| \tag{64}$$

where the subscript h denotes the grid size. However, this has not been done in this work. Evaluation has been done by inspection and (64) has only been used as rule of thumb when considering mesh independence.

4 Test Case

4.1 Validation Test Facility

The measurements used to validate the CFD solutions were made in an idealized ax-isymmetric LPP burner at Karlsruhe University[13]. The test facility consists of a cylinder with annular inlet and outlet. The geometry of the burner is given in figure 1. For more details concerning the measurement methods used, see [14][15].

4.2 Inlet and Outlet Conditions

All mean velocity components were given together with the six velocity correlations, which made the definition of the inlet conditions easy. The only problem was to define an inlet condition for the dissipation and a suitable outlet condition. Even if the velocity and the turbulent kinetic energy were given exactly where the inlet reaches the cylinder,

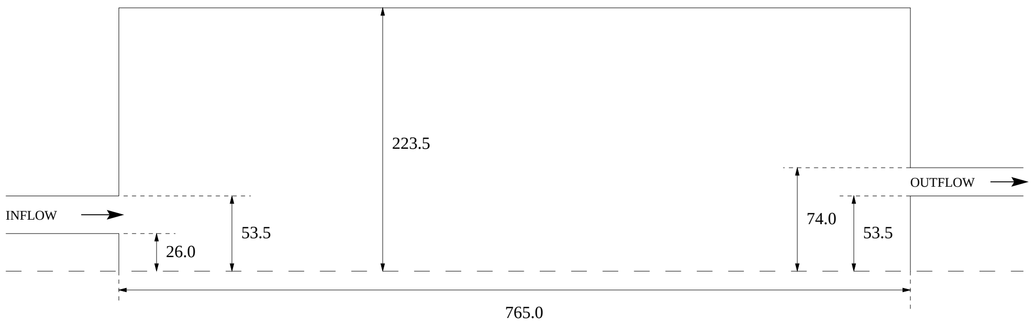

Figure 1: Geometry of the LPP burner

I decided to start the calculations a distance of 25 mm upstream in the annular inlet. This was done to allow a dissipation field to develop. The inlet dissipation was then set according to expression (65), derived from energy equilibrium assumptions[16],

$$\epsilon = \frac{k^{3/2}}{\alpha R} \tag{65}$$

where R is the radius of the cumbustor chamber and $\alpha = 0.36$ is a constant. Furthermore, the radial velocity was set to zero while the other velocity components was just transported upstream. There was no need to adjust the velocities to get the right profile on entering the cylinder.

At the outlet a constant pressure was set a distance of 235 mm downstream from the combustor.

4.3 Computational Mesh

I used two different meshes for my calculations and two more for testing the grid dependence. One mesh was used for all the $k-\epsilon$ models, but since the $k-\omega$ models need resolved boundary layers, grid points were added when constructing this mesh. The four meshes used are shown in figures 2 – 5. The meshes are slighty finer at the inlet as this part of the combustor is considered to influence the flow pattern the most. This may not be totally true as the annular outlet accelerates the flow before the exit, which obviuosly influences the flow upstream. There are reasons to believe that this causes the central vortex that is present not only in the flow with the stronger swirl, but also in the flow with swirl number $S = 0.40$. Though, the difference in grid size between the inlet and outlet section is not that large and does probably not influence the flow significantly.

When constructing the coarse mesh for the the $k - \epsilon$ models, care was taken to get the same resolution in the boundary layer. This was done to separate the numerical error in the interior of the combustor from the errors due to the grid in the wall region where grid independence may not be expected.

5 Results

5.1 General Computational Aspects

The presence of the swirl caused several minor practical problems. The time to reach a converged solution increased considerably. The required number of iterations had to be increased by a factor of five to ten. The explicit time marching method is slow but robust so no problem with stability arised.

Furthermore, the swirling flow solutions are known to be more sensitive to the mesh used[17]. Rather dense meshes were therefore used from the start. This eliminated the problem with numerical errors obscuring model effects. Comparison of solutions made on different meshes shows good agreement, even if it is clear that a finer mesh yields a solution that is closer to the measured data. In figure 6 the largest deviations between different meshes are shown. The dotted line shows a solution with different wall resolution from the other two. The solid and the dashed lines show solutions where the grid density is the same in the wall region but the dashed are coarser in the interior. Hence, the treatment near the wall affected the solution strongly, but the numerical error in the interior is not a large problem. In the case of these two profiles the numerical error may be of the same size as the difference between two similar models, c.f. the dashed and the solid lines in figure 6 with the corresponding figures 15 and 18 in appendix. However, the evaluation has been done on a larger set of data so this will not hinder correct conclusions.

As mentioned above, for the standard mesh and the coarse mesh the boundary layer resolution used was approximately the same, while for the finer mesh the resolution was considerably higher. Theoretically the error is of second order so the deviations between the standard and the fine mesh should be smaller than between the standard and the coarse mesh. As this was not the case, the conclusion is that the resolution near the wall has a large influence on the accuracy of the solution. The importance of the wall is confirmed by the higher accuracy reached when using wall functions.

The mesh dependence was smaller for the $k - \omega$ model. If this was caused by the resolved boundary layer or is implicit in the method I do not know, but in the light of the previuos paragraph the better wall treatment should be an important factor.

The computational times per iteration do not increase for the more complex models, which is a positive surprise. The non-linear $k - \omega$ model includes complex expres-

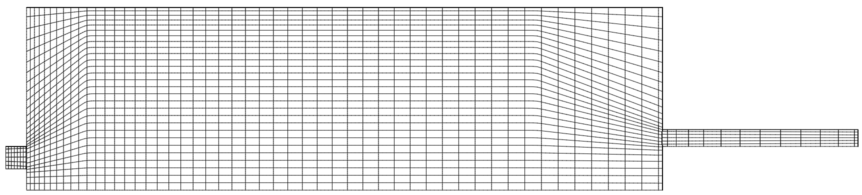

Figure 2: The mesh used for the $k-\epsilon$ models, every fourth grid point is plotted

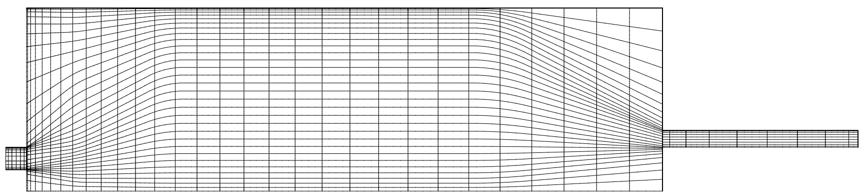

Figure 3: The mesh used for the $k-\omega$ models, every fourth grid point is plotted

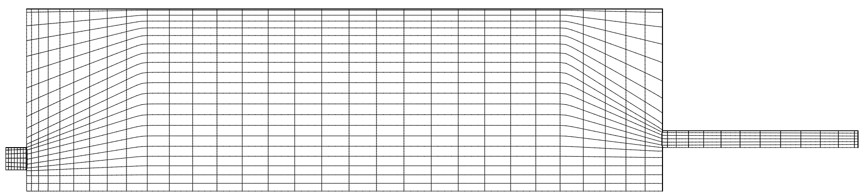

Figure 4: The smaller mesh used for testing mesh indendence for the $k-\epsilon$ models, every fourth grid point is plotted

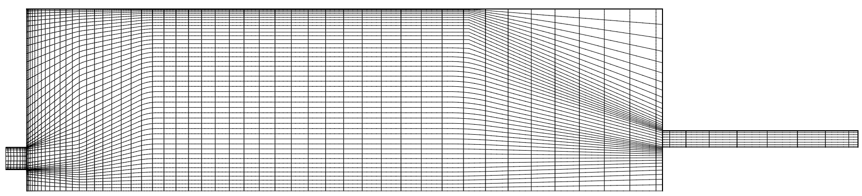

Figure 5: The larger mesh used for testing mesh indendence for the $k-\omega$ models, every fourth grid point is plotted

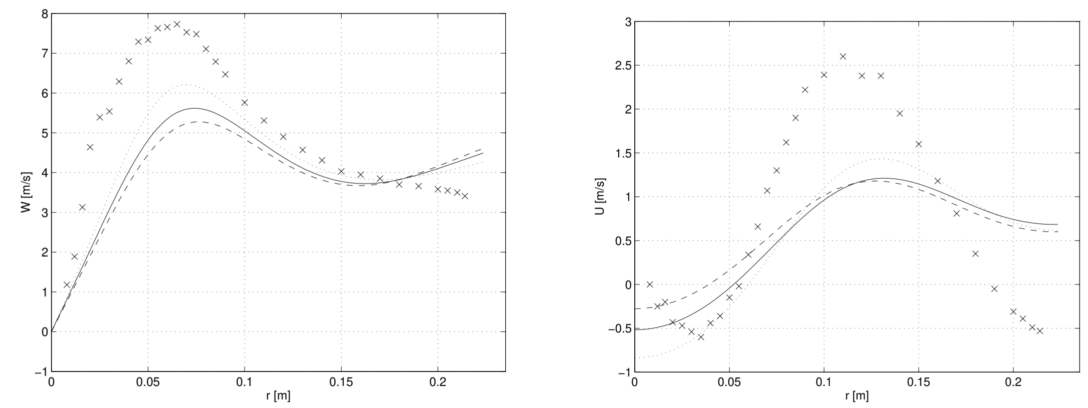

(a) *Azimuthal velocity 100 mm downstream*

(b) *Axial velocity 220 mm downstream*

Figure 6: The figures show flow case with swirl number 0.40 and are calculated with the standard $k-\epsilon$ model. These two profiles show the maximum deviations between different meshes. Note that the wall resolution is higher in the case of the dotted line compared with the other two. — standard mesh (c.f. fig.2), $\cdots$ half distance between grid points compared with the previous mesh, $--$ coarse mesh (c.f. fig.4), + Holzöpfel[13].

sions that could have been time consuming to compute. It is the same for the swirl modification which includes a coordinate transformation before evaluating C_μ. But this is not the case, computational times only depended on the mesh used.

Concerning the total time to convergence, there are some differences between the models. The $k-\omega$ models required more iterations than the standard $k-\epsilon$ model so even if each iteration was cheaper, due to smaller mesh, the time to convergence was be approximately the same. The RNG-methods required approximately 30% more time steps than the standard $k-\epsilon$ model and the swirl modification increased this number even further.

5.2 Flow Case Swirl number $S = 0.40$

5.2.1 General Behaviour

Although the models behave very differently there are some common features. The largest deviation between the models and the experiment concerns the central vortex, triggered by the annular outlet, that none of the models could predict. The outlet

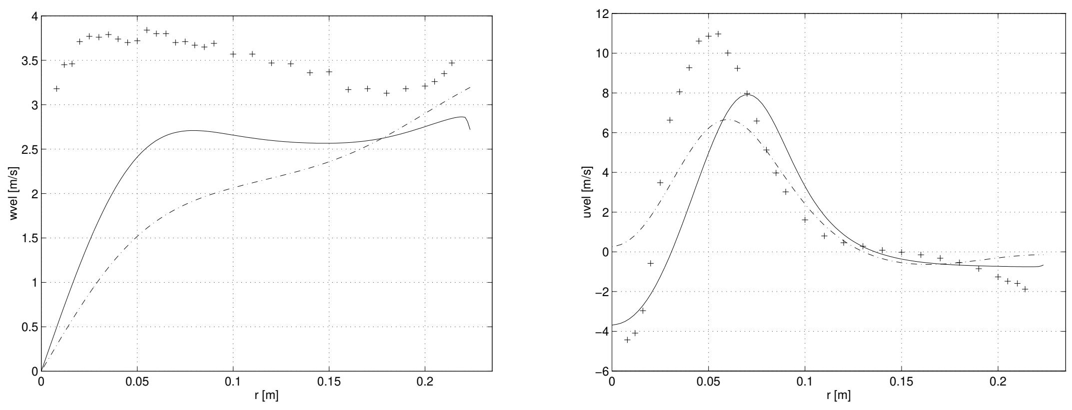

(a) *Azimuthal velocity 220 mm downstream*

(b) *Axial velocity 100 mm downstream*

Figure 7: Comparison of the $k-\epsilon$ model with and without wall functions, the figures show flow case with swirl number 0.40.$- \cdot - k-\epsilon$ without wallfcns, — $k-\epsilon$ with wallfcns, + Holzöpfel[13].

pipe causes an acceleration of the fluid a distance downstream and this results in a vortex with a peak in the azimuthal velocity where the outlet is located. The wall of the combustor also seems to be more important than expected. As the main features of the flow are located in the center of the combustor, the velocity near the wall is low and was thought to have negligible effect on the flow. However, as the momentum depends on the radius, the outer wall has a large impact on the momentum even if the velocity is small. It is mainly the azimuthal velocity that is directly affected by the wall which can be seen in figure 7(a) as a more correct shape in the outer region, close to the combustor wall, when using a correct wall treatment. The strong coupling through the swirl causes also positive effects close to the center axis. In figure 7(b) the improvement can be clearly seen in the center where the computed axial velocity follows the measured values much better when wall functions had been implemented.

All models also failed to predict the recirculation zones correctly, see figure 8. The $k-\epsilon$ model without wall functions and RNG-$k-\epsilon$ without swirl modification managed to predict that there are in fact two recirculation zones at the symmetry line. On the other hand, they underpredicted the maximal negative axial velocity in the second recirculation zone. The other models manageed this better but did not predict two zones.

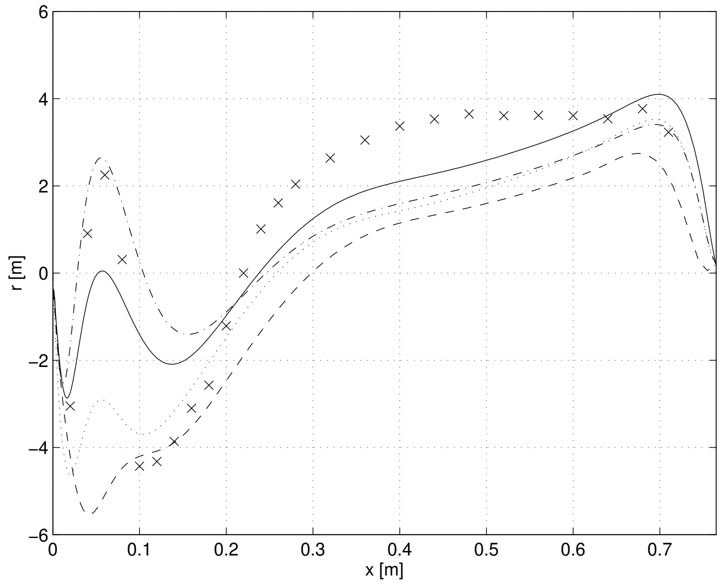

Figure 8: Axial velocity along the central axis, the figures show flow case with swirl number 0.40. $- \cdot -k-\epsilon$ without wallfcns, $\cdots k-\epsilon$ with wallfcns, — $RNG-k-\epsilon$ without swirl mod., $--\ k-\omega$, + Holzöpfel[13].

5.2.2 Features of the Different Models

Starting with the $k-\epsilon$ model without wallfunctions, it behaves qualitatively quite well. The peaks are located approximately at the right positions but the values are incorrect. In general, velocities are underpredicted but closer to the outlet the model does not manage to catch the flow properties at all. The turbulent kinetic energy is overpredicted close to the inlet but gets underpredicted further downstream. This kind of behaviour is not seen among the other models.

Implementing wall functions gave a significant improvement, as mentioned in the previous section. Particularly the size of the peaks, but to some extent also the shape of the profiles, are closer to the measured flow. However, the use of wall functions also changes the location of the peaks to the worse, see e.g. figure 7(b). For the $k-\epsilon$ model the improvement on the size of the peaks is larger than the deteriation of the location of them, but there is no guarantee that this will be the case for other models.

The Richardson number correction consists only of a minor adjustment to the standard $k-\epsilon$ model which did not alter the computed flow very much. The modification yields a slightly better solution with the higher value of the constant C_g but the improvement is not significant. The Richardson number correction was not tested together with wallfunctions.

Considering the RNG models, a large improvement can be seen over the $k - \epsilon$ models. Apart from at the end of the combustor, the computations agree very well with the measured values. Even many features of the fluctuating velocity correlations are captured. The effects of the swirl modification are small. There are some improvements but computational disadvantages such as slower convergence rate have to be considered when choosing model. It is mainly in the detailed structure of the velocity correlations that the differences are noticable. The swirl modification brings out some of the smaller peaks and is also able to predict the location of the larger peaks more correctly than RNG-$k - \epsilon$ without swirl modification. Examples can be seen in figures 9(a) and 9(b).

However, in some cases the swirl modification yields a result that is worse compared with the standard RNG-$k - \epsilon$. One example is shown in figure 9(c). The peak is more correct when not using the swirl modification but the form of the curve is better captured with the modification.

Also in this case, the model was tested with wall functions. The improvement for standard $k - \epsilon$ is large but this is not the case here. In some aspects, the solution with wall functions is slightly better but in other, the case is the inverse. The construcion of μ_{eff} is made to include low-Re effects so perhaps the mesh used was fine enough to give good wall treatment for RNG-$k - \epsilon$ without wall functions. Wall functions and the swirl modification is not compatible at all. The solution is in this case worse in all aspects than the standard RNG-$k - \epsilon$.

The $k - \omega$ models are also considerably better than the standard $k - \epsilon$ model, with or without wall functions. The improvement is probably to some extent caused by the more correct wall treatment. Compared with the RNG methods, they are slightly better close to the outlet and approximately as good as the RNG methods in the first half of the combustor. The difference between the non-linear $k - \omega$ model and the standard version reminds of the case for the RNG-$k - \epsilon$ with and without swirl modification, the non-linear model gives more details and is closer in shape. In this case though, the standard $k - \omega$ model is considerably better in predicting the sizes of the peaks. There is one feature though where the non-linear model shows a considerably better performance and this is the central vortex. Among all models only the non-linear $k - \omega$ model shows a tendency towards developing the vortex that is present in the measurements.

5.3 Summarizing Case $S = 0.40$

The group of models that shows the best performance is the $k - \omega$ models. They are closest both in the location and the size of the peaks, and thereby also in the shape of

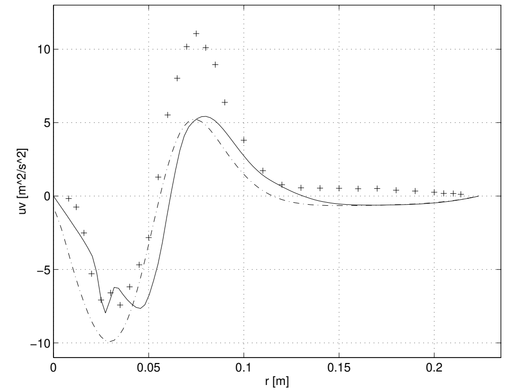

(a) $\overline{u'v'}$ *100 mm downstream*

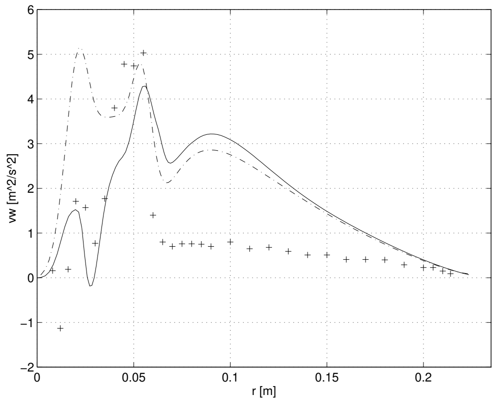

(b) $\overline{v'w'}$ *20 mm downstream*

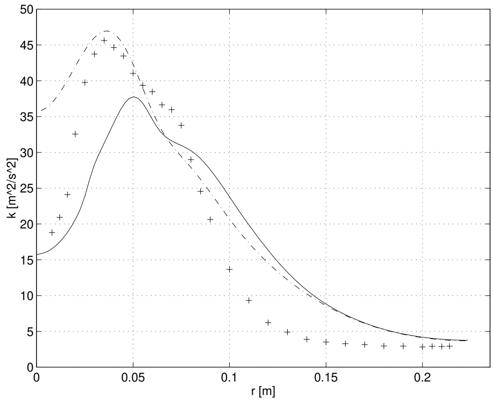

(c) k *100 mm downstream*

Figure 9: Comparison between RNG-$k-\epsilon$ with and without swirlmodification, the figures show flow case with swirl number 0.40. $-\cdot-RNG-k-\epsilon$ without swirl mod., — $RNG-k-\epsilon$ with swirl mod., + Holzöpfel[13]

the profiles. Also the RNG models yield satisfactory solutions but they are not quite as good as the $k - \omega$ models. The implementation of wall functions improved the standard $k - \epsilon$ model considerably but did not affect RNG-$k - \epsilon$ significantly.

5.4 Flow Case Swirl number $S = 0.95$

5.4.1 General Behaviour

This flow case has shown to be considerably more difficult to predict. The problems observed for the lower swirl case is even more accentuated in this case. However, it also seems that it has been difficult to create a good set of measurements. By inspecting the measured velocities, one can see a strong central vortex and several smaller vortices that indicates that the flow is probably not perfectly axisymmetric or stationary, see figure 36 in appendix.

Therefore, I concentrate this evaluation on the first part of the combustor where the measured flow are acceptable and at least some correlation between computed and measured profiles can be found.

5.4.2 Features of the Different Models

In this case, all models behave more or less in an unacceptable way. From the plotted profiles in appendix, it seems that the models overpredict the effect of the swirl. With this I mean that the expansion of the jet is greater, the peaks are located at a larger radius, see e.g. figure 42 in appendix. The tendency was the same for the previous flow case but more prominent here. The improvements using wall functions or the RNG-$k - \epsilon$ model that were described in the previuos section are not at all as large in this flow case. They are slightly better in predicting the size of the peaks, but the locations are wrong.

The non-linear $k - \omega$ model, however, seems to have the same performance for this higher swirl number as it had for the lower. It manages to predict the location of the peaks, at least in the first part of the combustor, but underpredicts the size of them. There are also large deviations close to the central axis of the combustor. Both these defiancies are probably due to the inability of predicting the central vortex.

Looking at the velocity correlations, the situation is about the same with the non-linear $k - \omega$ model closest to the measurements, but not close enough to give satisfactory results. It is interesting to note that this model manages to predict all six components of the correlation tensor correctly. The other models may be successfull in predicting some of the components but are wrong for others, see e.g. figures 52 – 53.

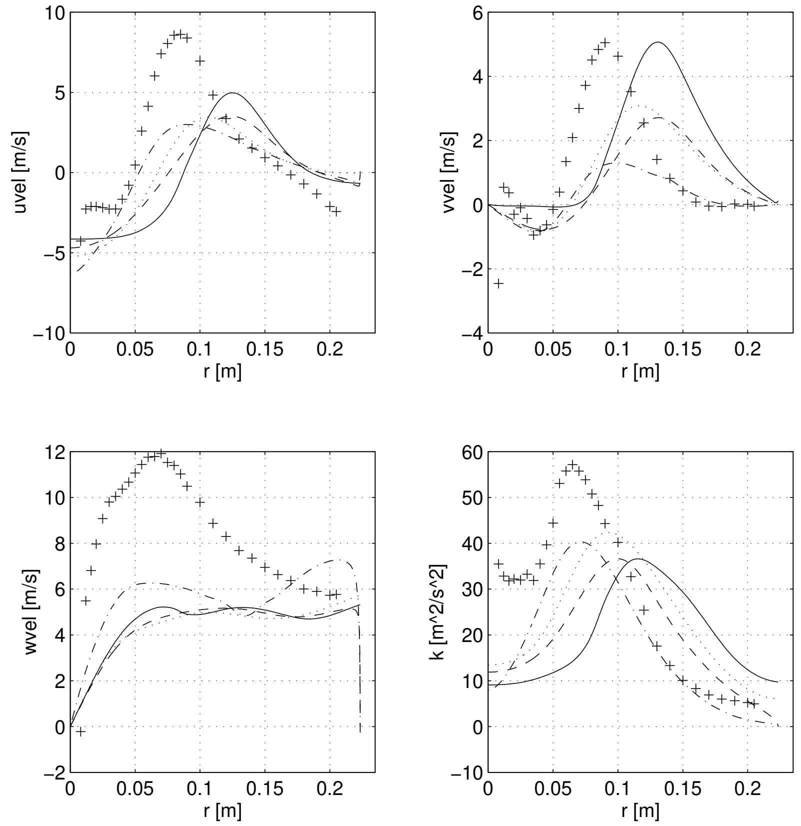

Figure 10: The figure shows an example of how the models behave in the higher swirl flow. Non-linear $k-\omega$ has the right location but underpredicts the velocities, RNG-$k-\epsilon$ with swirl modification is closer in the size of the peaks but are wrong in the location adnd the other models lie in between. 100 mm downstream, $\cdots RNG-k-\epsilon$, $-\cdot-$non-linear $k-\omega$, $---k-\omega$, — $RNG-k-\epsilon$ with swirl mod., + Holzöpfel[13]

5.5 Summarizing Case $S = 0.95$

It is not possible to select a winner in this case, only losers. Only the non-linear $k - \omega$ model is reasonably close to the measured set of data when considering the location of the peaks while the RNG-$k - \epsilon$ has better top values. Close to the central axis no model is good but the problems of predicting the type of vortex that often arises in swirling flow are well known[6].

6 Conclusions

In general, this work has shown that the standard $k - \epsilon$ model should not be used for swirling flows, especially without wall functions. The non-linear $k - \omega$ model shows good over-all performance. It gives acceptable results in both flow cases even if the standard $k - \omega$ model is slightly better for swirl number 0.40. The drawback with this model is that it is difficult to implement. The non-linear terms yield complex expressions that are difficult to get correct. However, it did not take longer time using the non-linear model compared to the standard $k - \omega$ model.

Among the $k - \epsilon$ models, the RNG methods are clearly the best to use. The standard RNG-$k - \epsilon$ model is easy to implement in an existing code, while the swirl modification demands a little more work. The improvements due to the swirl modification are small and it most be decided for each case if it is worth the extra work with the modification to get the higher accuracy.

The flow case with the higher flow was the more difficult predict. That the inlet conditions is important for swirling flow cases has been reported earlier[2]. The type of outlet seems to have a large impact also. This may be the case only when an annular outlet is used. It is difficult to say if it is the geometry or the definition of the the outlet flow conditions that causes the difficulties.

References

[1] A.H. Lefebvre. *Gas Turbine Combustion.* Taylor and Francis, USA, 1983.

[2] D.G. Sloan, P.J. Smith, and L.D. Smoot. Modeling of swirl in turbulent flow systems. *Prog. Energy Combust. Sci*, 12:163–250, 1986.

[3] D.C. Wilcox. *Turbulence modeling for CFD.* DCW Industries Inc., La Canada , California, 1993.

[4] H. Tennekes and J.L. Lumley. *A First Course in Turbulence.* The MIT Press, Massachusetts , USA, 1972.

[5] R.L. Panton. *Incompressible Flow.* John Wiley and Sons, New York , USA, 1984.

[6] A. Smirnoff. Turbulent swirl flow modeling in axisymmetric confined geometries. Thesis for the degree of Licentiate of Engineering, report 95/5, Dept. of Thermo and Fluid Dynamics, Chalmers Univ. Techn., Göteborg, 1995.

[7] M.A. Leschziner and W. Rodi. Calculation af annular and twin parallel jets using various discretization schemes and turbulence-model variations. *J. Fluid Engng*, 103:352–360, 1981.

[8] M. Yin, F. Shi, and Z. Xu. Renormalization group based ke turbulence model for flow in a duct with strong curvature. *Int. J. Engng Sci*, 34:243–248, 1996.

[9] J. Larsson. Two-equation turbulence models for turbine blade heat transfer simulations. AIAA papers, 1997.

[10] T.-H. Shih. Chapter 4, one point turbulence closure. Proc. ECOFTAC/IUTAM Summer School on Turbulence and Transition Modelling, Stockholm, 1995.

[11] L.-E. Eriksson. Development and validation of highly modular flow solver versions in g2dflow and g3dflow series for compressible viscous reactiong flow. Report 9970-1162, Volvo Aero Corporation, 1995.

[12] J. Larsson. Numerical simulation of turbine blade heat transfer. Thesis for the degree of Licentiate of Engineering, report 96/4, Dept. of Thermo and Fluid Dynamics, Chalmers Univ. Techn., Göteborg, 1996.

[13] F. Holzöpfel. Zur turbulenzstruktur freier und eingeschlossener drehstrümungen. Dissertation, Engler-Bunte-Institut der Universität Karlsruhe, 1996.

[14] F. Holzöpfel, B. Lenze, and W. Leuckel. Assessment of a quintuple hotwire measurement technique for highly turbulent flows. *Exp. Fluids*, 18:100–106, 1994.

[15] F. Holzöpfel, B. Lenze, and W. Leuckel. Quintuple hotwire measurements in highly turbulent confined swirl flows. 2nd Int. Conf. Fluid Dyn. Meas. APpl., Beijing, pp. 338-343, 1994.

[16] Y.G. Lai. Predictive capabilities of turbulence models for a confined swirling flow. *AIAA journal*, 34:1743–1745, 1996.

[17] P. Emvin. Installation and validation of the unstructured flow simulation package FLUENT together with the parametric mesh generator AML. Report 9970-1907, Volvo Aero Corporation, 1996.

A Measured Velocity Field, $S = 0.40$

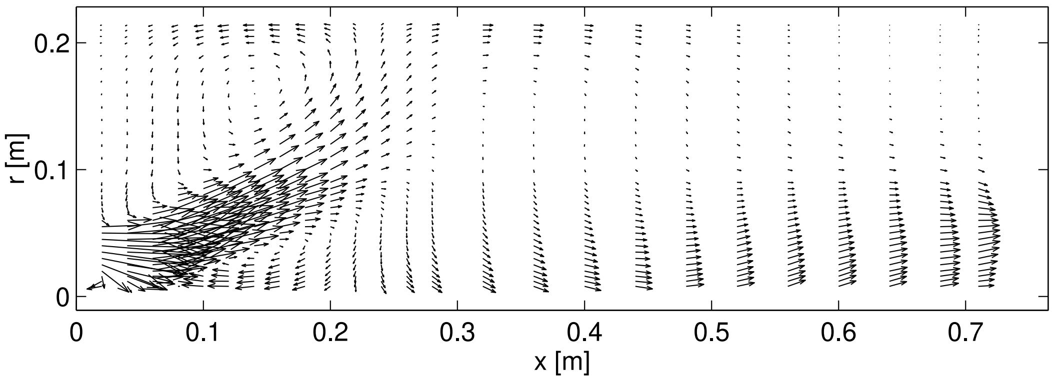

Figure 11: The measured 2D axisymmetric flow case for swirl number $S = 0.40$

B Velocity Profiles, $S = 0.40$

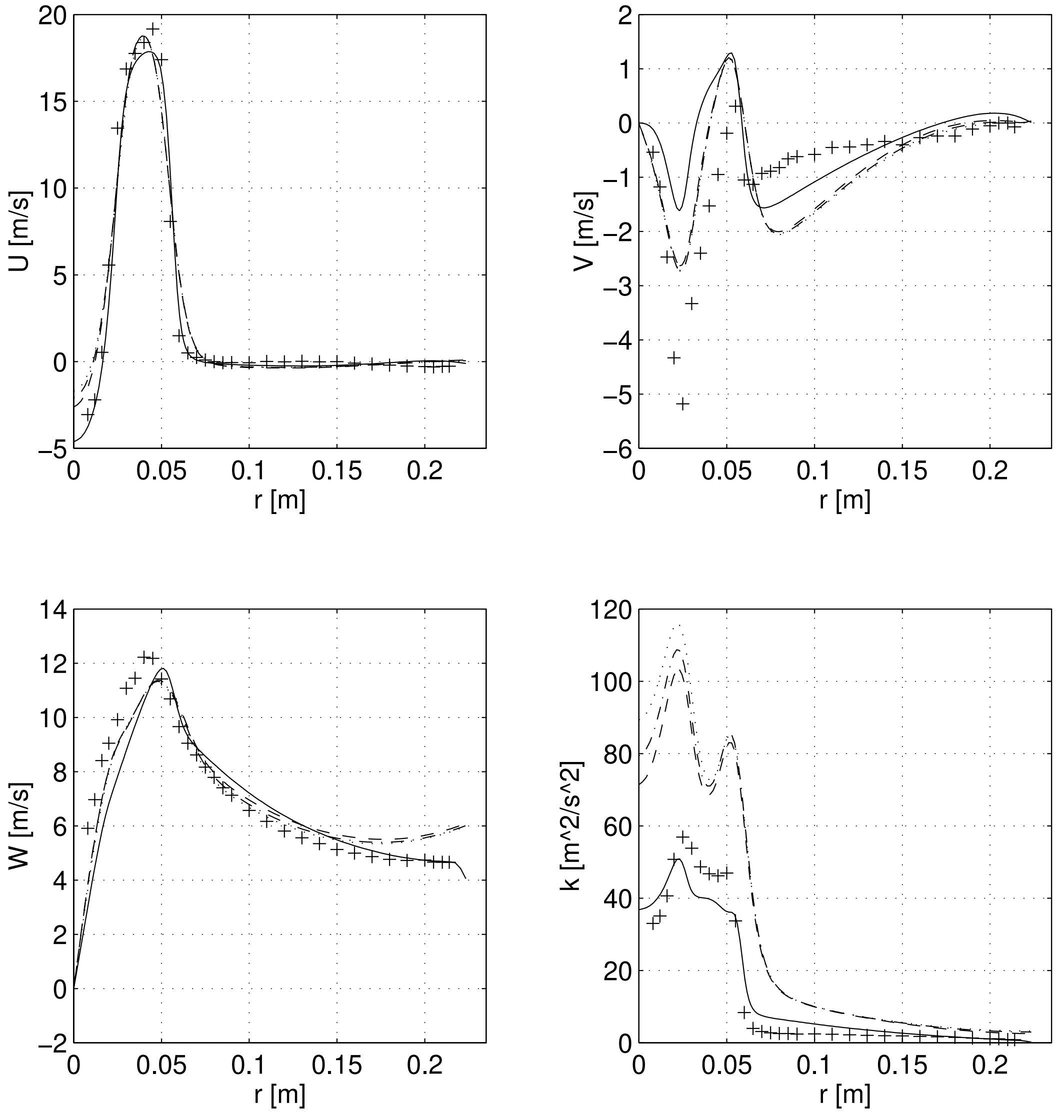

Figure 12: 20 mm downstream, $\cdots k-\epsilon$, $-\cdot-k-\epsilon \quad RN = 0.002$, $---k-\epsilon \quad RN = 0.008$, — $k-\epsilon$ with wallfcn, + Holzöpfel[13]

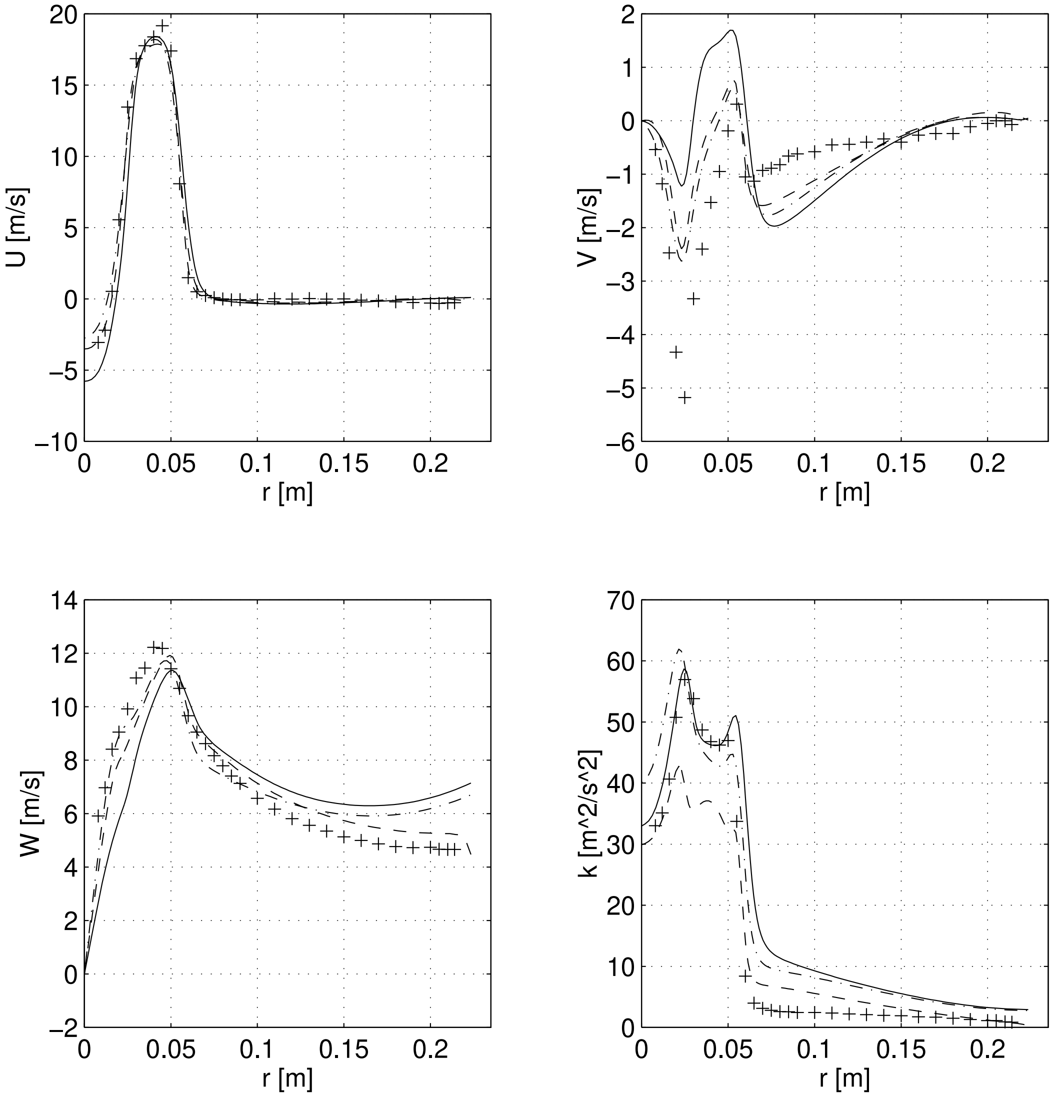

Figure 13: 20 mm downstream, $- \cdot - RNG - k - \epsilon$, $- - - RNG - k - \epsilon$ with wallfcns, — $RNG - k - \epsilon$ with swirl mod., + Holzöpfel[13]

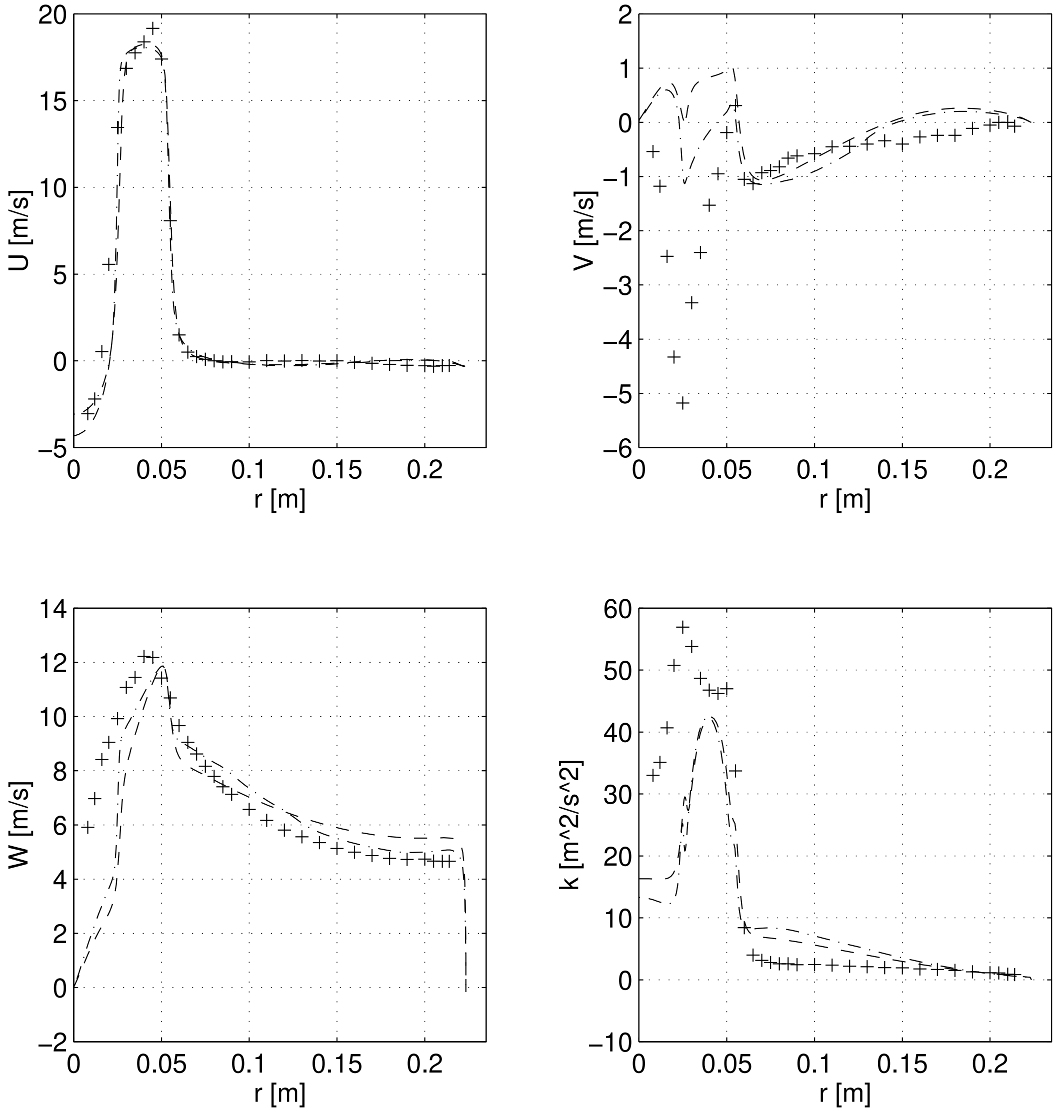

Figure 14: 20 mm downstream, $- \cdot -$non-linear $k-\omega$, $---k-\omega$, + Holzöpfel[13]

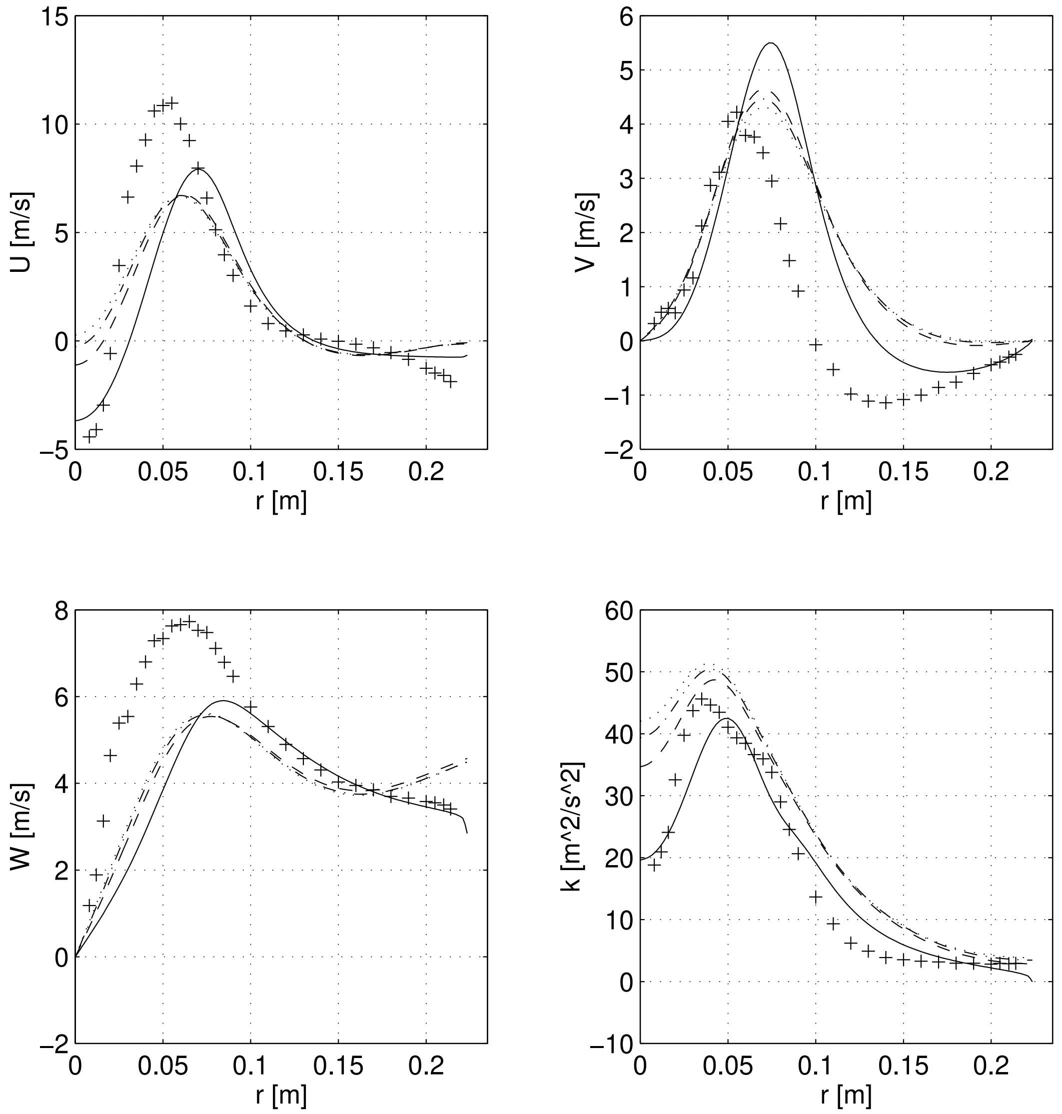

Figure 15: 100 mm downstream, $\cdots k-\epsilon$, $-\cdot- k-\epsilon \quad RN=0.002$, $--- k-\epsilon \quad RN=0.008$, — $k-\epsilon$ with wallfcn, + Holzöpfel[13]

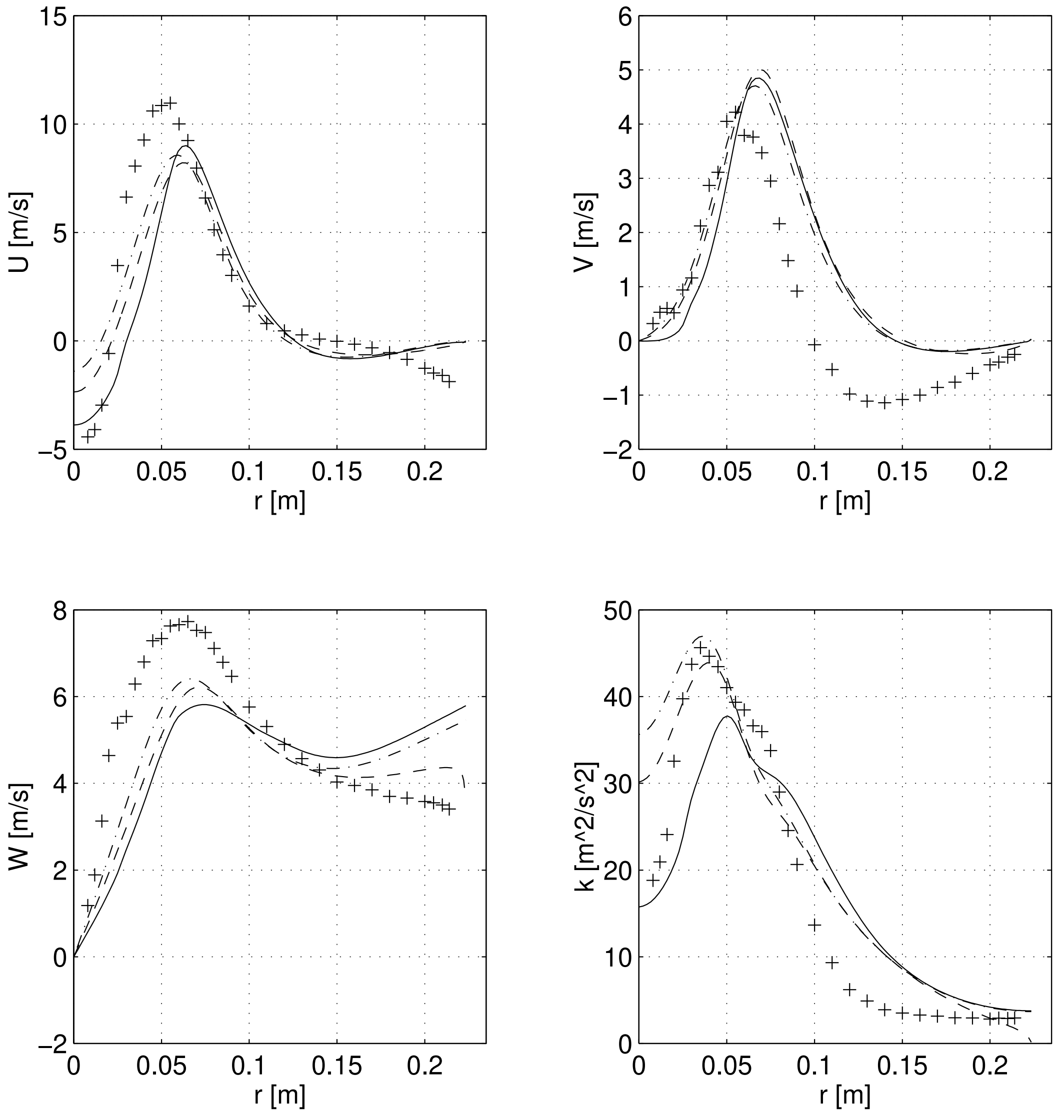

Figure 16: 100 mm downstream, $-\cdot-RNG-k-\epsilon$, $---RNG-k-\epsilon$ with wallfcns, — $RNG-k-\epsilon$ with swirl mod., + Holzöpfel[13]

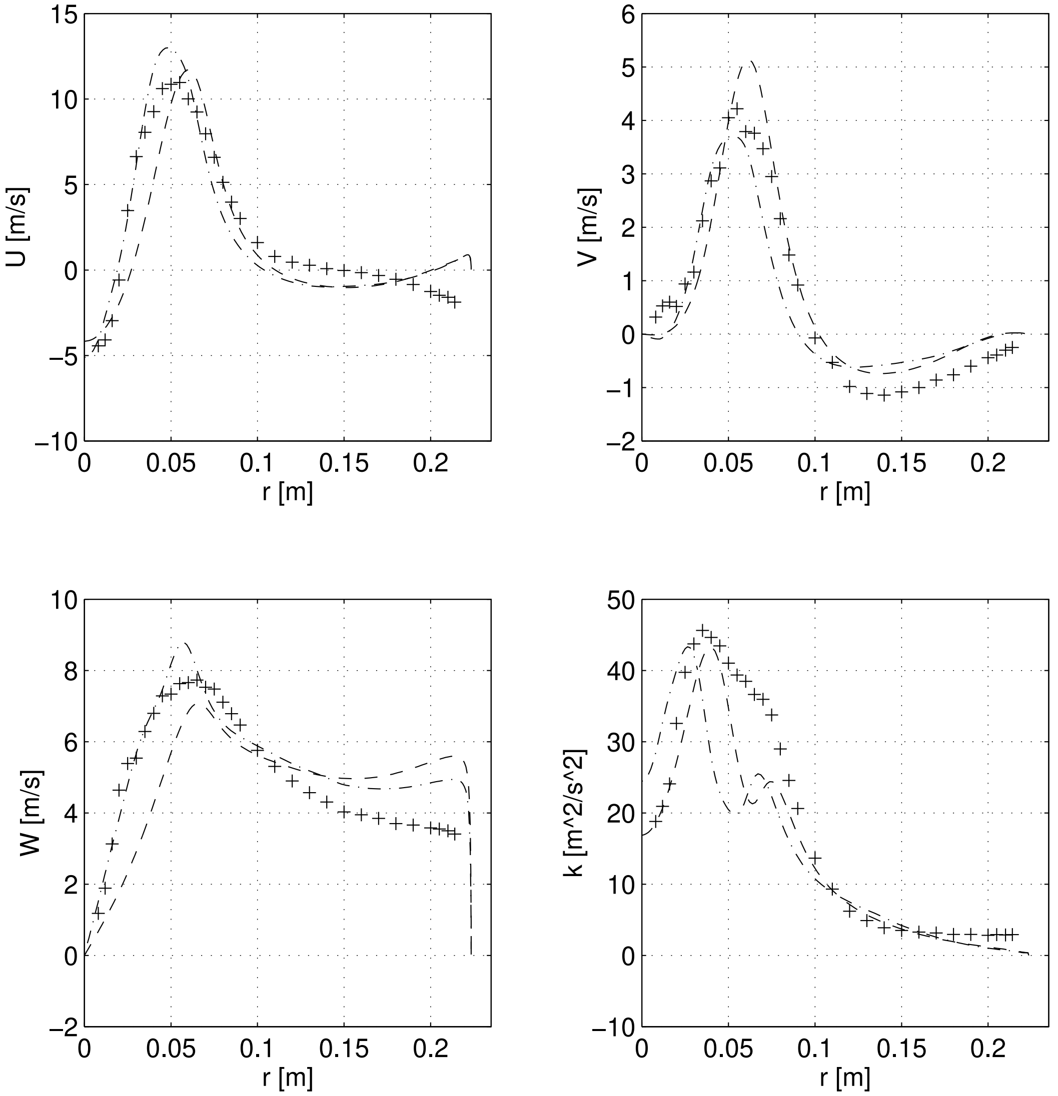

Figure 17: 100 mm downstream, $-\cdot-$non-linear $k-\omega$, $---k-\omega$, + Holzöpfel[13]

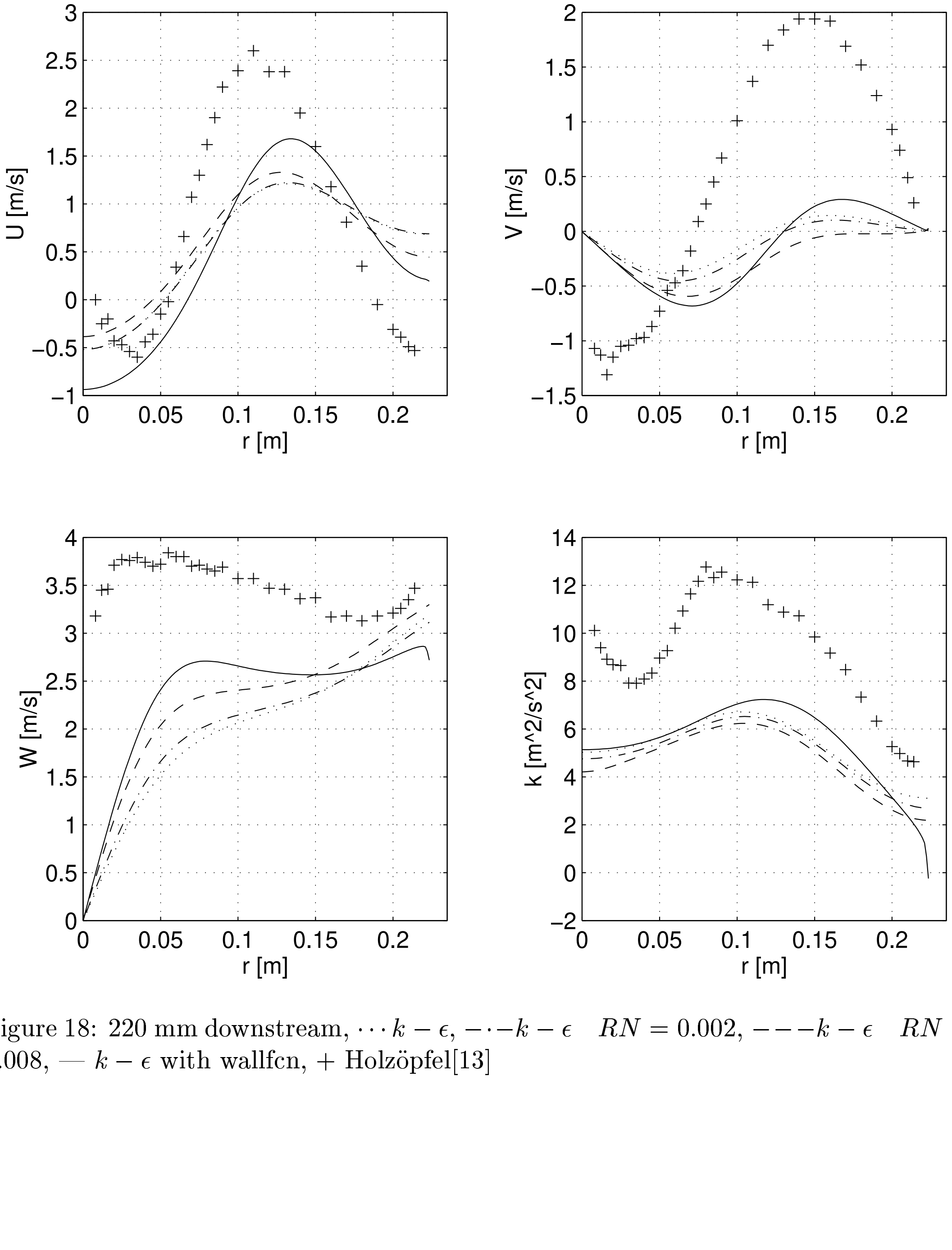

Figure 18: 220 mm downstream, $\cdots k - \epsilon$, $-\cdot- k - \epsilon \quad RN = 0.002$, $--- k - \epsilon \quad RN = 0.008$, — $k - \epsilon$ with wallfcn, + Holzöpfel[13]

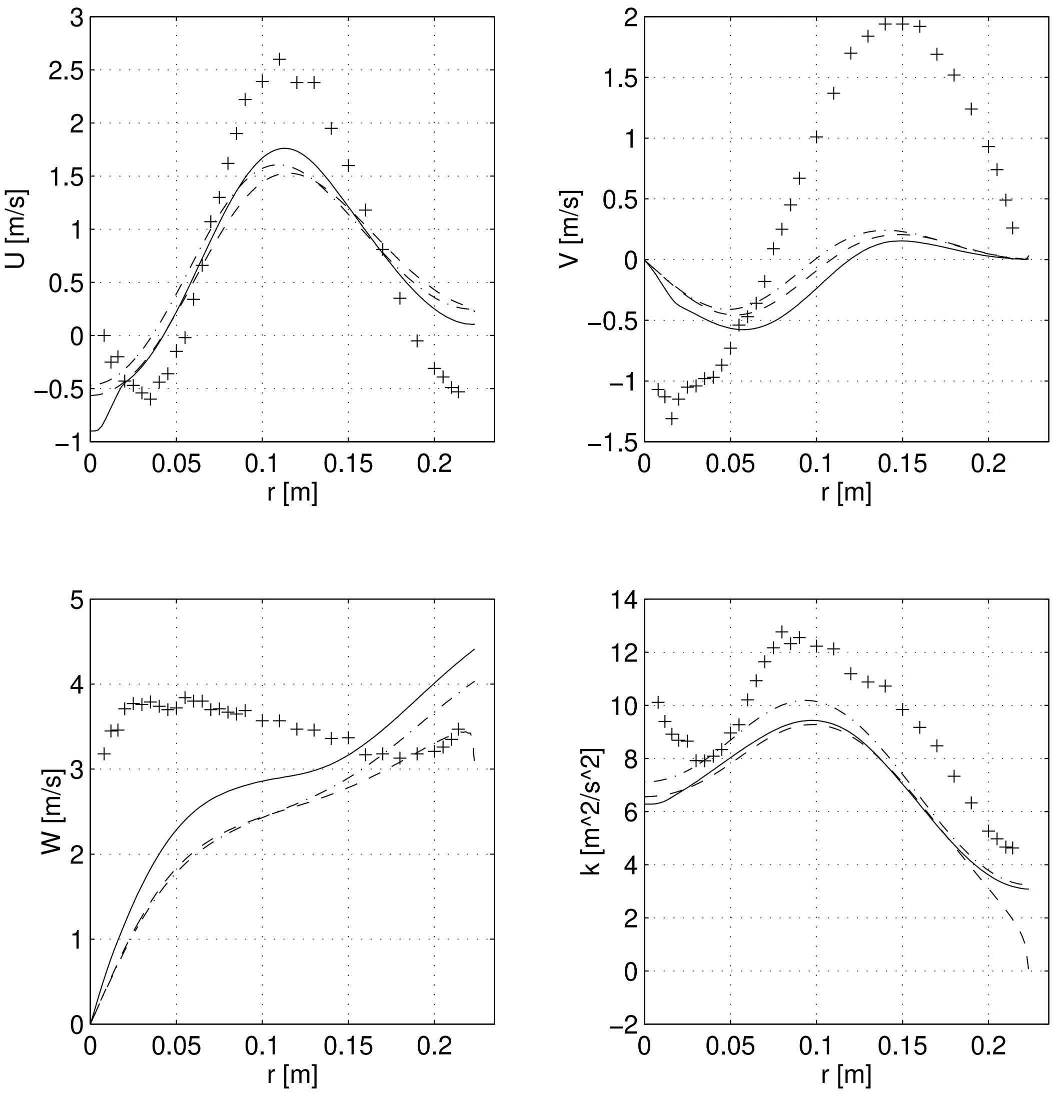

Figure 19: 220 mm downstream, $-\cdot-RNG-k-\epsilon$, $---RNG-k-\epsilon$ with wallfcns, — $RNG-k-\epsilon$ with swirl mod., + Holzöpfel[13]

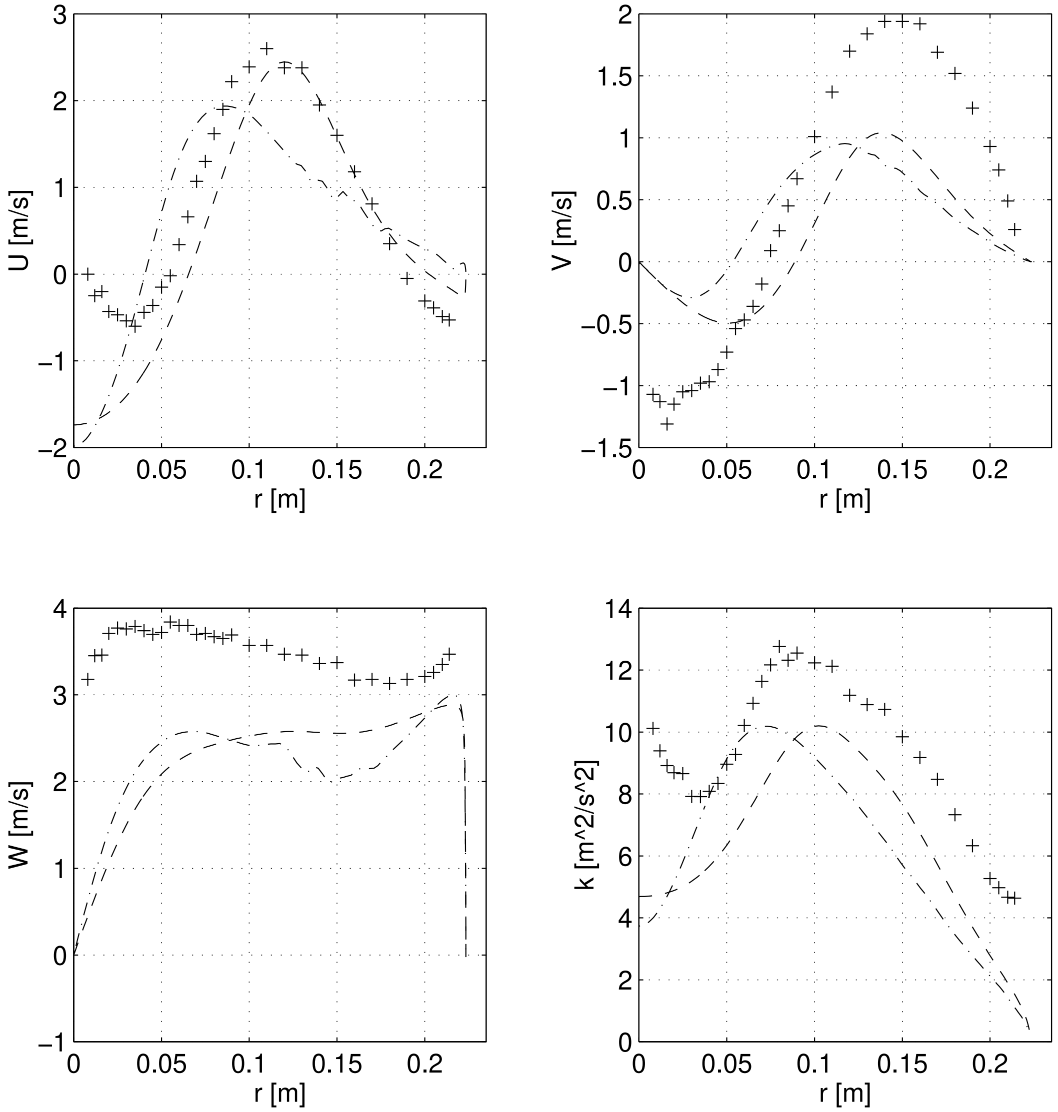

Figure 20: 220 mm downstream, $-\cdot-$non-linear $k-\omega$, $---k-\omega$, + Holzöpfel[13]

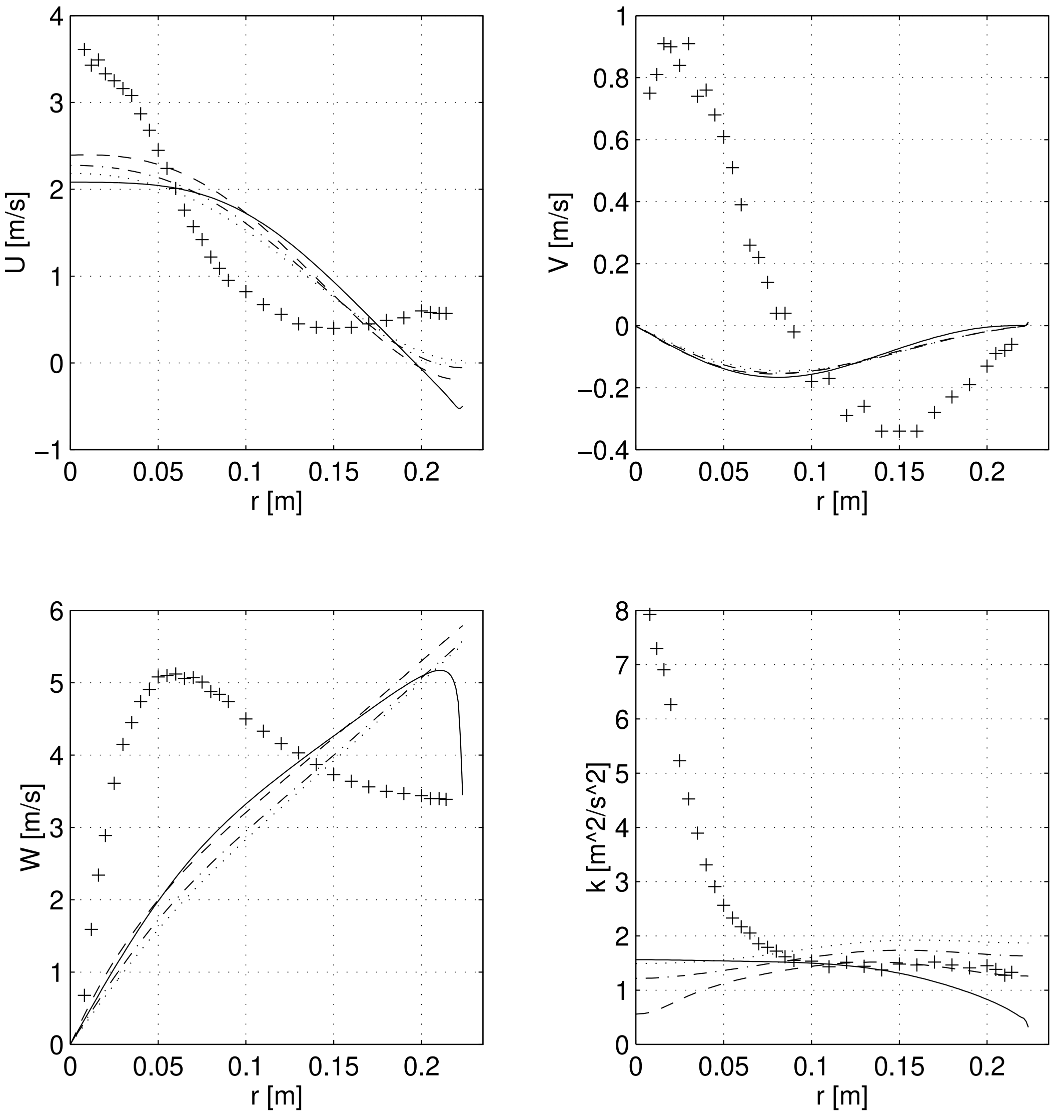

Figure 21: 520 mm downstream, $\cdots k-\epsilon$, $-\cdot - k-\epsilon \quad RN = 0.002$, $---k-\epsilon \quad RN = 0.008$, — $k-\epsilon$ with wallfcn, + Holzöpfel[13]

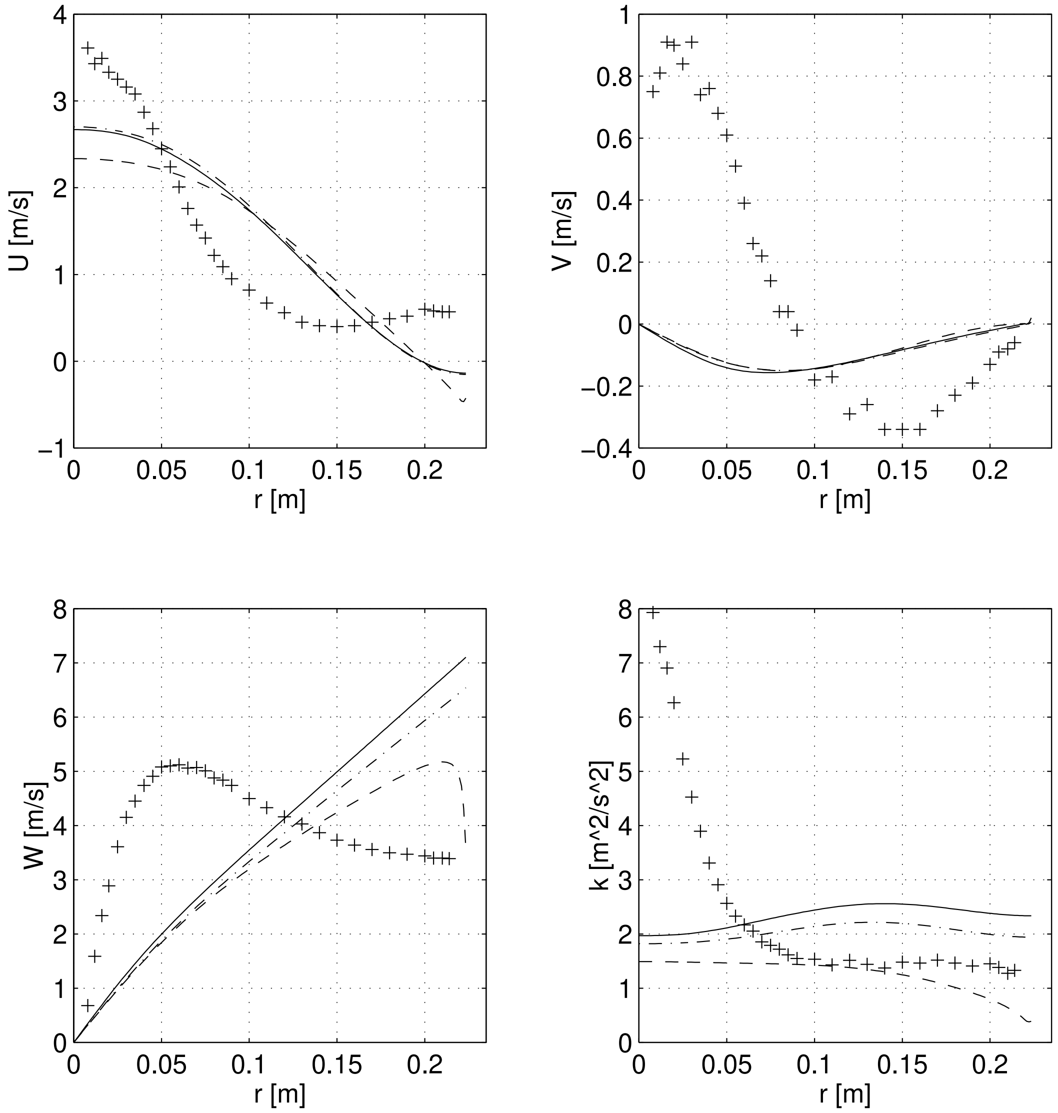

Figure 22: 520 mm downstream, $-\cdot - RNG - k - \epsilon$, $- - - RNG - k - \epsilon$ with wallfcns, — $RNG - k - \epsilon$ with swirl mod., + Holzöpfel[13]

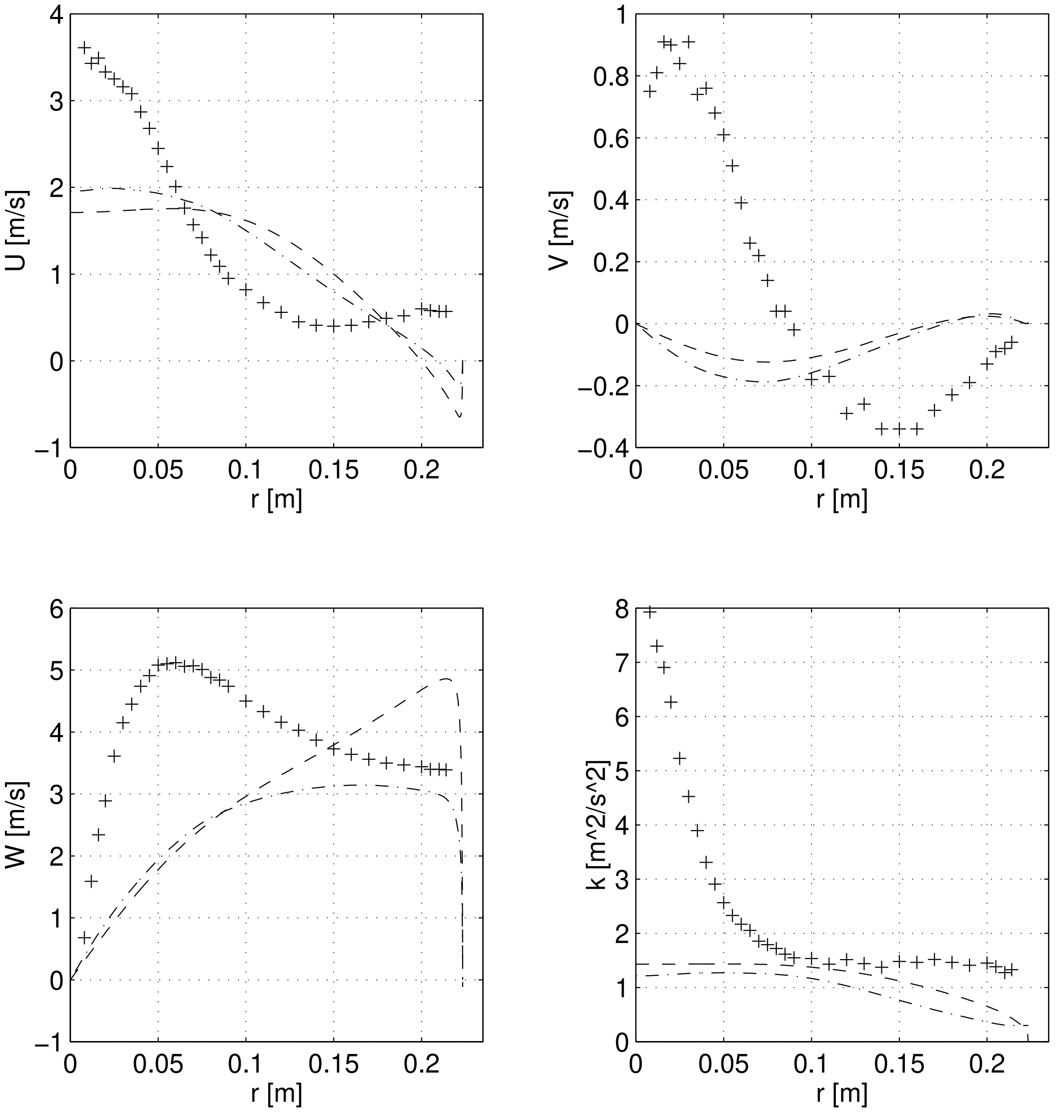

Figure 23: 520 mm downstream, $-\cdot-$non-linear $k-\omega$, $---k-\omega$, + Holzöpfel[13]

C Velocity Correlations, $S = 0.40$

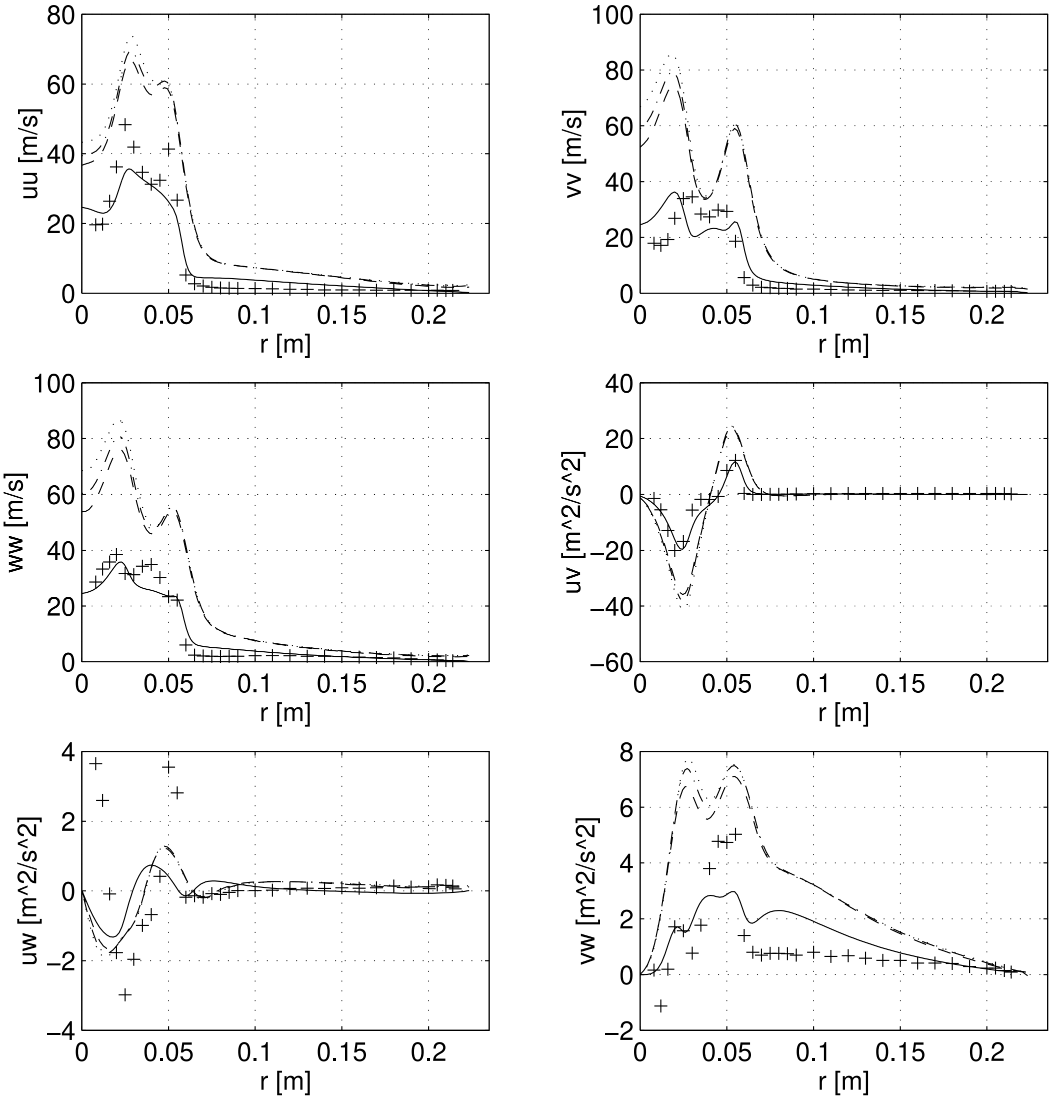

Figure 24: 20 mm downstream, $\cdots k-\epsilon$, $-\cdot- k-\epsilon \quad RN = 0.002$, $--- k-\epsilon \quad RN = 0.008$, — $k-\epsilon$ with wallfcn, + Holzöpfel[13]

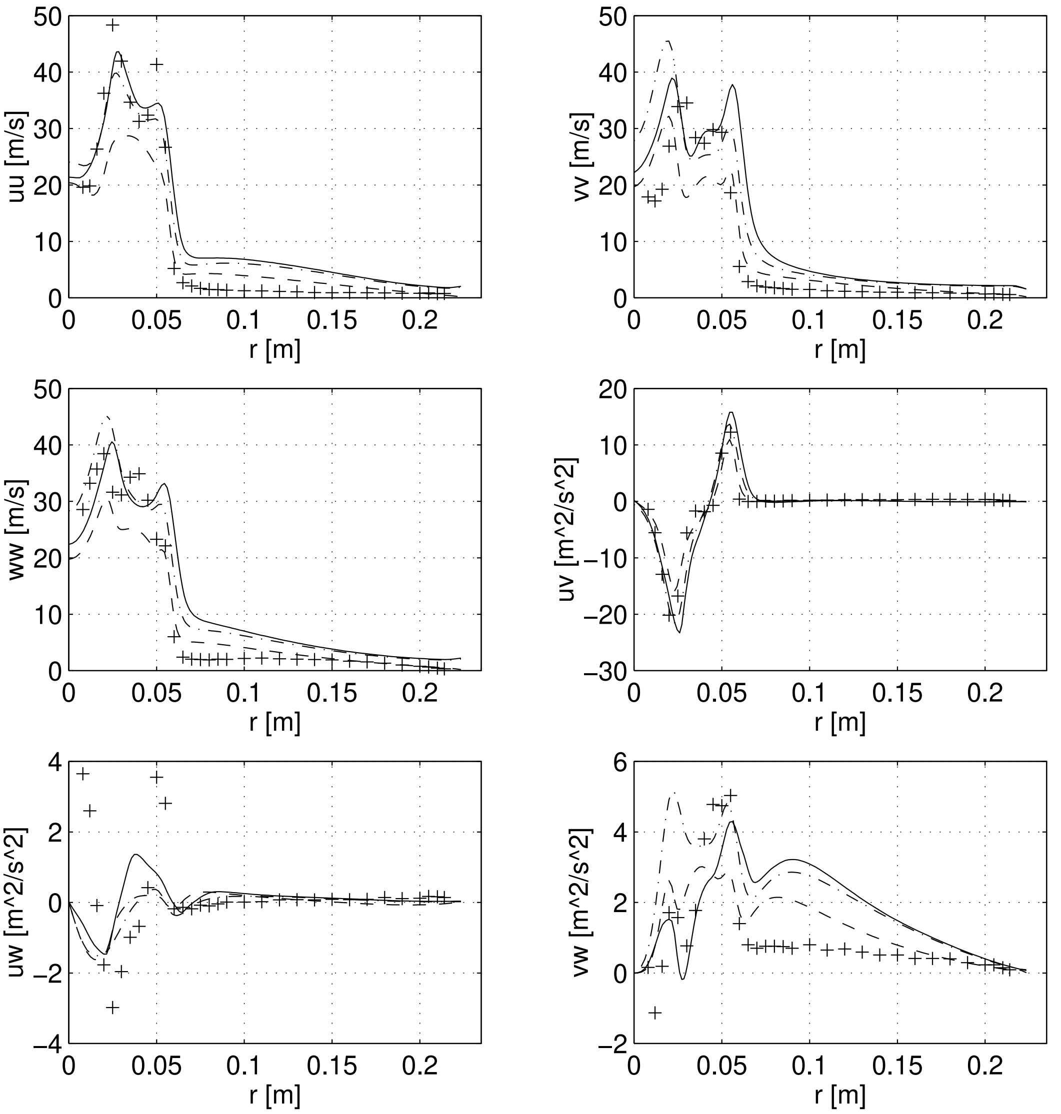

Figure 25: 20 mm downstream, $-\cdot-RNG-k-\epsilon$, $---RNG-k-\epsilon$ with wallfcns, — $RNG-k-\epsilon$ with swirl mod., + Holzöpfel[13]

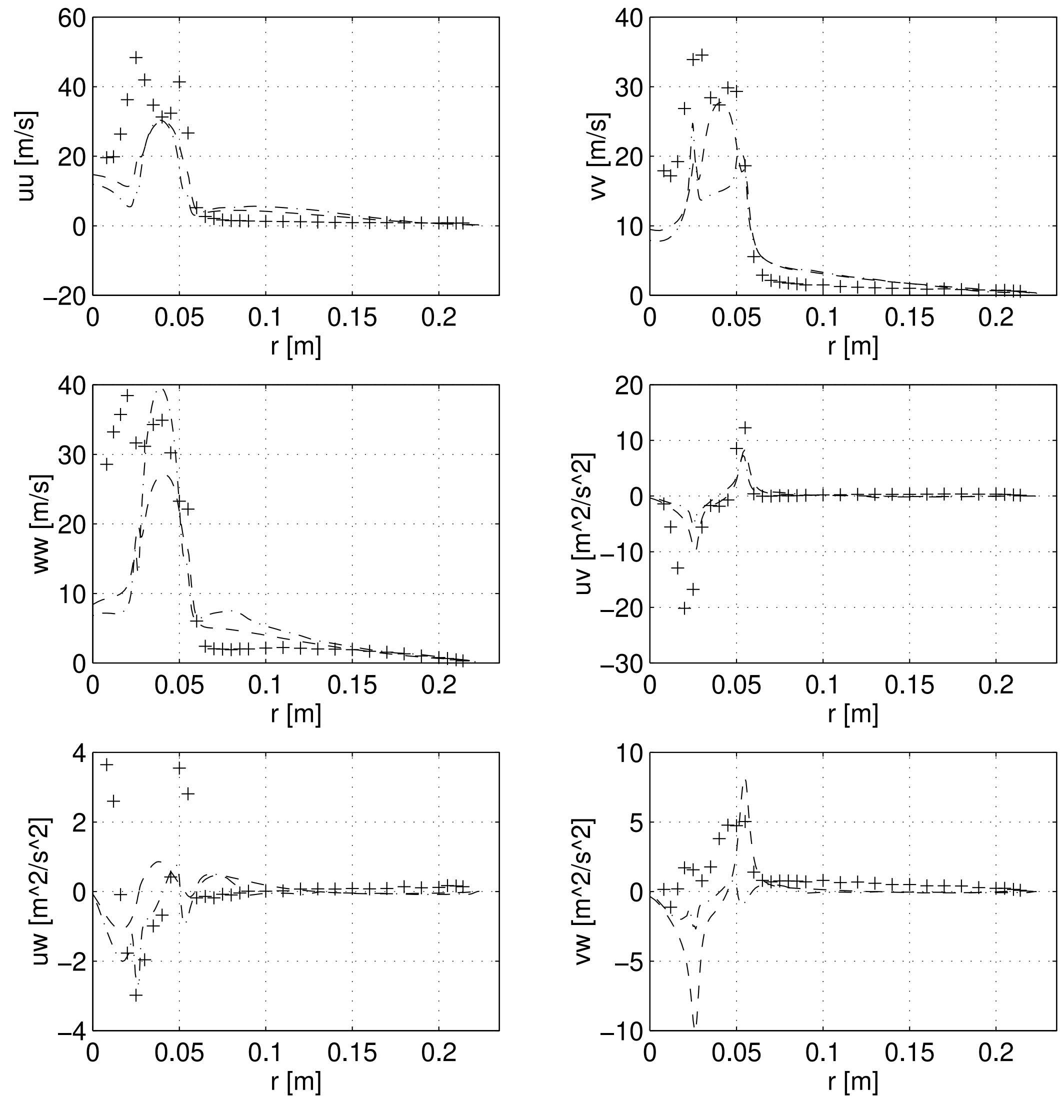

Figure 26: 20 mm downstream, $-\cdot-$non-linear $k-\omega$, $---k-\omega$, + Holzöpfel[13]

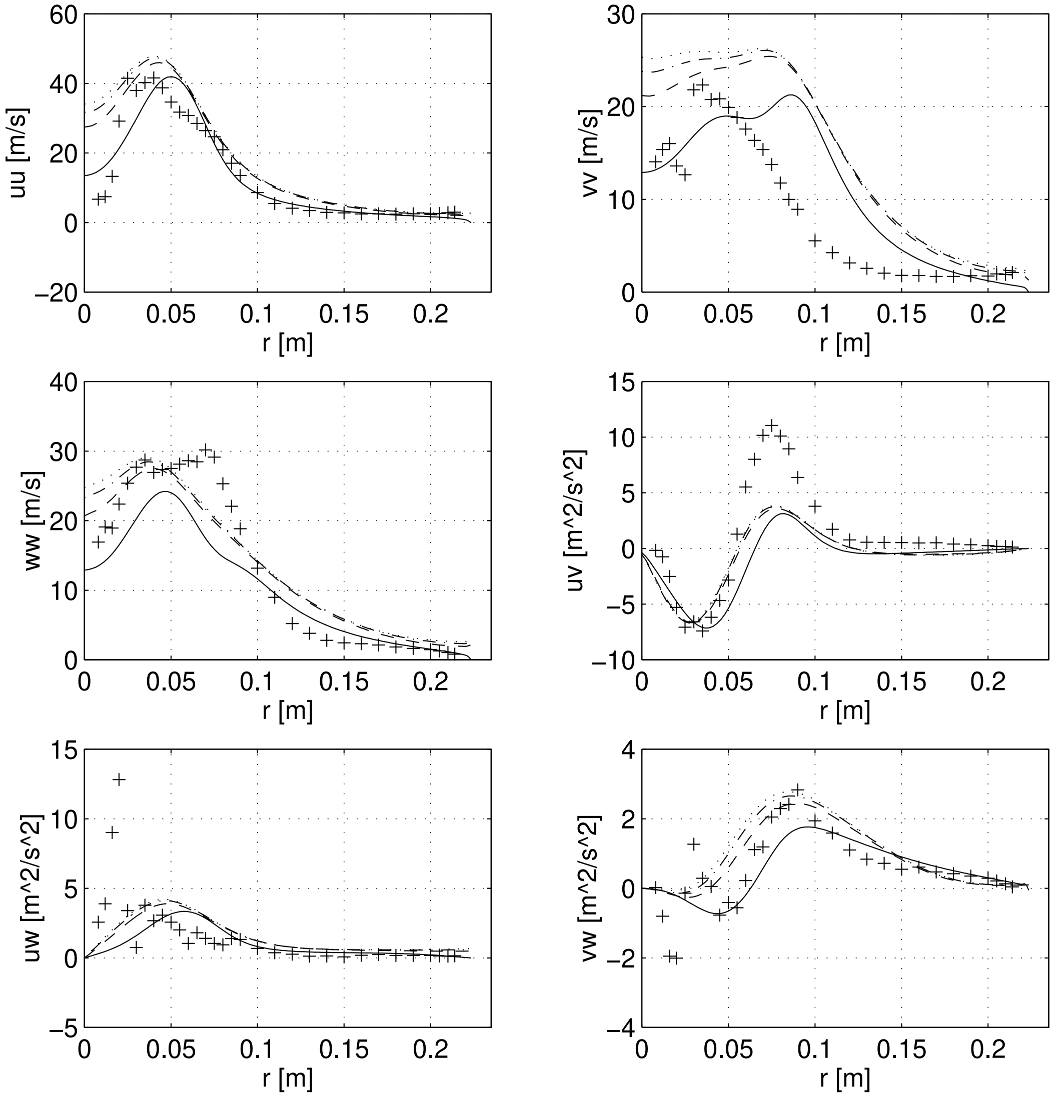

Figure 27: 100 mm downstream, $\cdots k-\epsilon$, $-\cdot- k-\epsilon \quad RN = 0.002$, $--- k-\epsilon \quad RN = 0.008$, — $k-\epsilon$ with wallfcn, + Holzöpfel[13]

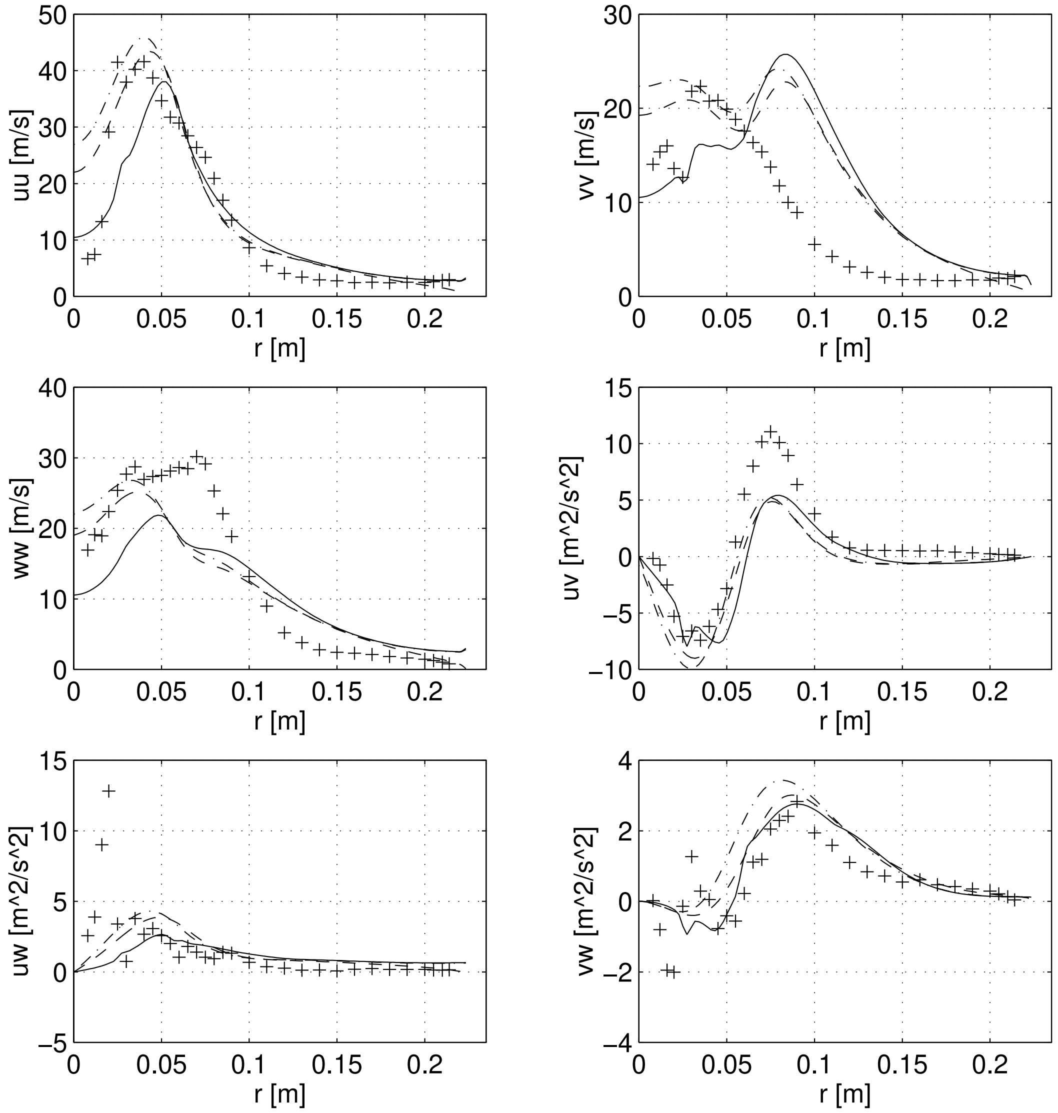

Figure 28: 100 mm downstream, $- \cdot - RNG - k - \epsilon$, $- - - RNG - k - \epsilon$ with wallfcns, — $RNG - k - \epsilon$ with swirl mod., + Holzöpfel[13]

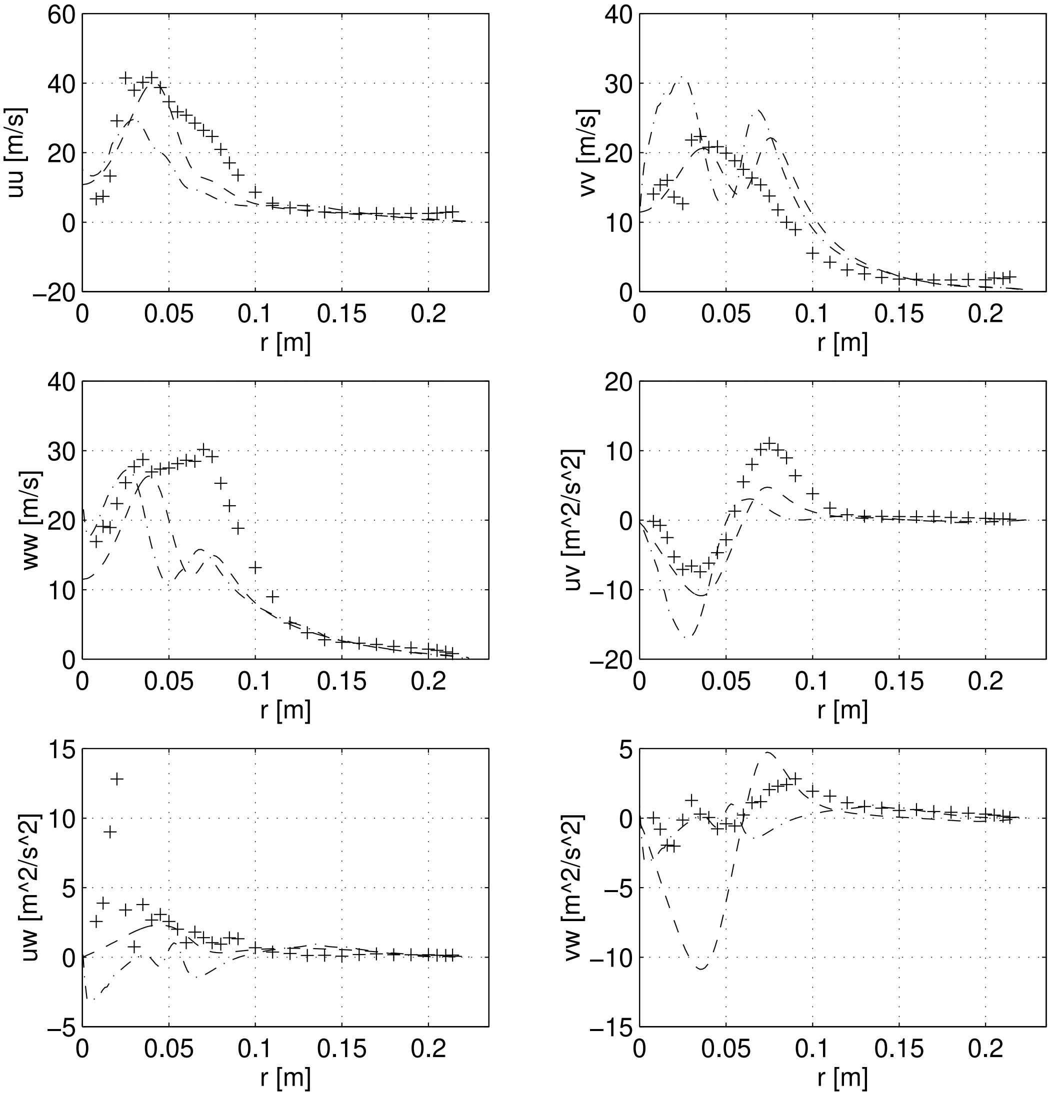

Figure 29: 100 mm downstream, $-\cdot-$non-linear $k-\omega$, $---k-\omega$, $+$ Holzöpfel[13]

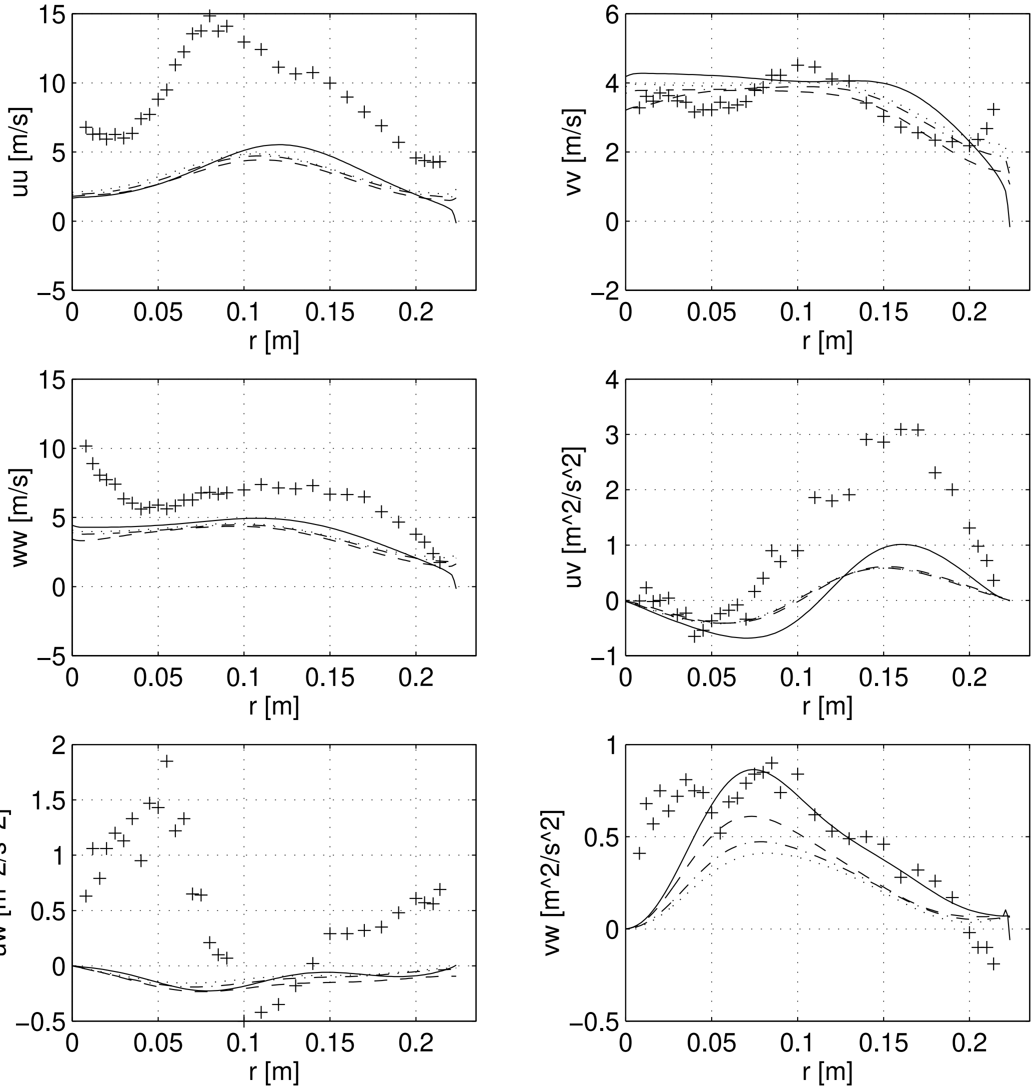

Figure 30: 220 mm downstream, $\cdots k-\epsilon$, $-\cdot- k-\epsilon \quad RN = 0.002$, $--- k-\epsilon \quad RN = 0.008$, — $k-\epsilon$ with wallfcn, + Holzöpfel[13]

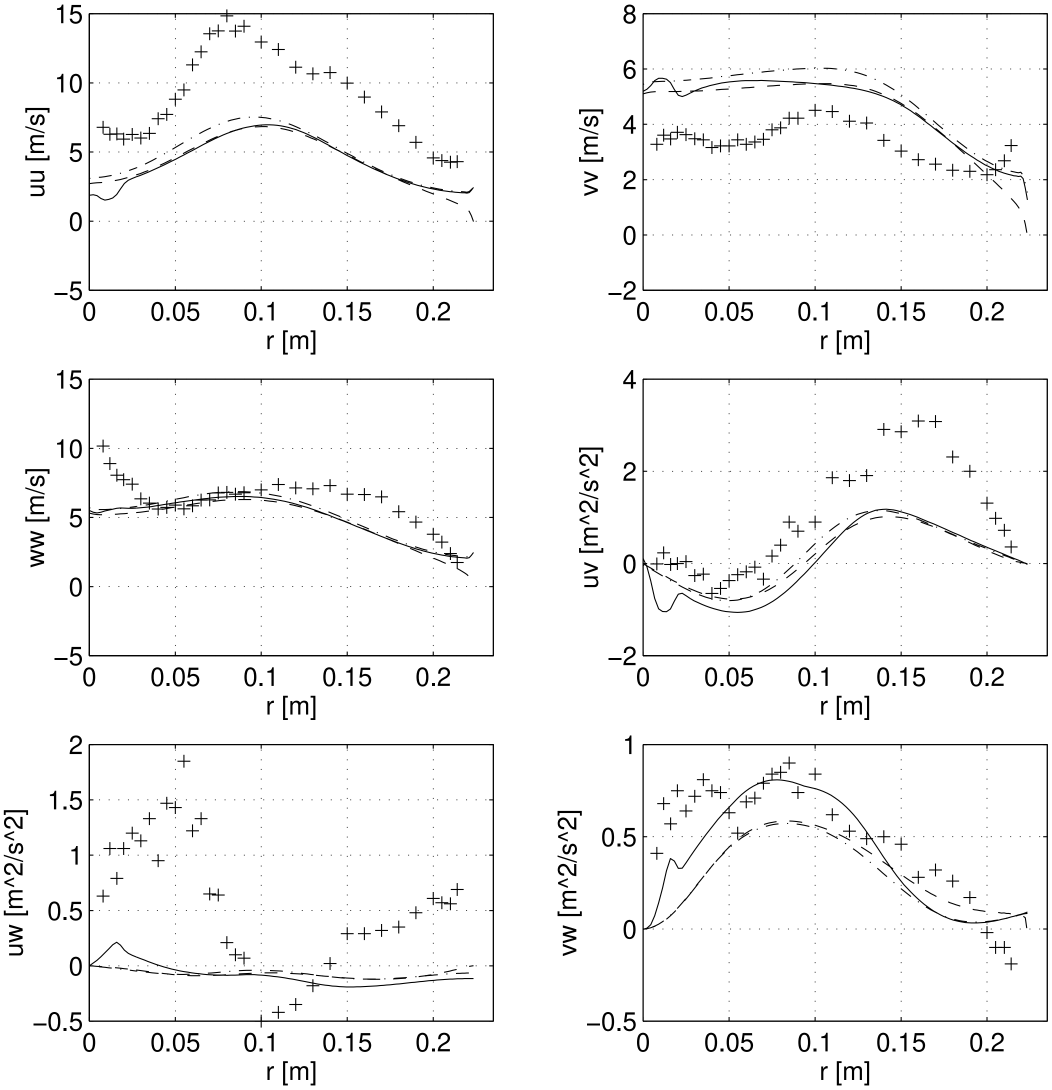

Figure 31: 220 mm downstream, $-\cdot-RNG-k-\epsilon$, $---RNG-k-\epsilon$ with wallfcns, — $RNG-k-\epsilon$ with swirl mod., + Holzöpfel[13]

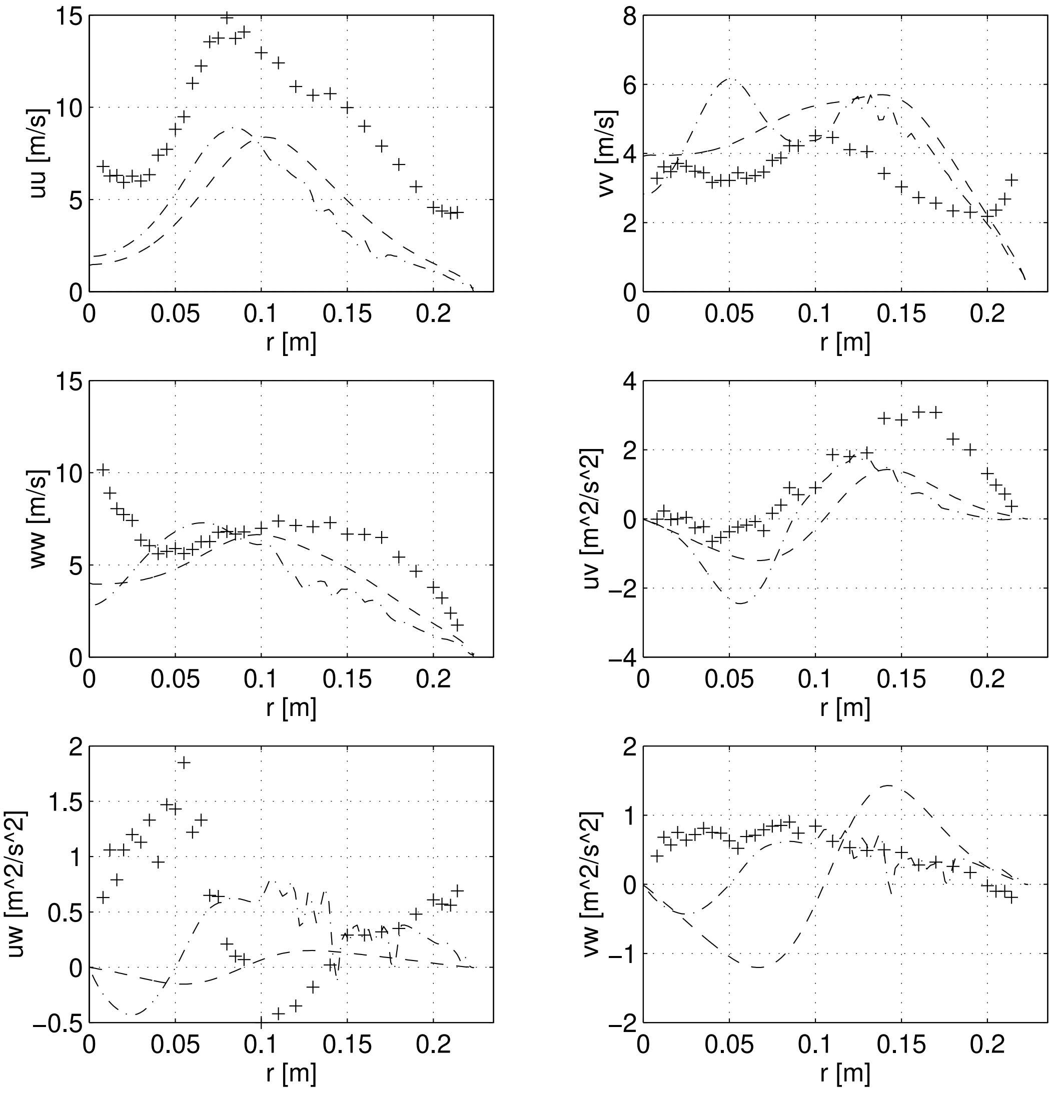

Figure 32: 220 mm downstream, $-\cdot-$non-linear $k-\omega$, $---k-\omega$, + Holzöpfel[13]

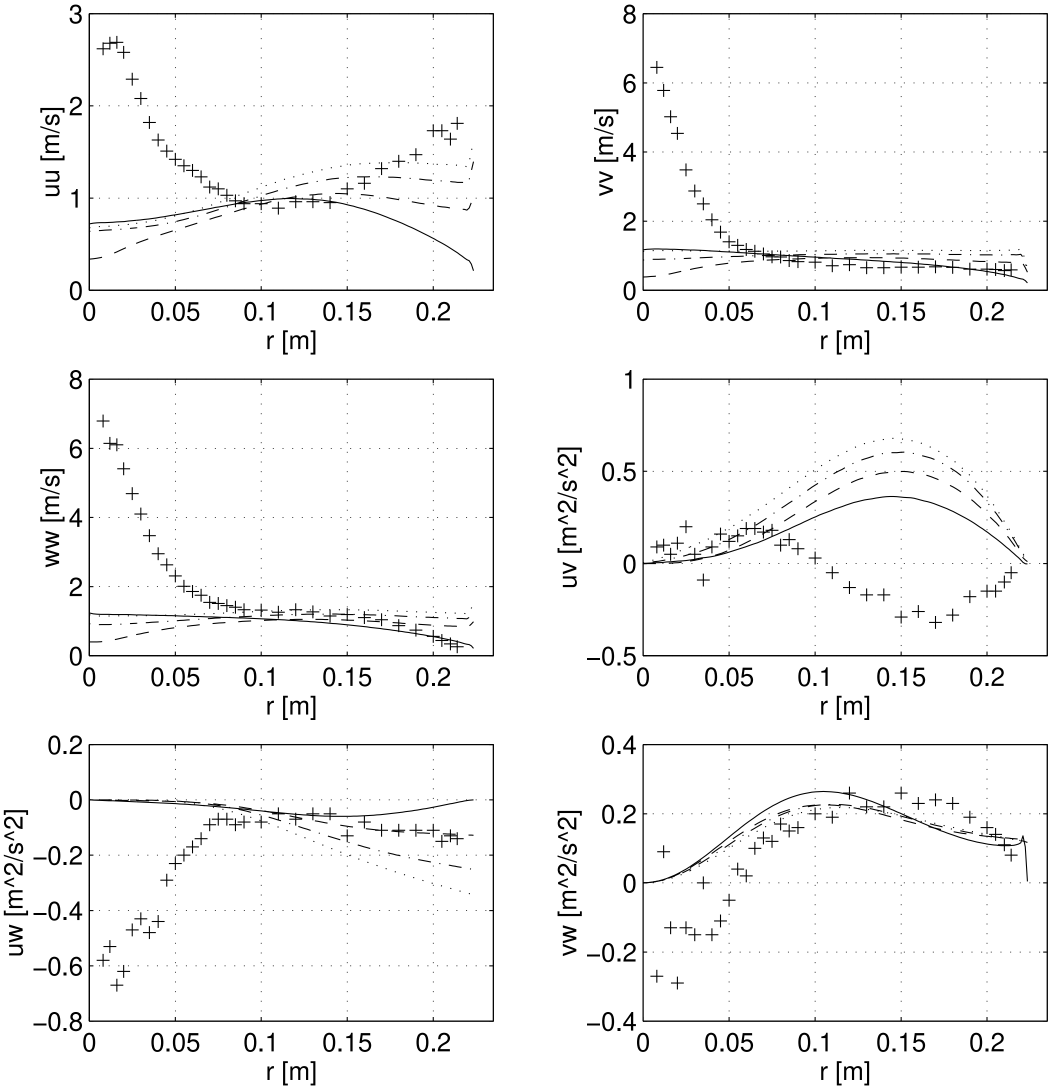

Figure 33: 520 mm downstream, $\cdots k-\epsilon$, $-\cdot- k-\epsilon \quad RN = 0.002$, $--- k-\epsilon \quad RN = 0.008$, — $k-\epsilon$ with wallfcn, + Holzöpfel[13]

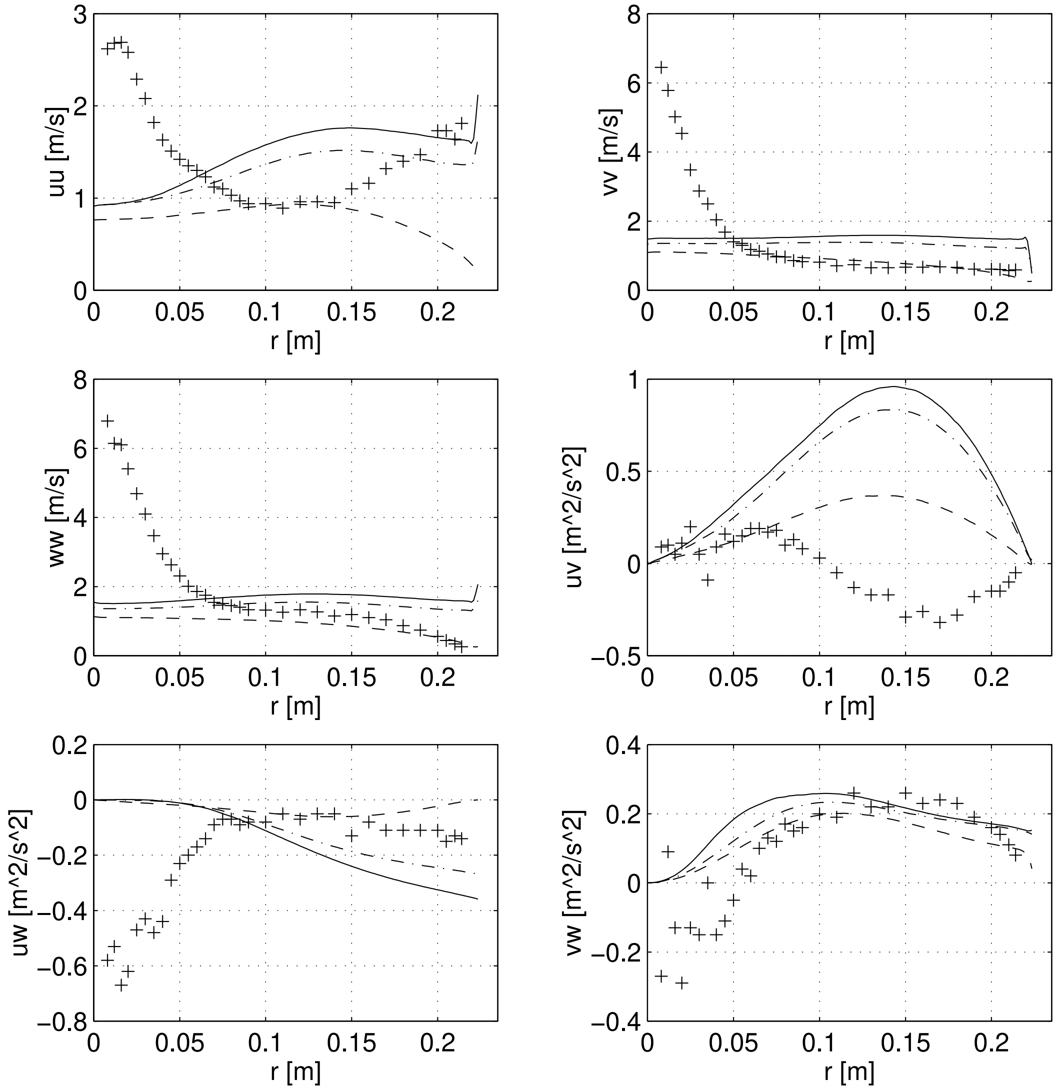

Figure 34: 520 mm downstream, $-\cdot-RNG-k-\epsilon$, $---RNG-k-\epsilon$ with wallfcns, — $RNG-k-\epsilon$ with swirl mod., + Holzöpfel[13]

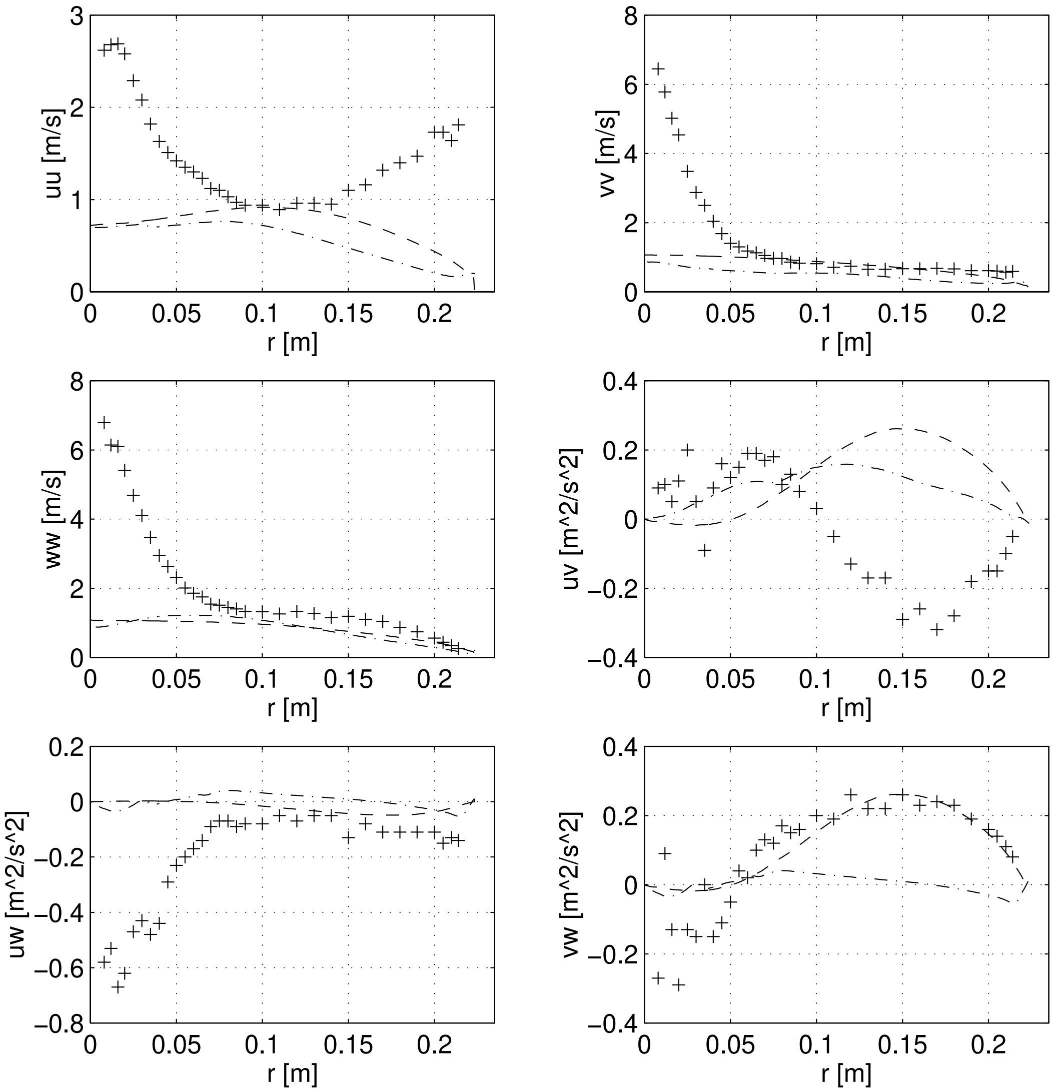

Figure 35: 520 mm downstream, $- \cdot -$non-linear $k-\omega$, $---k-\omega$, + Holzöpfel[13]

D Measured Velocity Field, $S = 0.95$

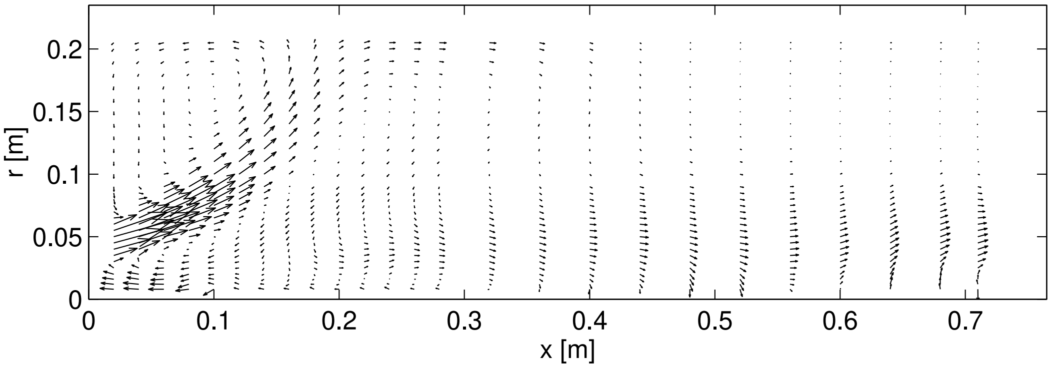

Figure 36: The measured 2D axisymmetric flow case for swirl number $S = 0.95$

E Velocity Profiles, $S = 0.95$

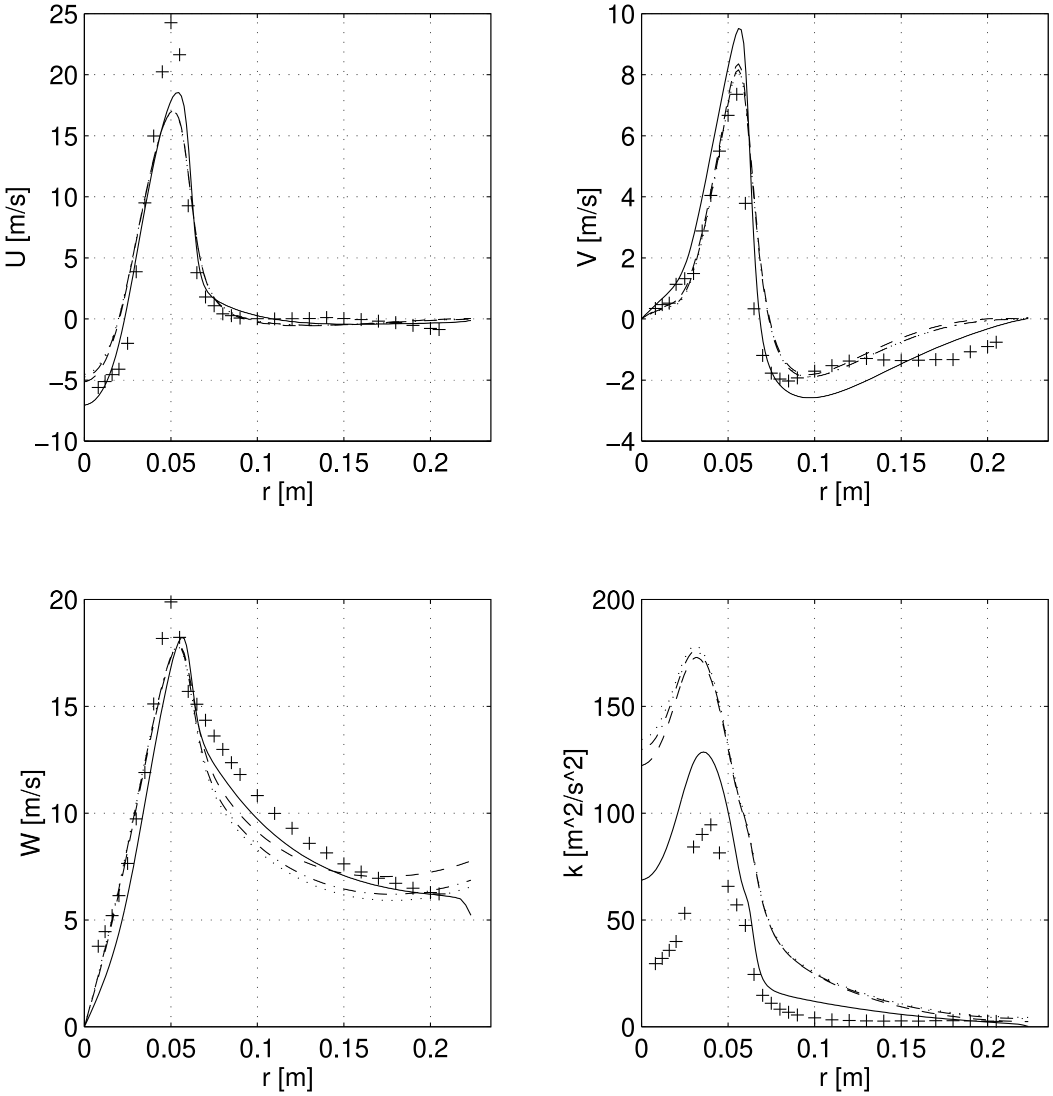

Figure 37: 20 mm downstream, $\cdots k-\epsilon$, $-\cdot- k-\epsilon \quad RN = 0.002$, $--- k-\epsilon \quad RN = 0.008$, — $k-\epsilon$ with wallfcn, + Holzöpfel[13]

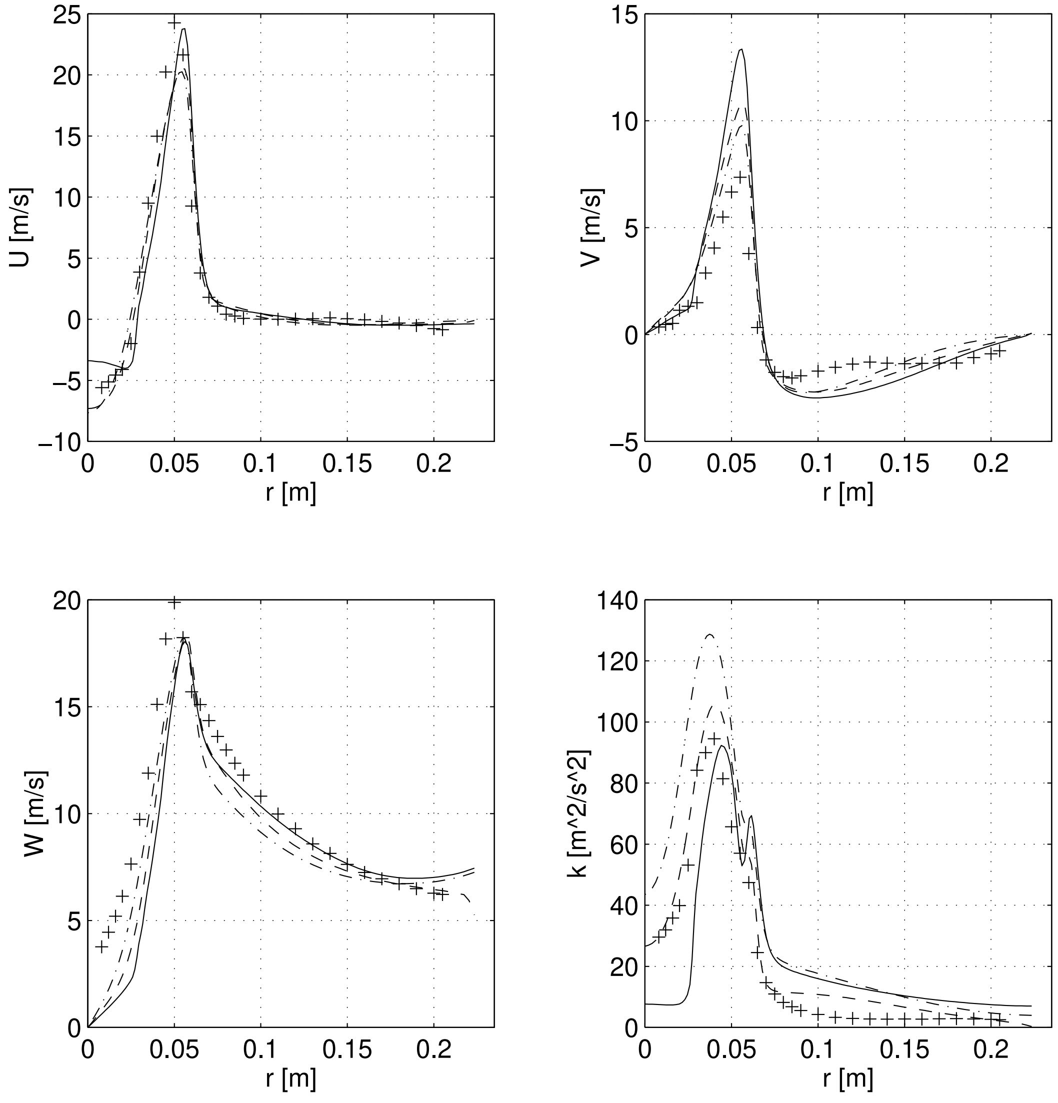

Figure 38: 20 mm downstream, $- \cdot - RNG - k - \epsilon$, $- - - RNG - k - \epsilon$ with wallfcns, — $RNG - k - \epsilon$ with swirl mod., + Holzöpfel[13]

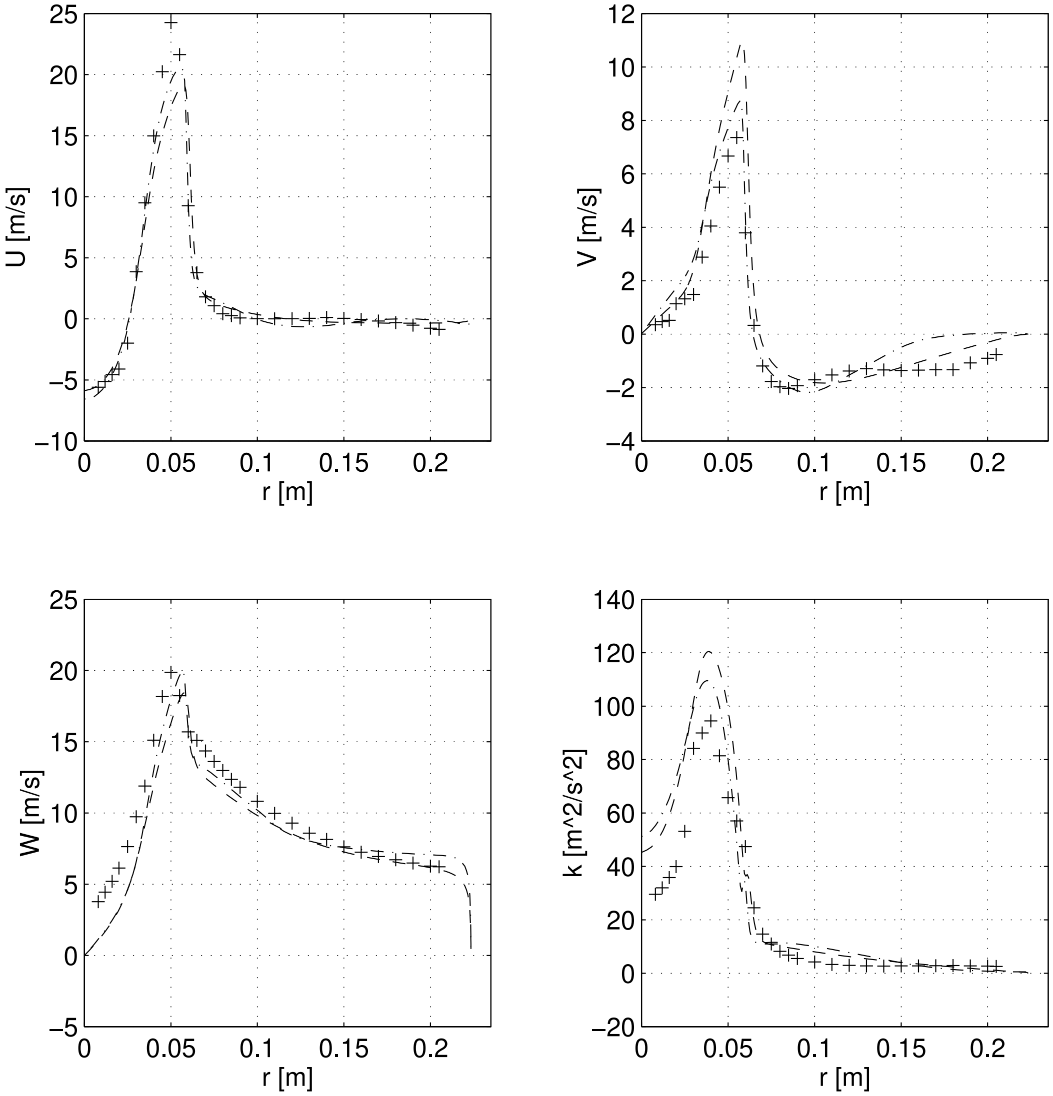

Figure 39: 20 mm downstream, $-\cdot-$non-linear $k-\omega$, $---k-\omega$, + Holzöpfel[13]

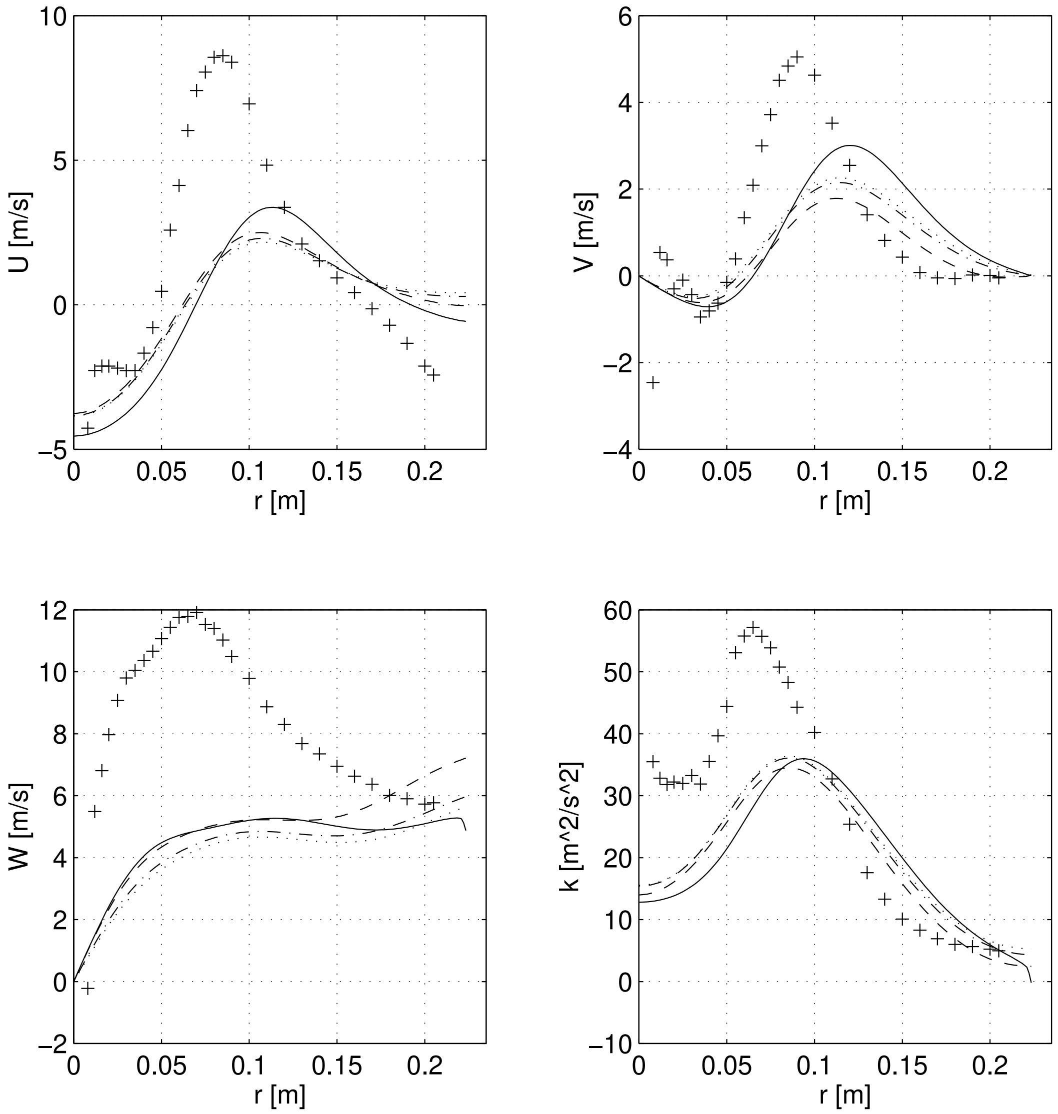

Figure 40: 100 mm downstream, $\cdots k-\epsilon$, $-\cdot- k-\epsilon \quad RN = 0.002$, $--- k-\epsilon \quad RN = 0.008$, — $k-\epsilon$ with wallfcn, + Holzöpfel[13]

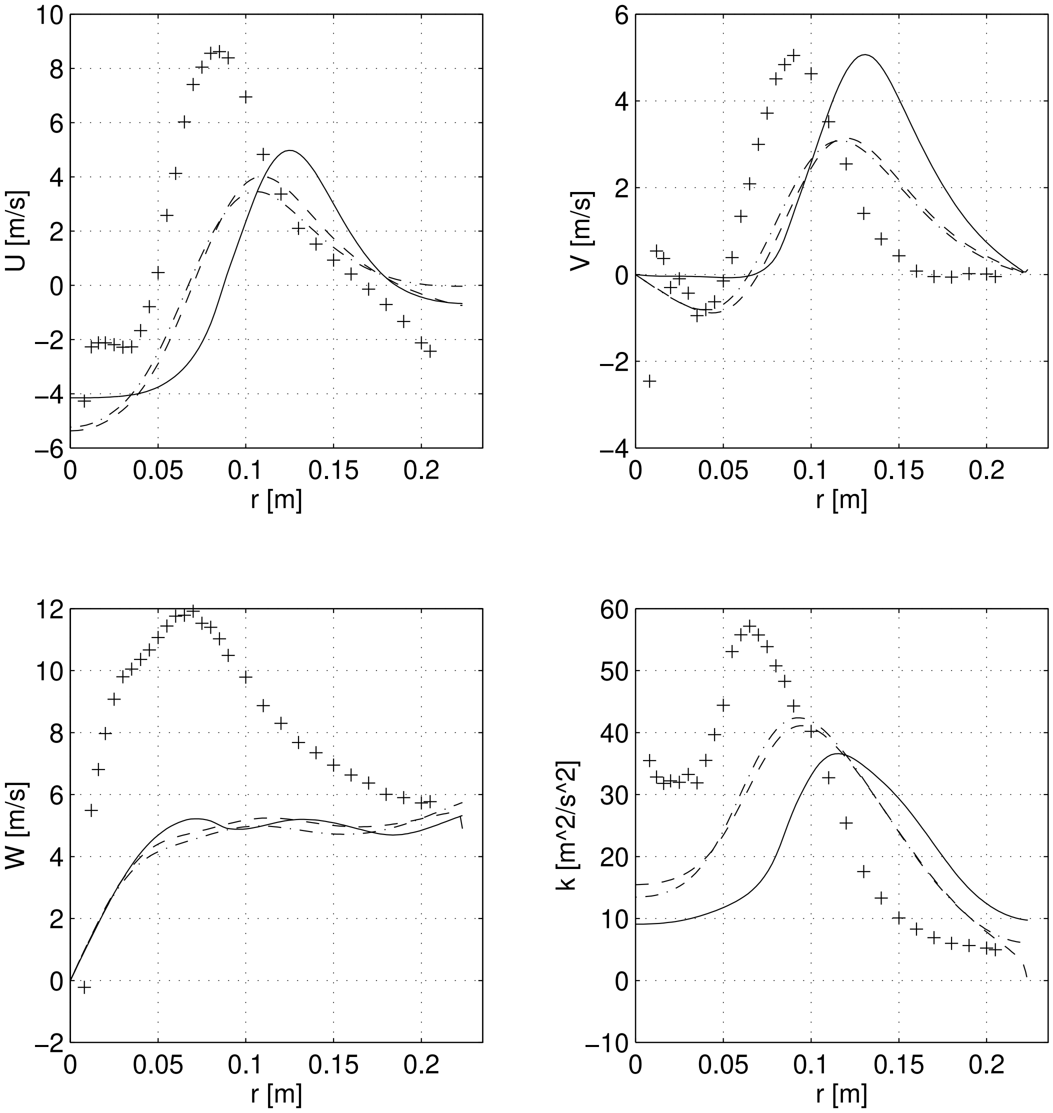

Figure 41: 100 mm downstream, $- \cdot - RNG - k - \epsilon$, $- - - RNG - k - \epsilon$ with wallfcns, — $RNG - k - \epsilon$ with swirl mod., + Holzöpfel[13]

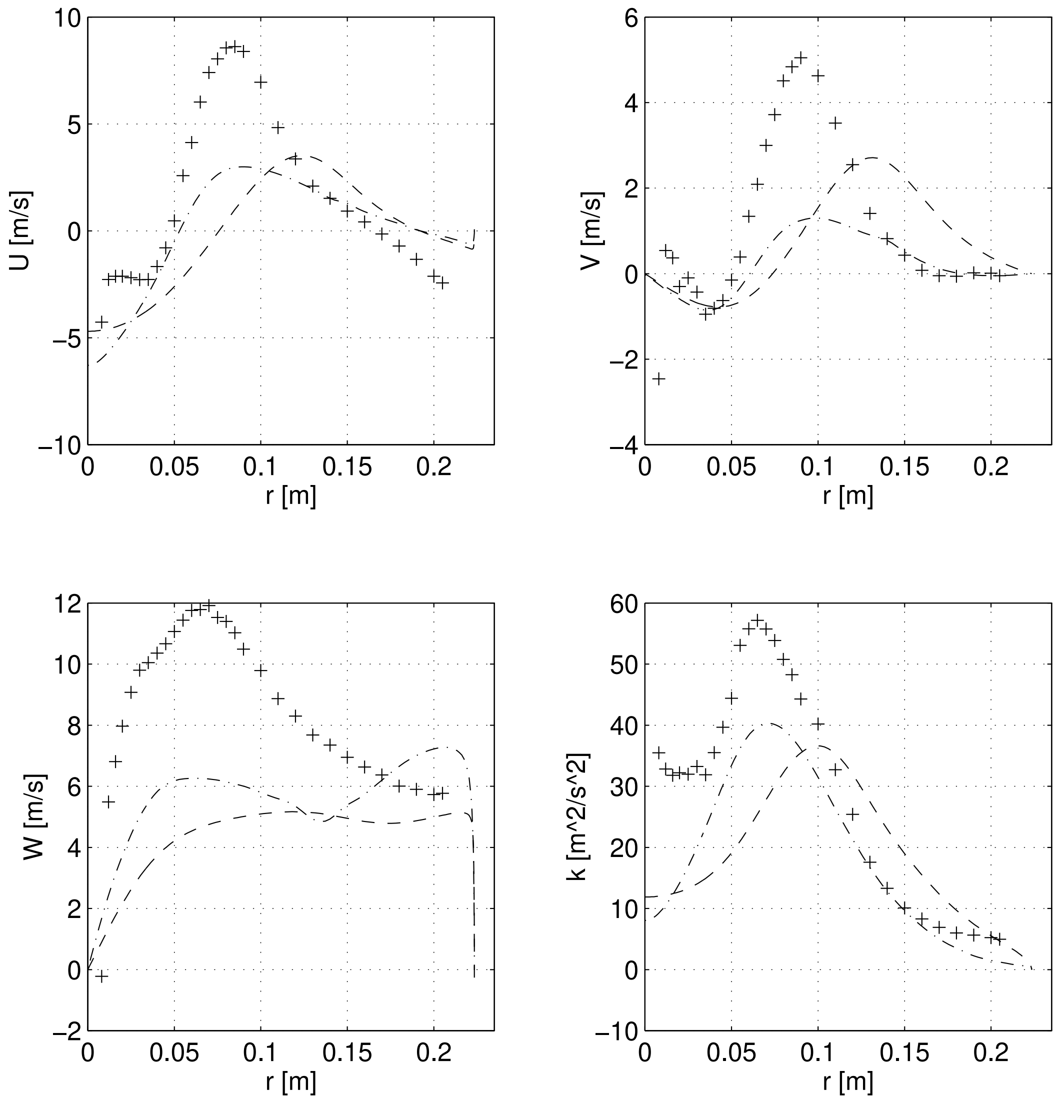

Figure 42: 100 mm downstream, $-\cdot-$non-linear $k-\omega$, $---k-\omega$, + Holzöpfel[13]

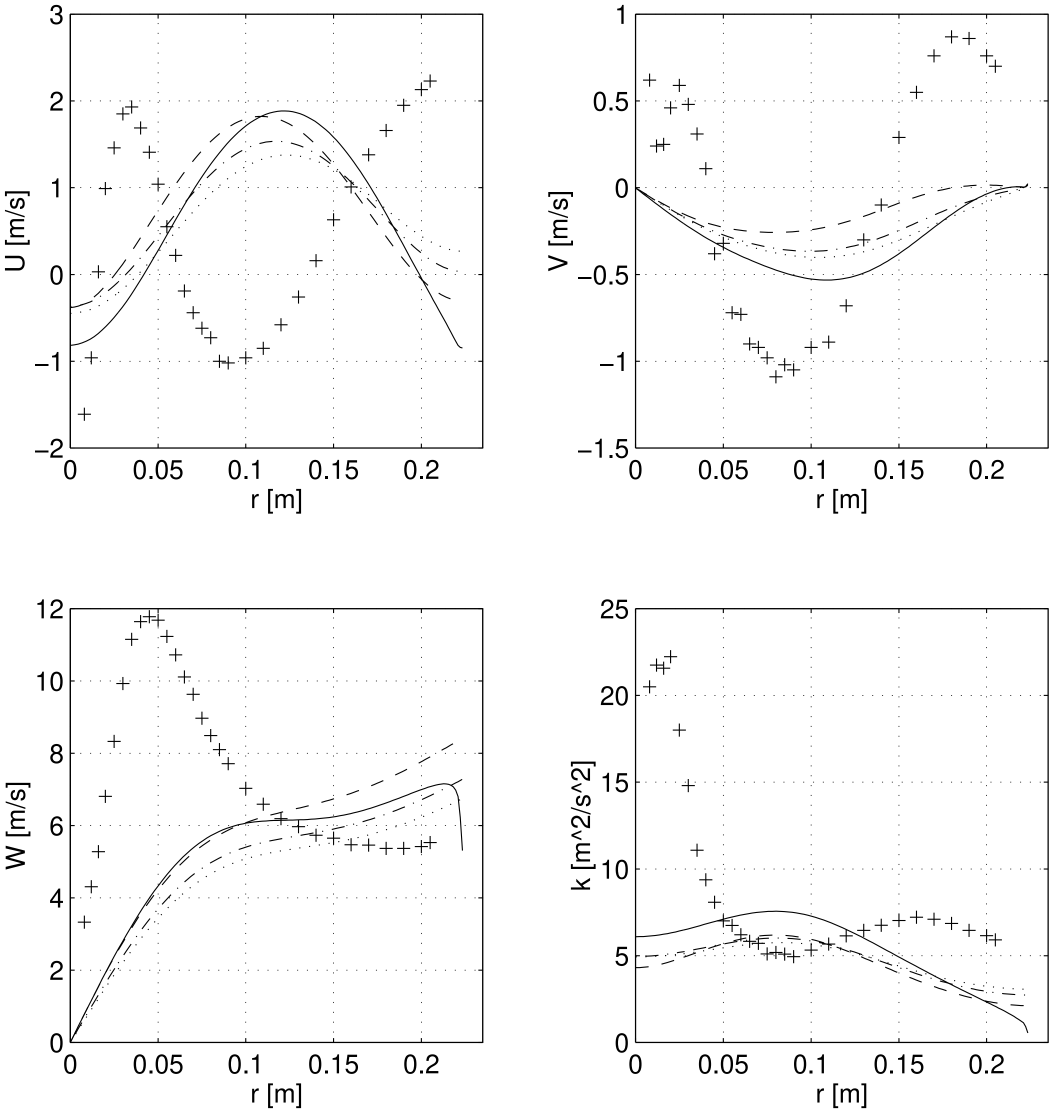

Figure 43: 220 mm downstream, $\cdots k-\epsilon$, $-\cdot- k-\epsilon \quad RN = 0.002$, $--- k-\epsilon \quad RN = 0.008$, — $k-\epsilon$ with wallfcn, + Holzöpfel[13]

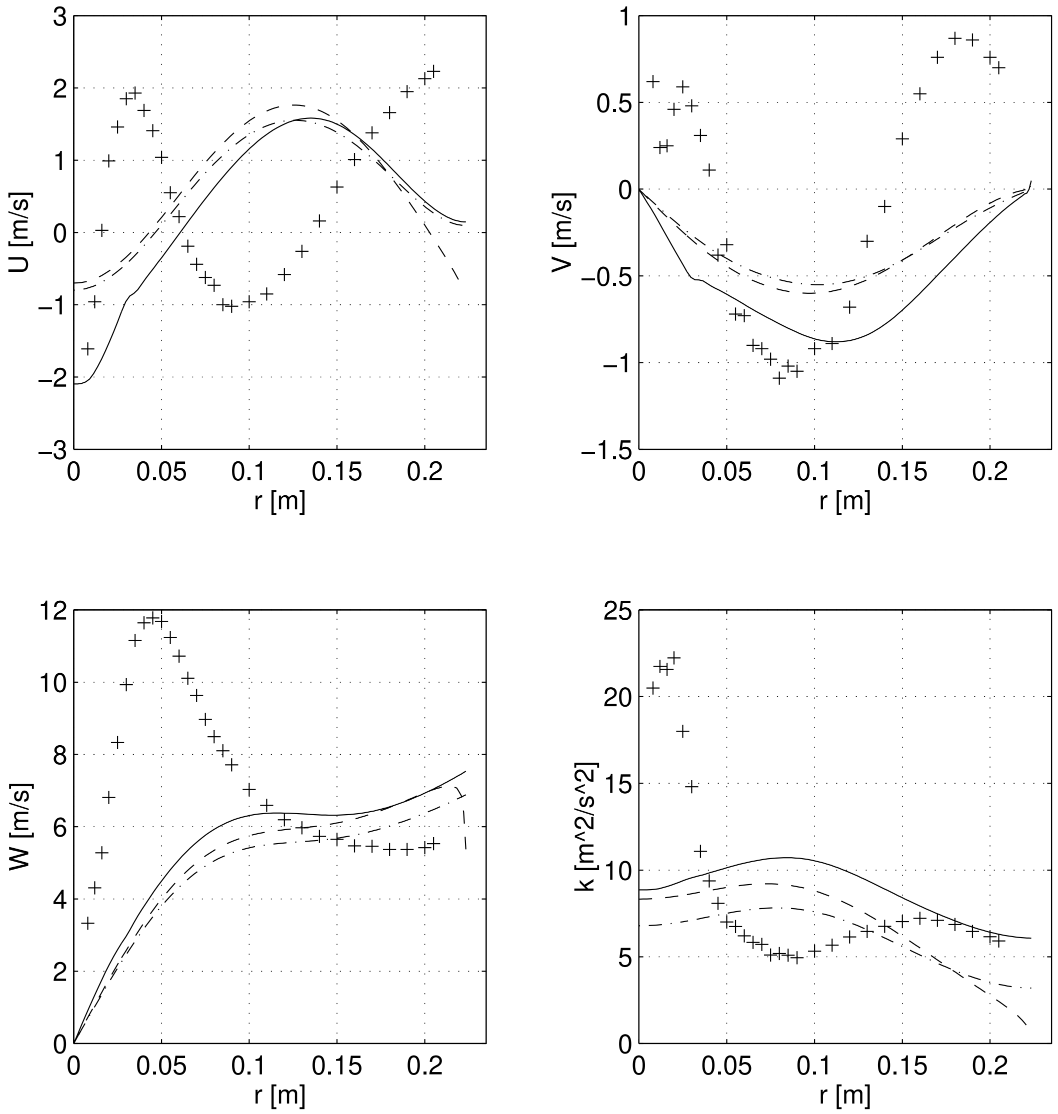

Figure 44: 220 mm downstream, $-\cdot-RNG-k-\epsilon$, $---RNG-k-\epsilon$ with wallfcns, — $RNG-k-\epsilon$ with swirl mod., + Holzöpfel[13]

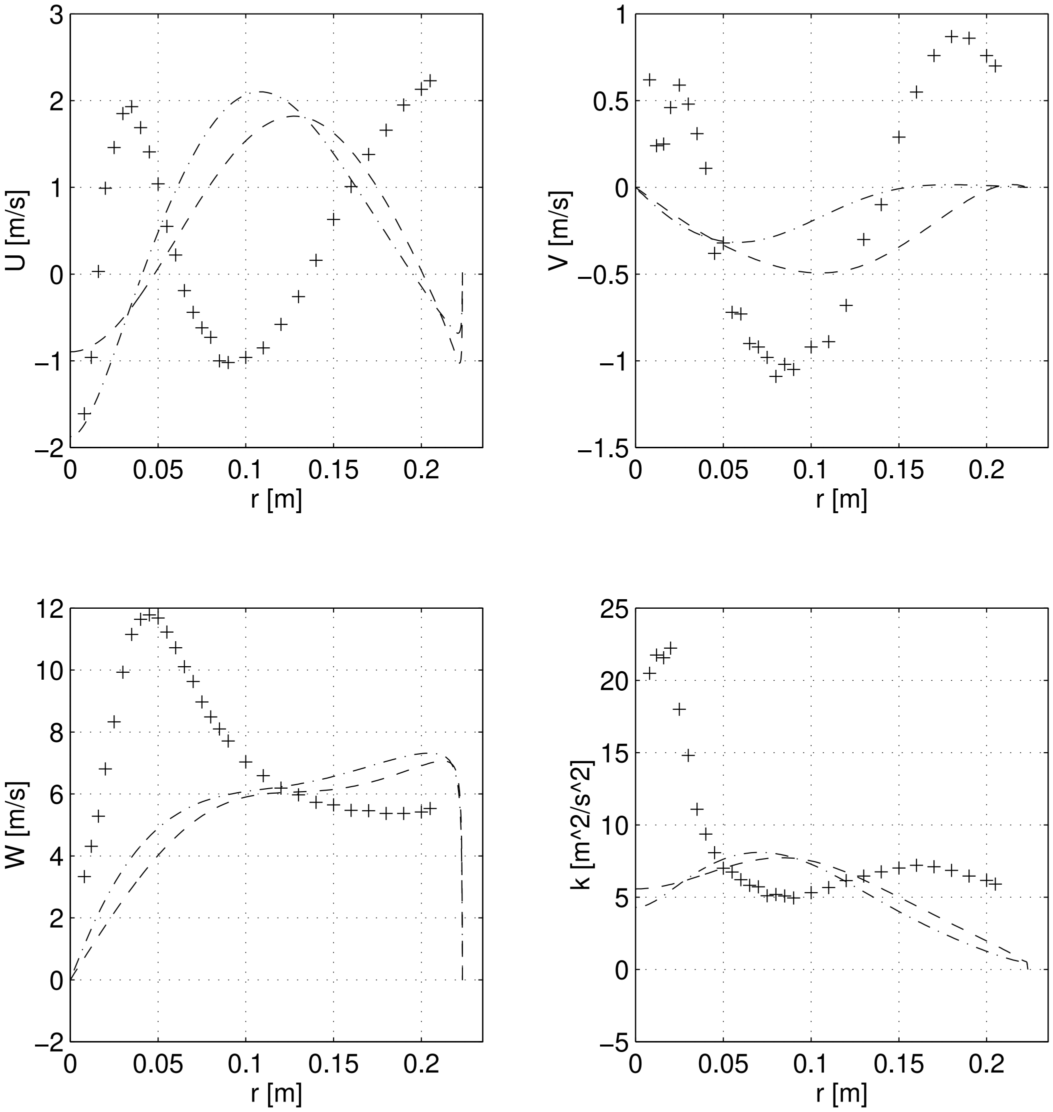

Figure 45: 220 mm downstream, $-\cdot-$non-linear $k-\omega$, $---k-\omega$, + Holzöpfel[13]

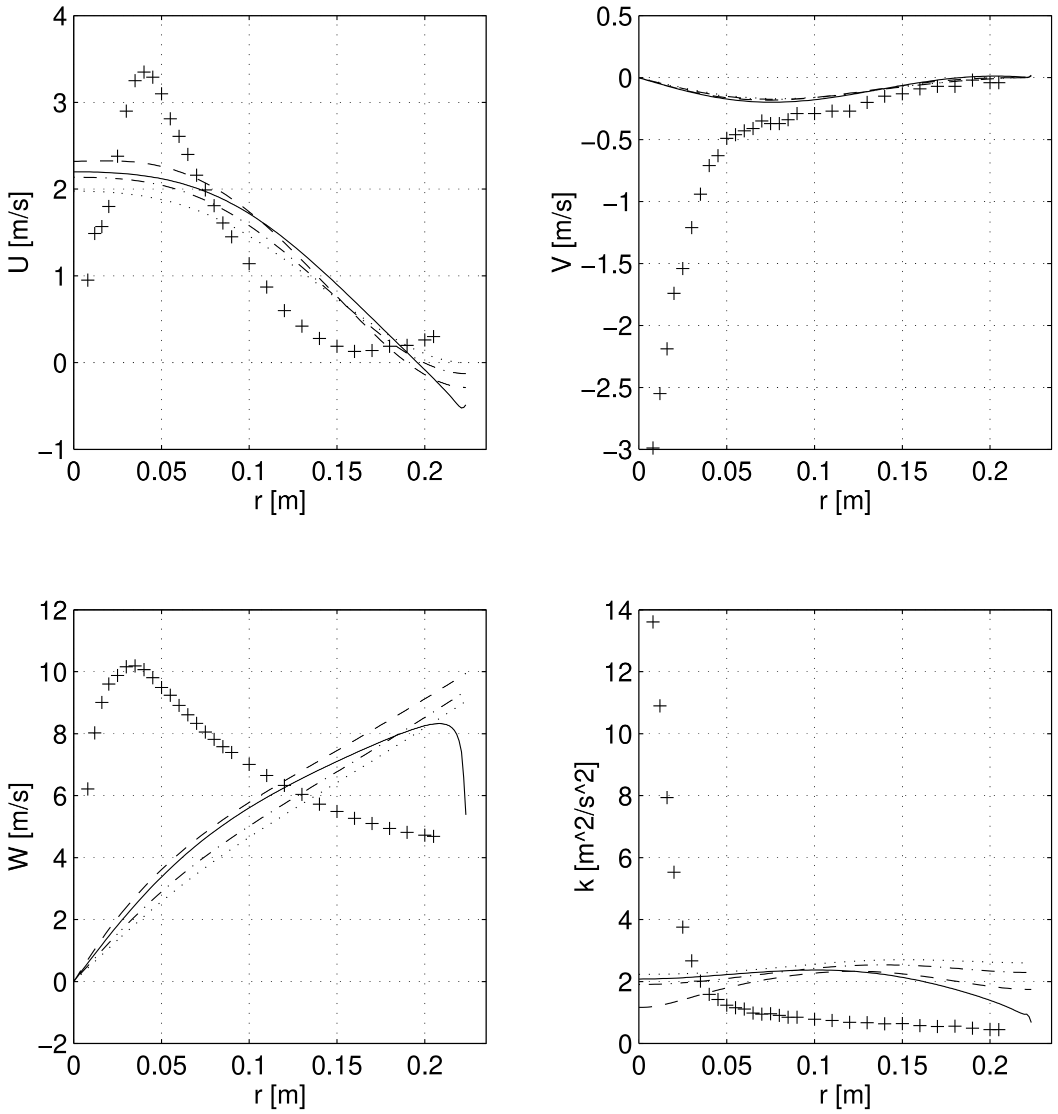

Figure 46: 520 mm downstream, $\cdots k-\epsilon$, $-\cdot- k-\epsilon \quad RN = 0.002$, $--- k-\epsilon \quad RN = 0.008$, — $k-\epsilon$ with wallfcn, + Holzöpfel[13]

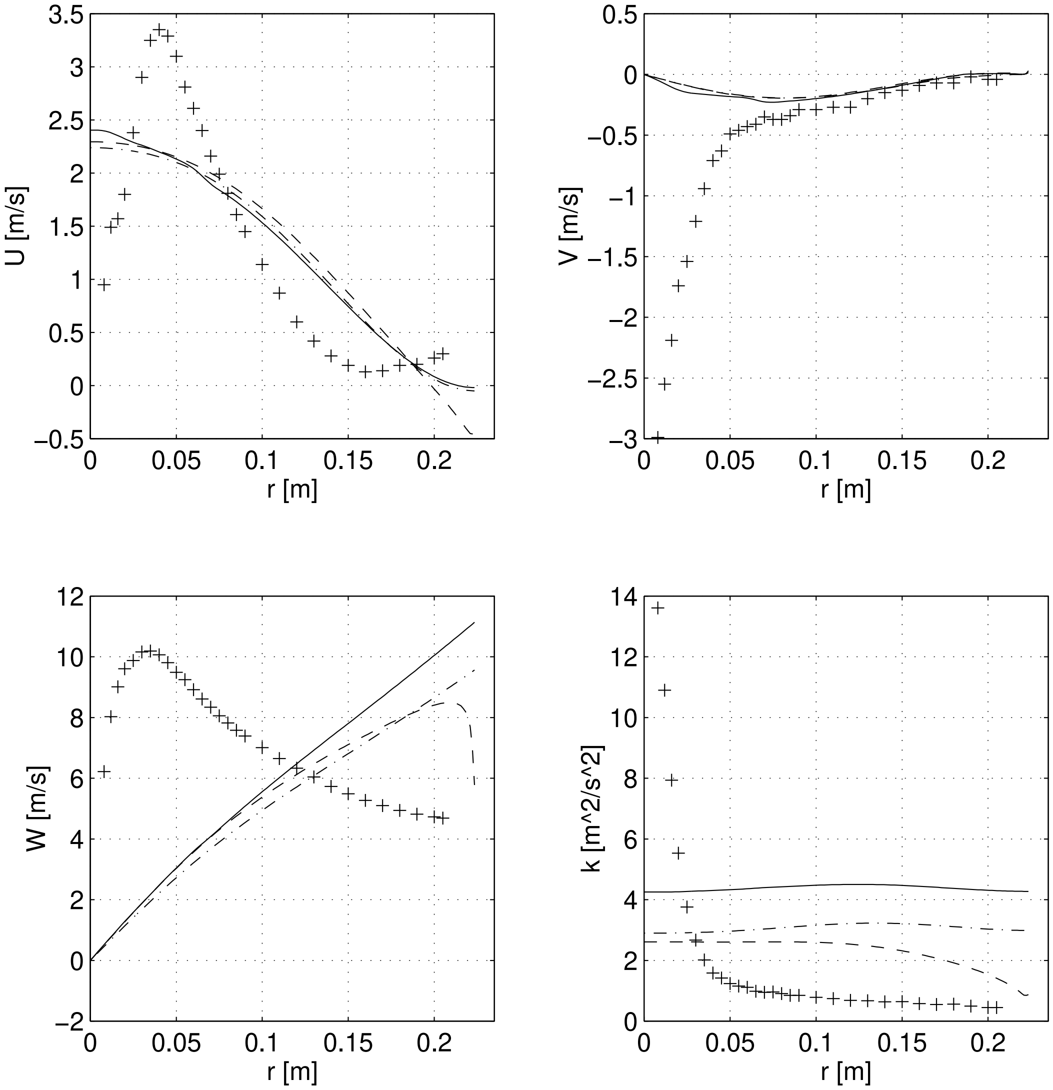

Figure 47: 520 mm downstream, $-\cdot-RNG-k-\epsilon$, $---RNG-k-\epsilon$ with wallfcns, — $RNG-k-\epsilon$ with swirl mod., + Holzöpfel[13]

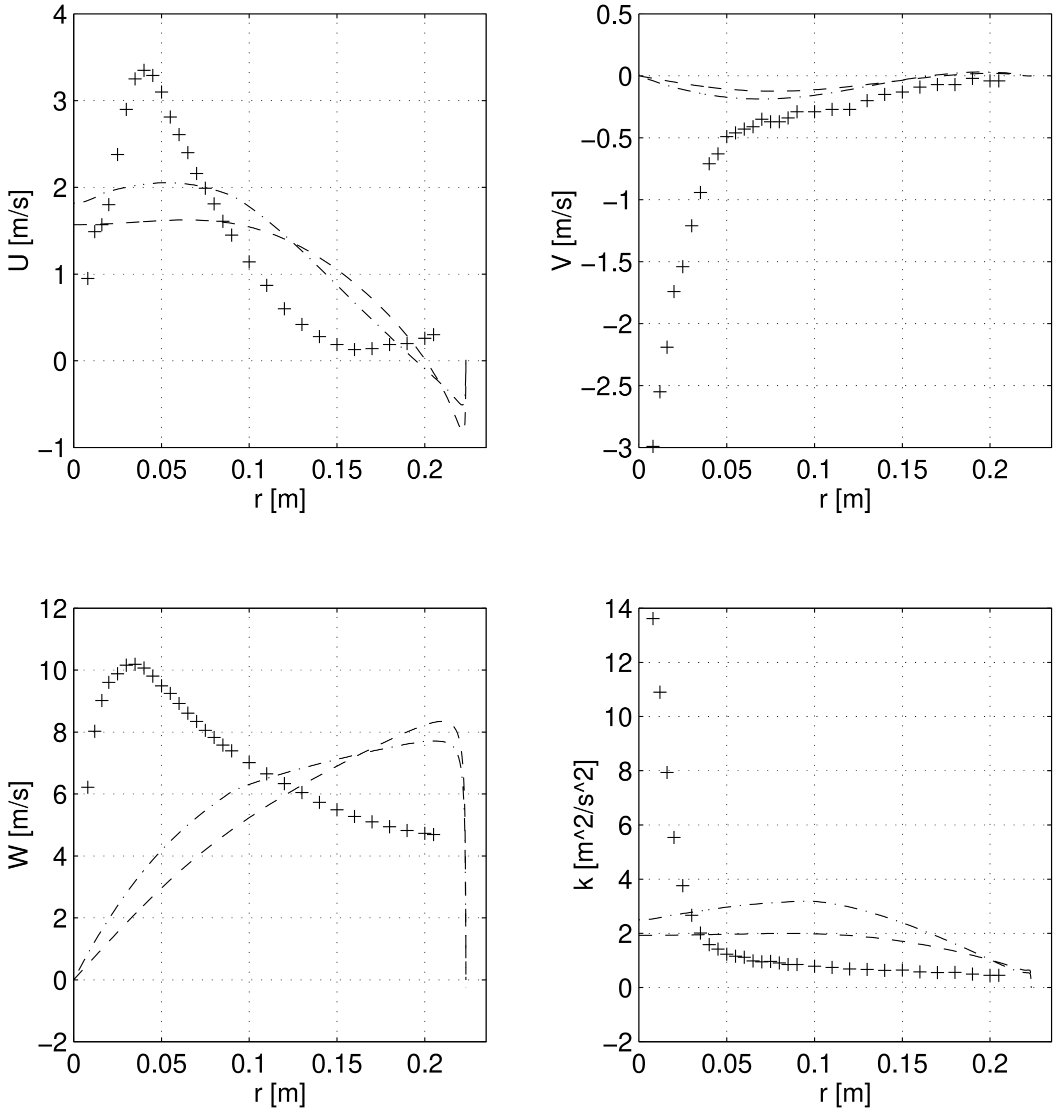

Figure 48: 520 mm downstream, $- \cdot -$non-linear $k - \omega$, $- - - k - \omega$, + Holzöpfel[13]

F Velocity Correlations, $S = 0.95$

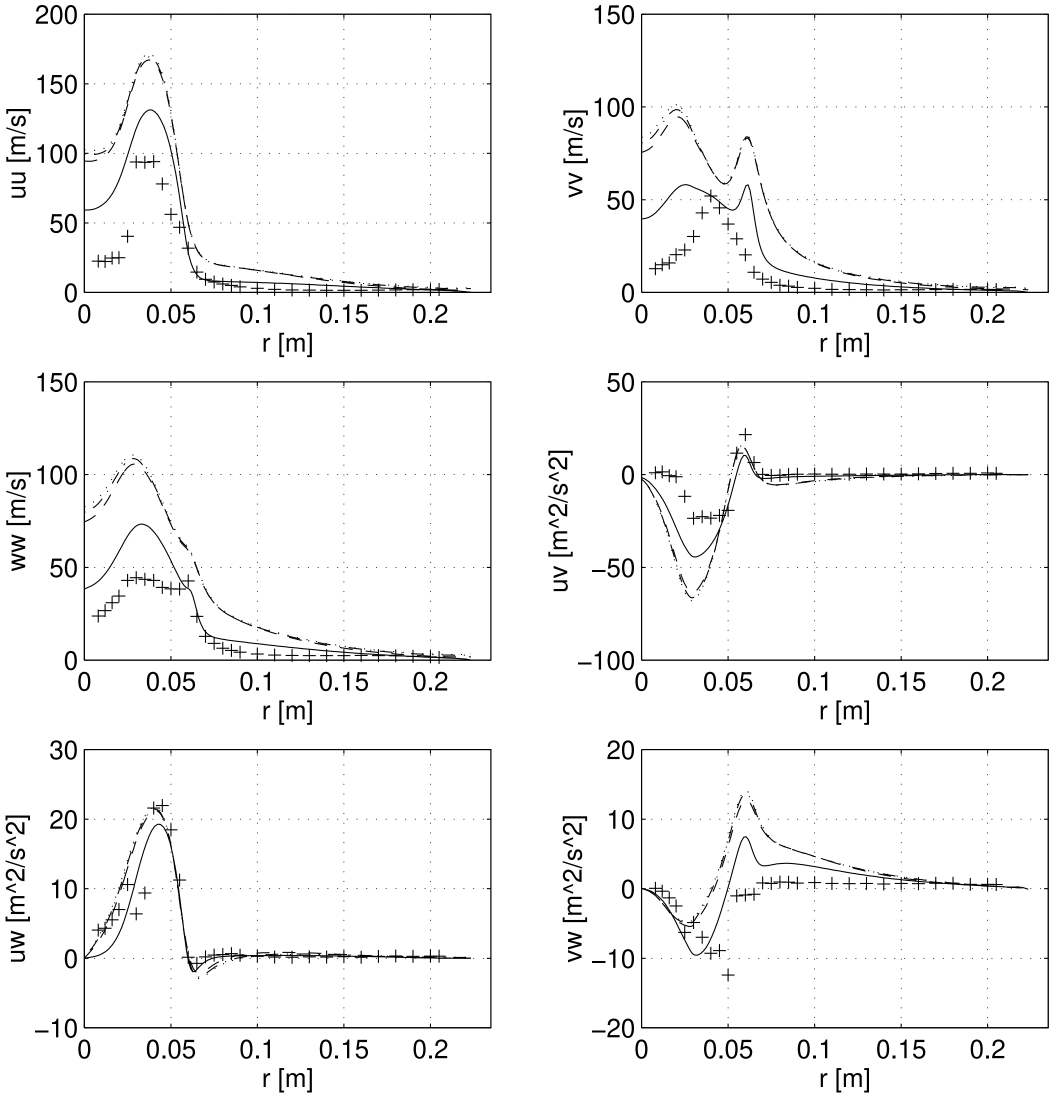

Figure 49: 20 mm downstream, $\cdots k-\epsilon$, $-\cdot- k-\epsilon \quad RN = 0.002$, $--- k-\epsilon \quad RN = 0.008$, — $k-\epsilon$ with wallfcn, + Holzöpfel[13]

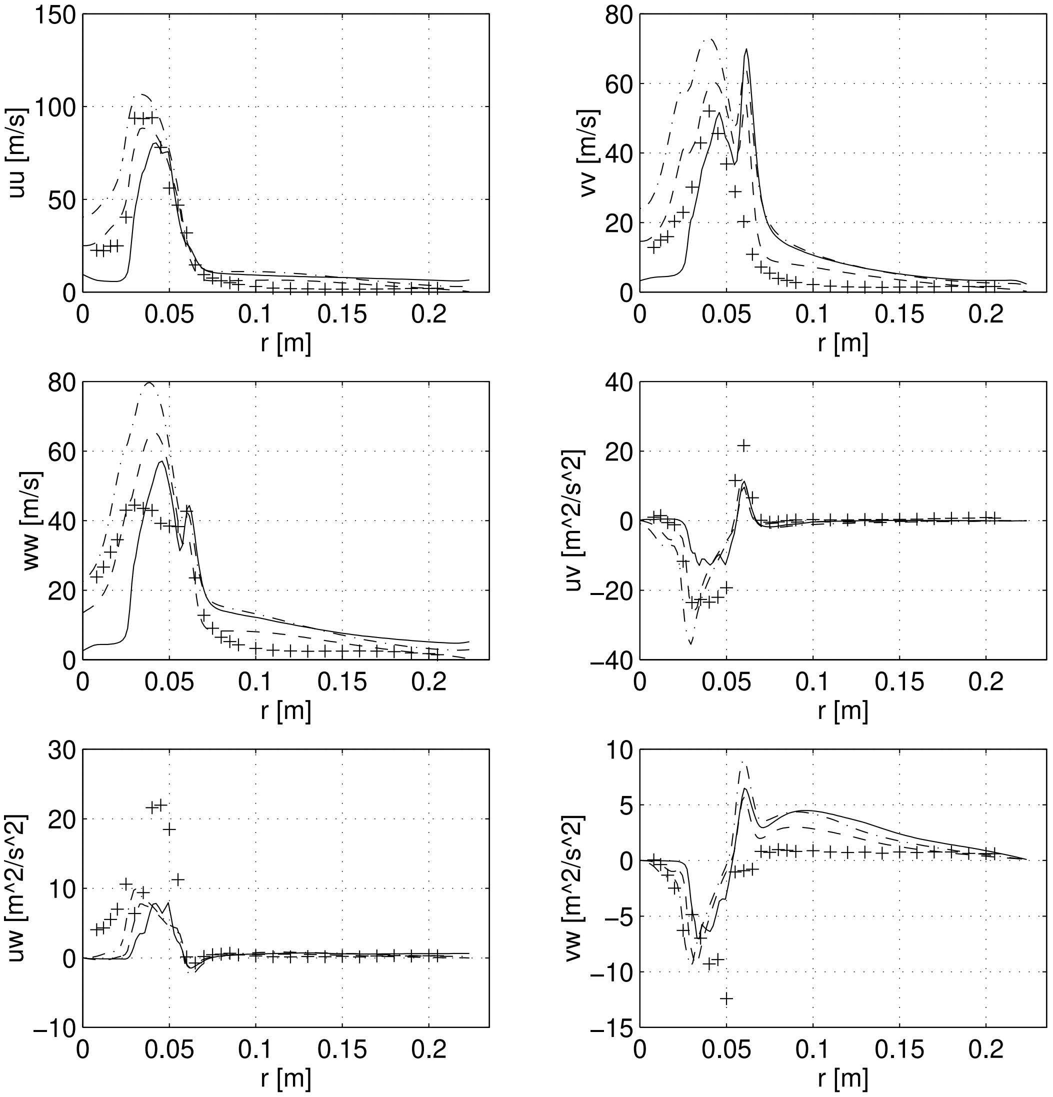

Figure 50: 20 mm downstream, $-\cdot-RNG-k-\epsilon$, $---RNG-k-\epsilon$ with wallfcns, — $RNG-k-\epsilon$ with swirl mod., + Holzöpfel[13]

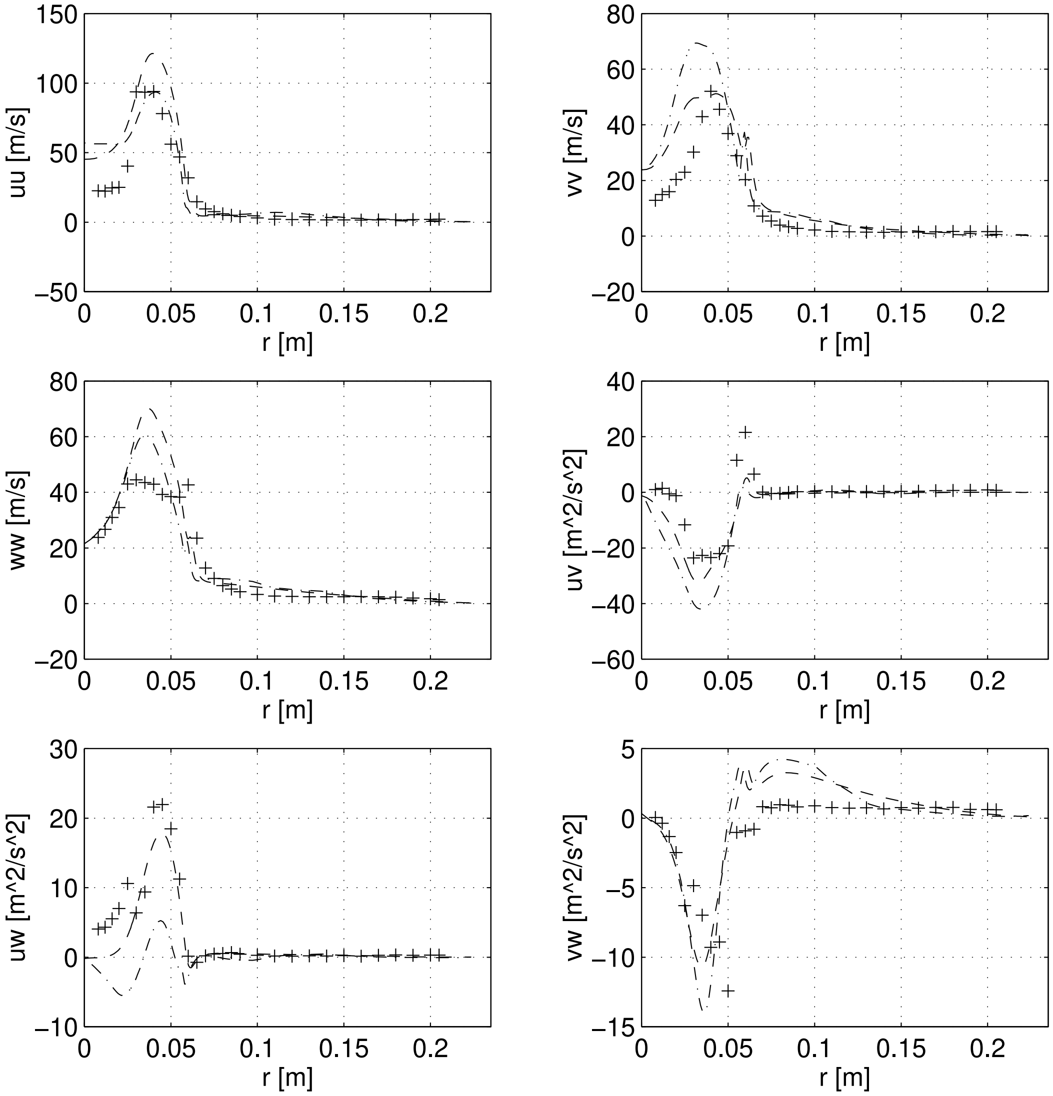

Figure 51: 20 mm downstream, $-\cdot-$non-linear $k-\omega$, $---k-\omega$, + Holzöpfel[13]

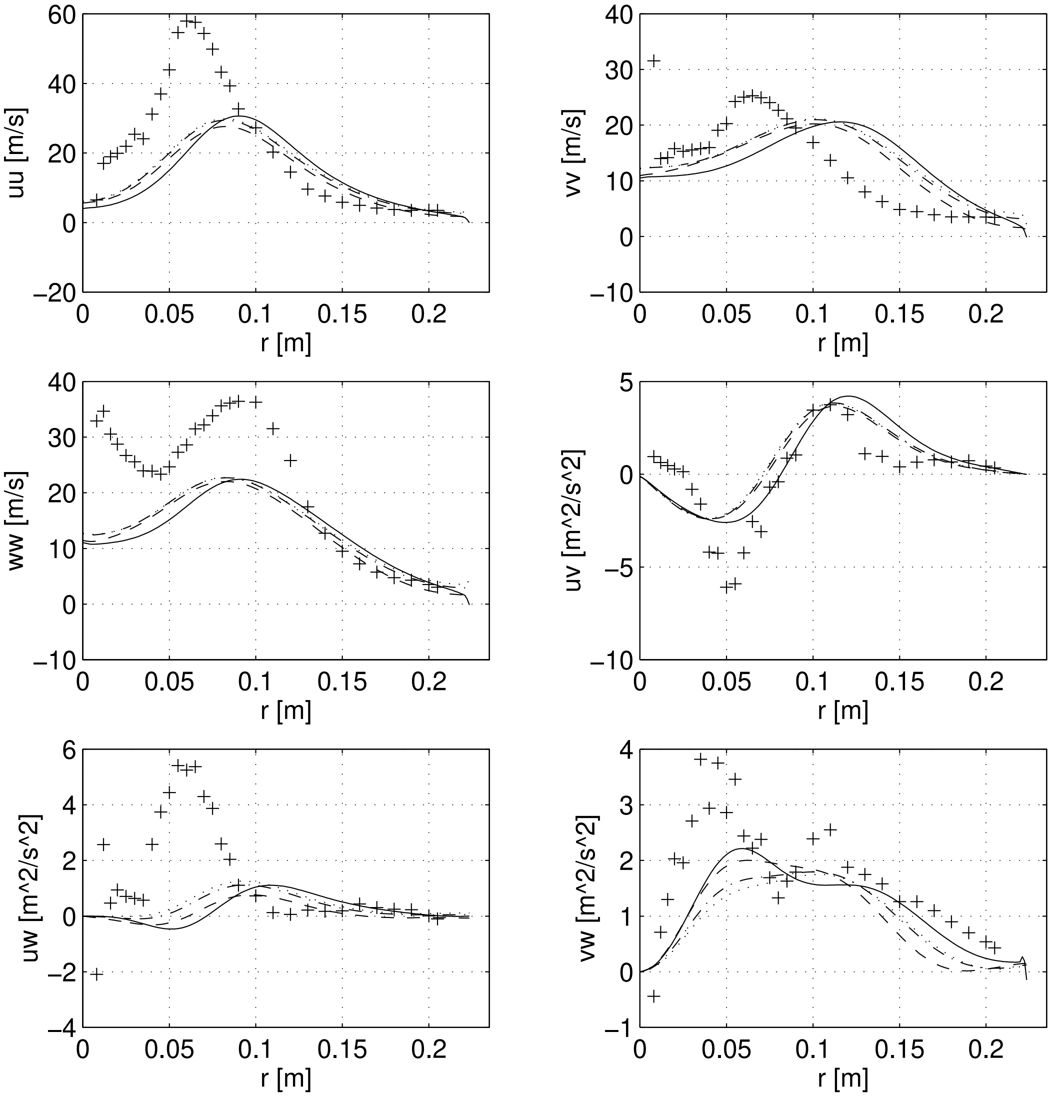

Figure 52: 100 mm downstream, $\cdots k-\epsilon$, $-\cdot- k-\epsilon \quad RN = 0.002$, $--- k-\epsilon \quad RN = 0.008$, — $k-\epsilon$ with wallfcn, + Holzöpfel[13]

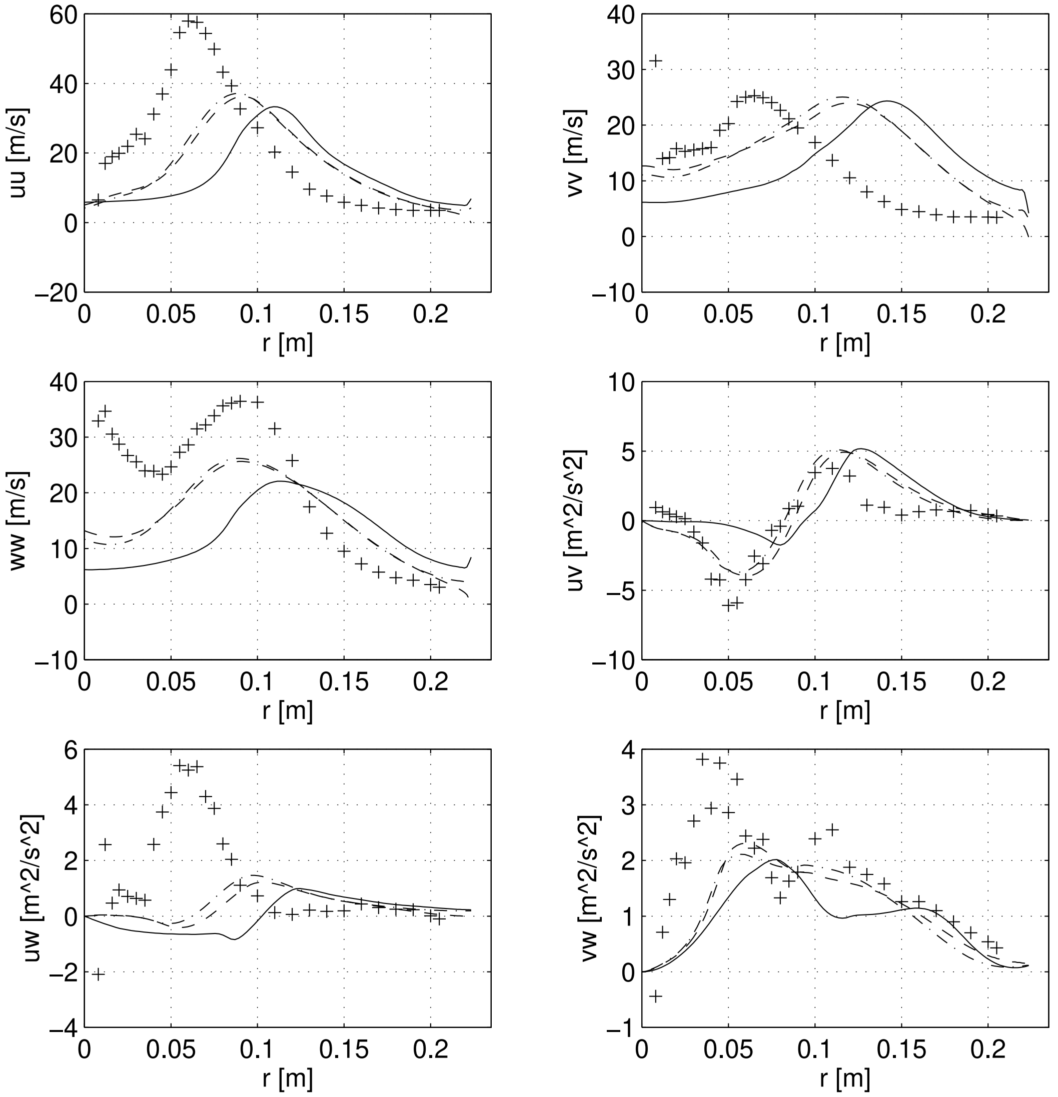

Figure 53: 100 mm downstream, $-\cdot-RNG-k-\epsilon$, $---RNG-k-\epsilon$ with wallfcns, — $RNG-k-\epsilon$ with swirl mod., + Holzöpfel[13]

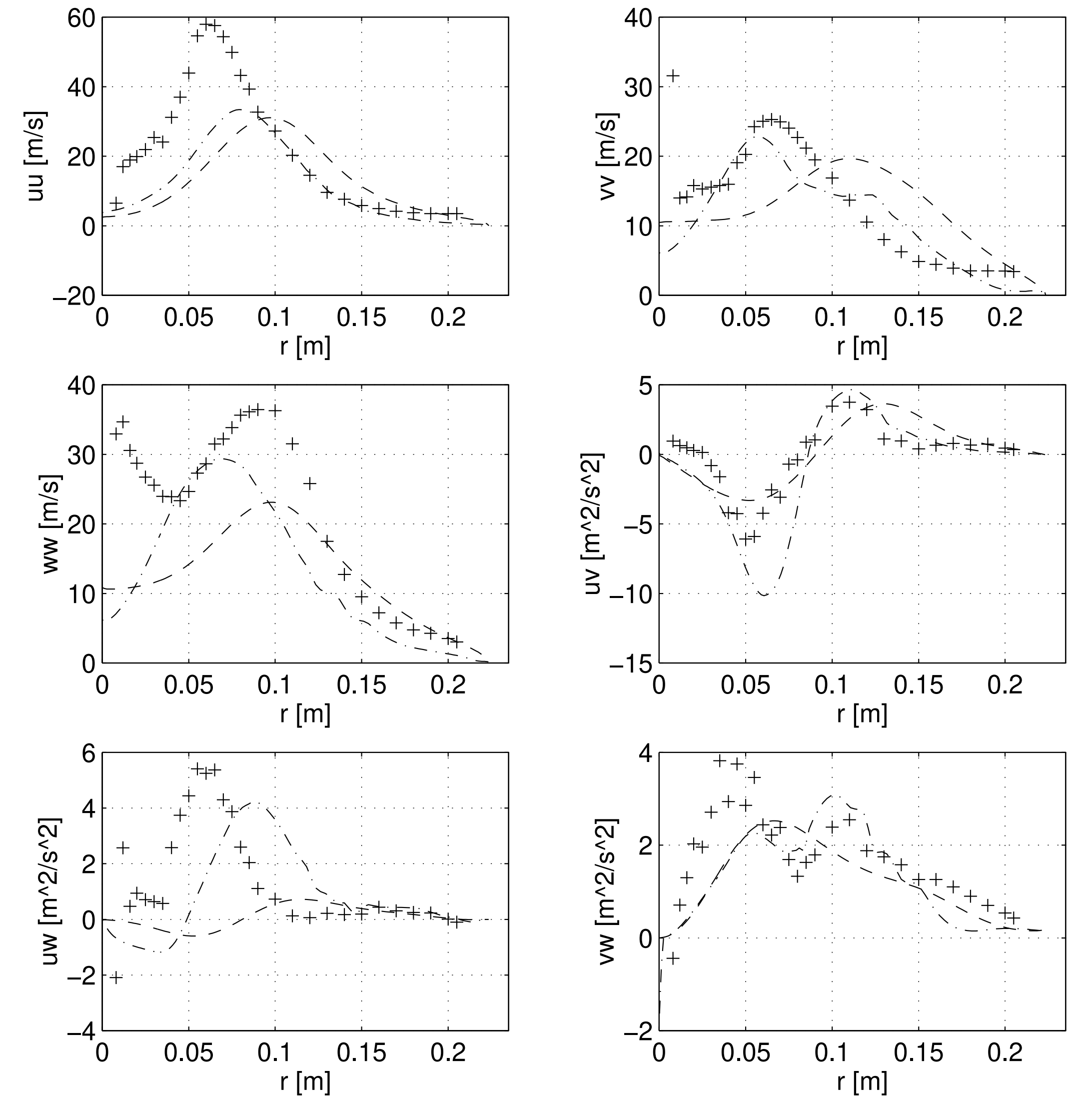

Figure 54: 100 mm downstream, $-\cdot-$non-linear $k-\omega$, $---k-\omega$, + Holzöpfel[13]

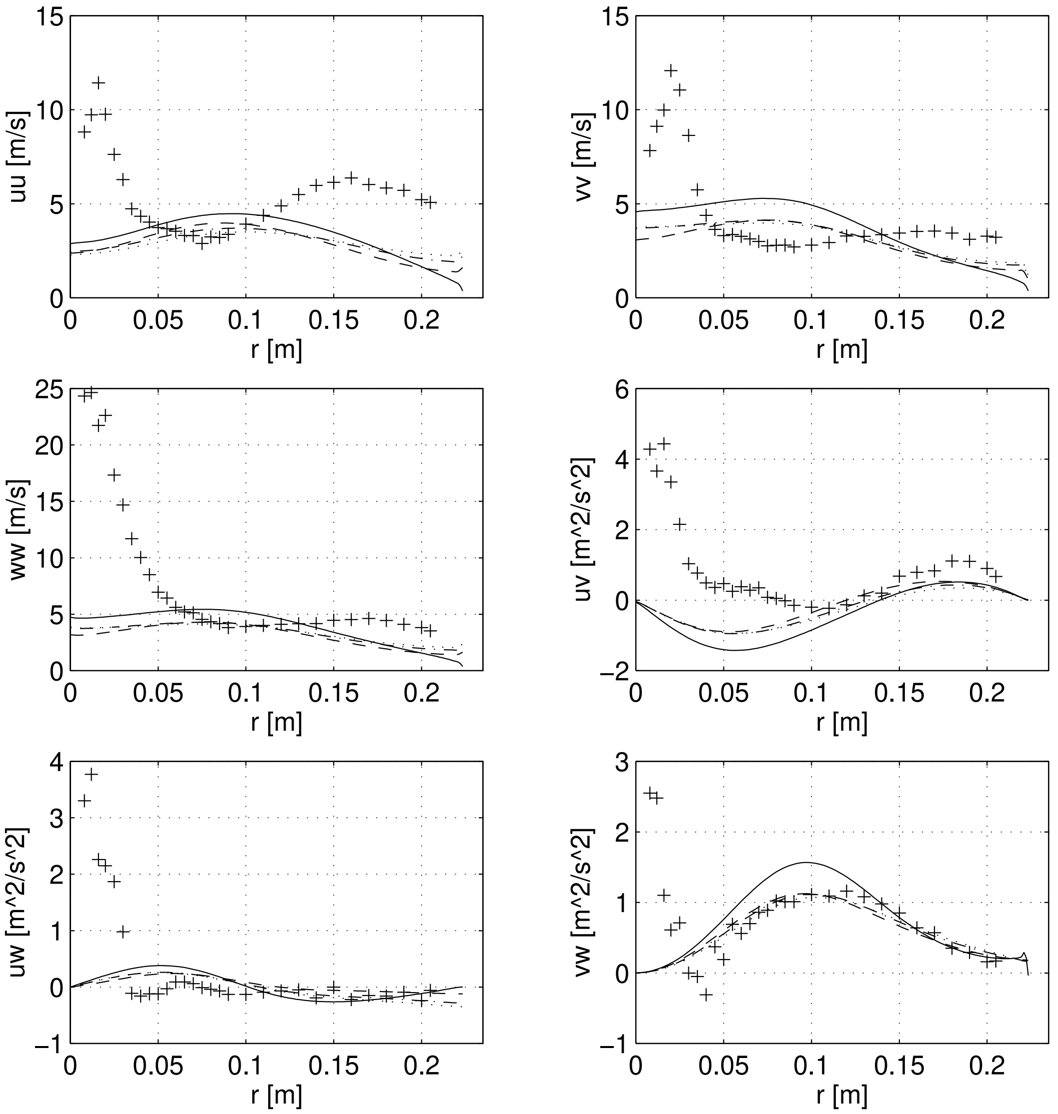

Figure 55: 220 mm downstream, $\cdots k-\epsilon$, $-\cdot-k-\epsilon \quad RN=0.002$, $---k-\epsilon \quad RN=0.008$, — $k-\epsilon$ with wallfcn, + Holzöpfel[13]

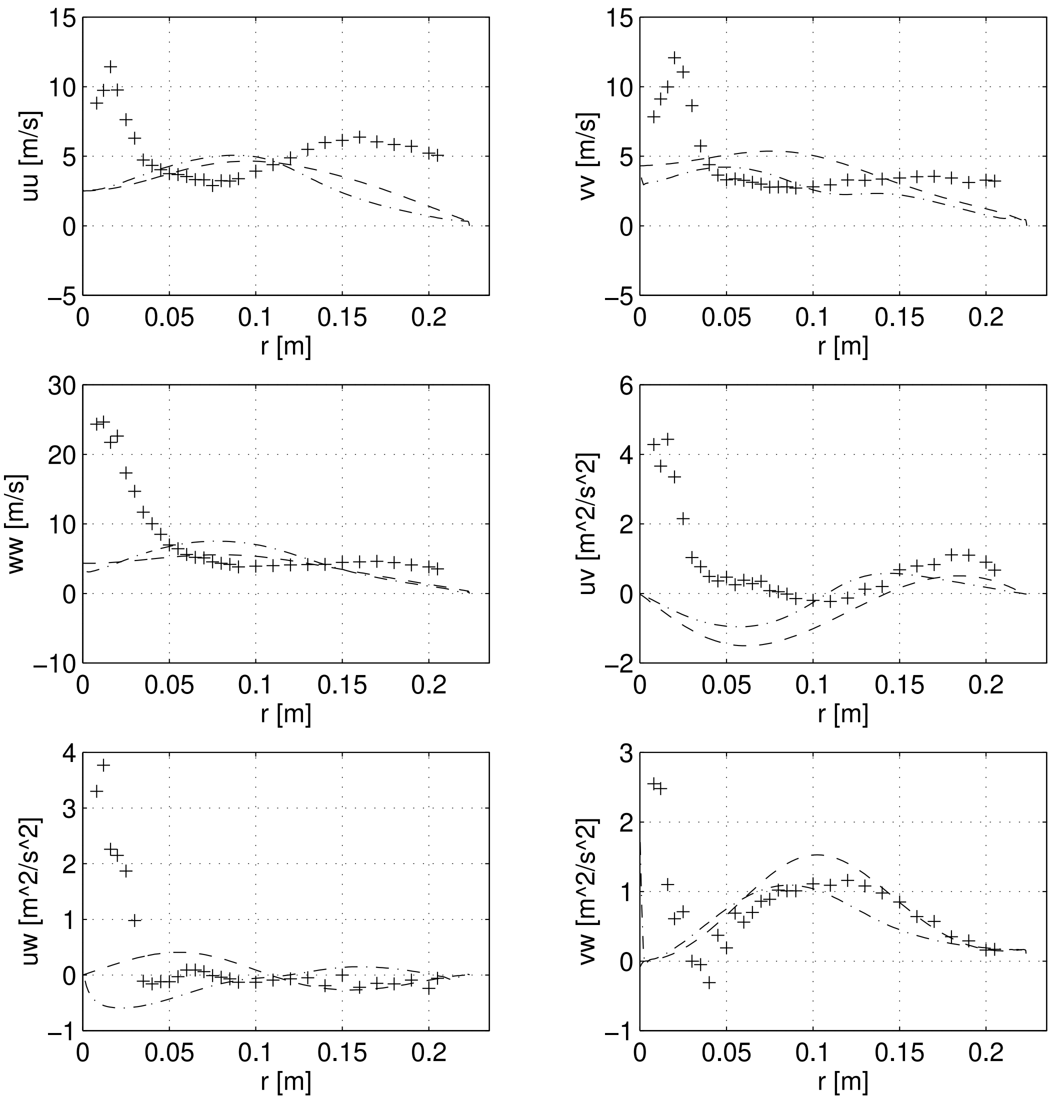

Figure 57: 220 mm downstream, $-\cdot-$non-linear $k-\omega$, $---k-\omega$, $+$ Holzöpfel[13]

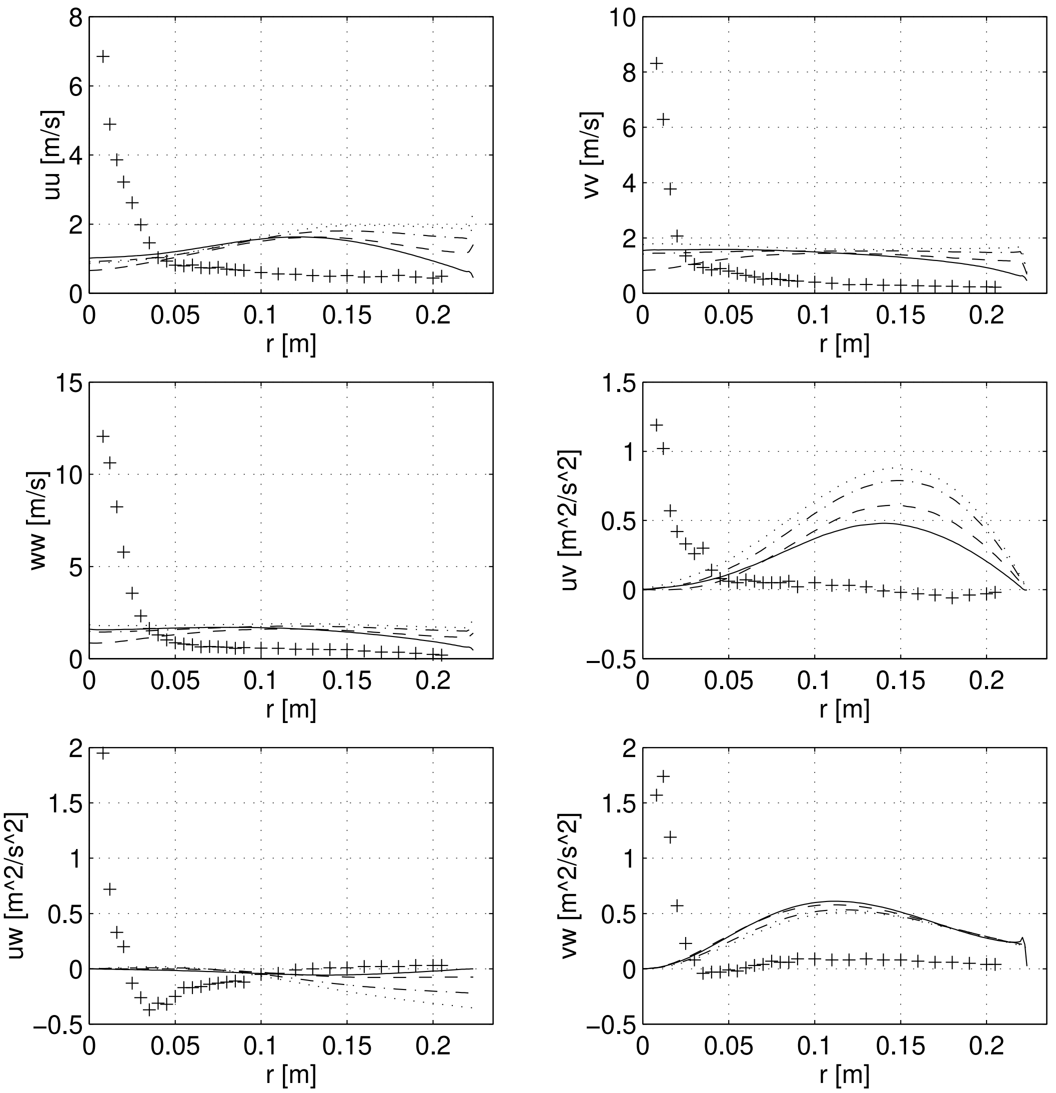

Figure 58: 520 mm downstream, $\cdots k-\epsilon$, $-\cdot- k-\epsilon \quad RN=0.002$, $--- k-\epsilon \quad RN=0.008$, — $k-\epsilon$ with wallfcn, + Holzöpfel[13]

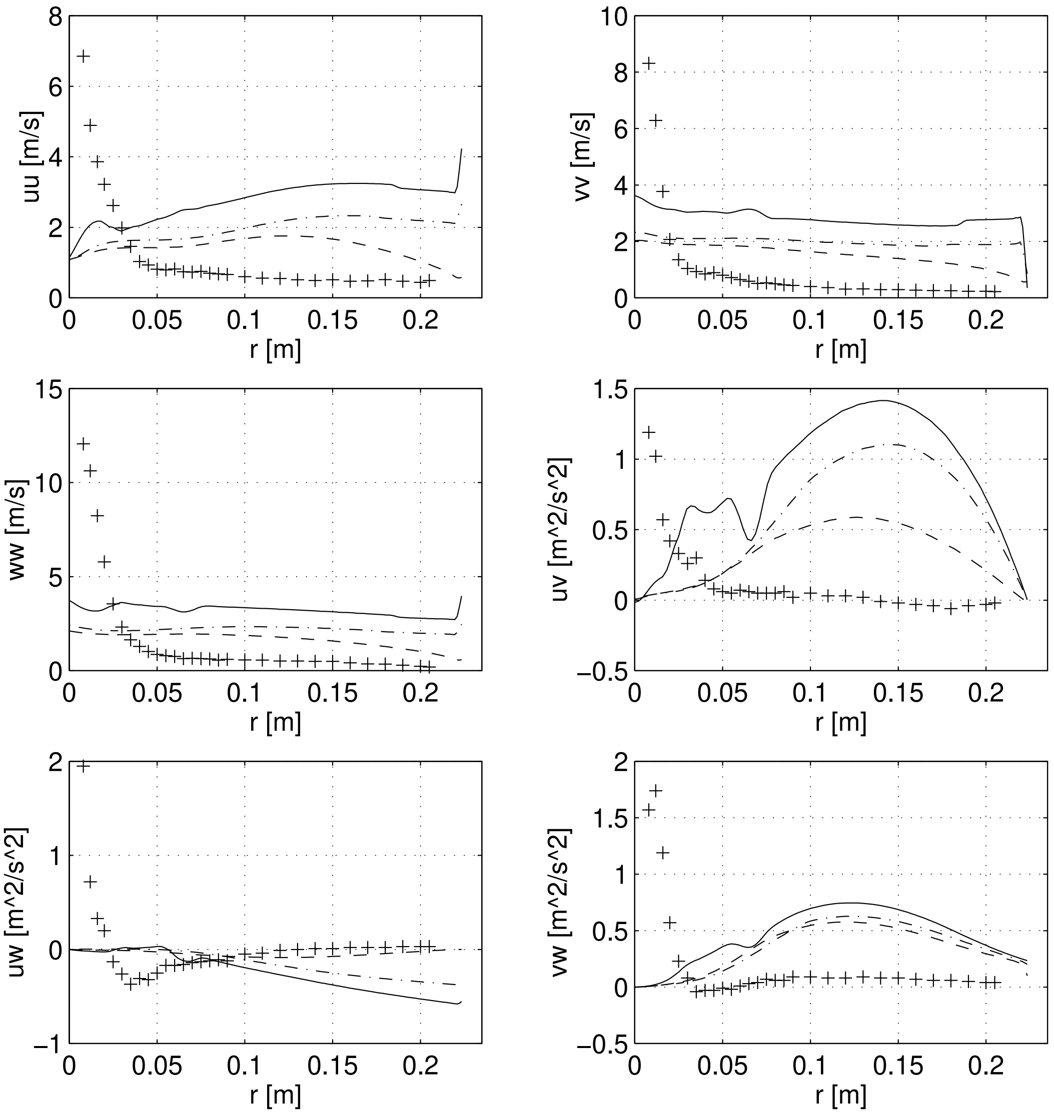

Figure 59: 520 mm downstream, $-\cdot- RNG-k-\epsilon$, $---RNG-k-\epsilon$ with wallfcns, — $RNG-k-\epsilon$ with swirl mod., + Holzöpfel[13]

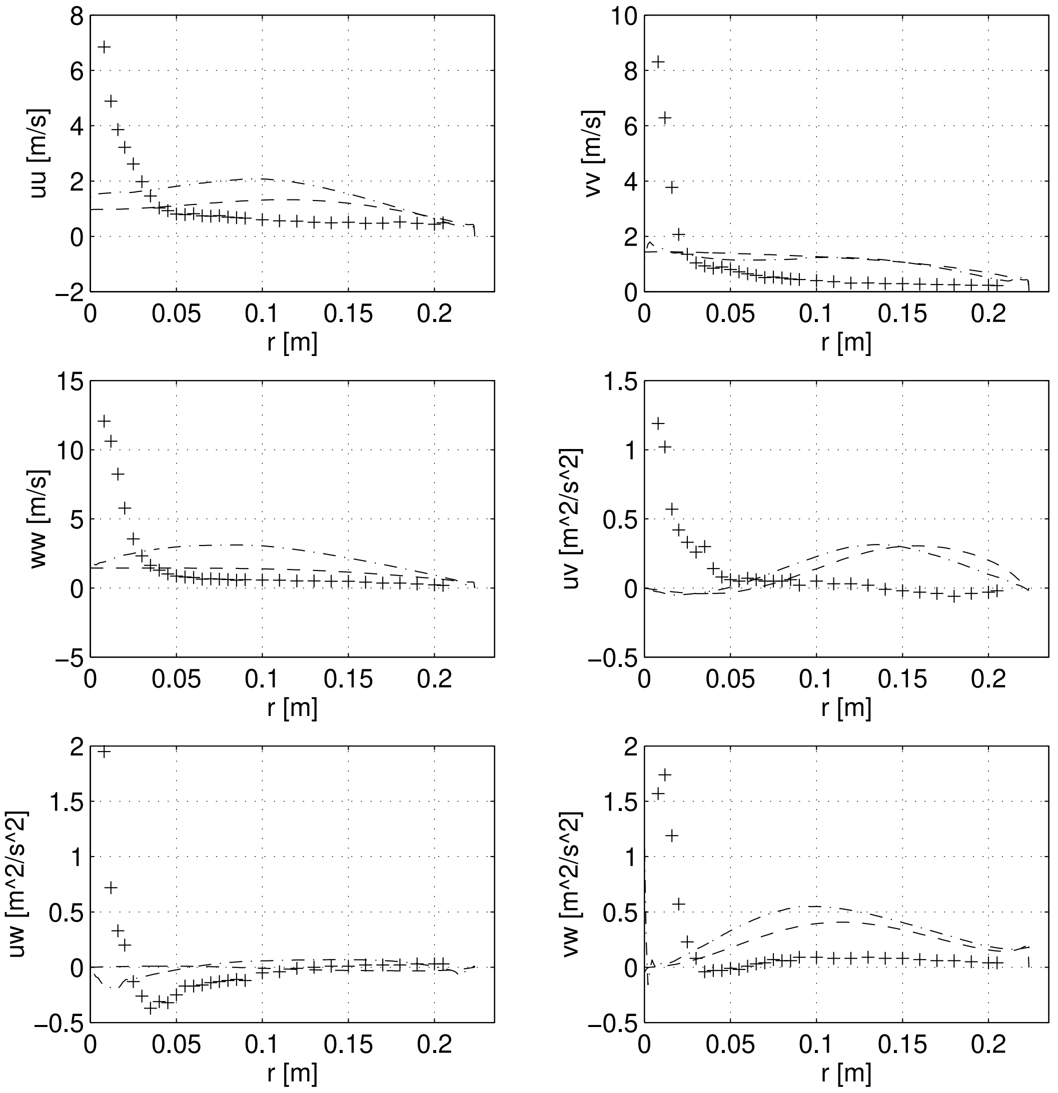

Figure 60: 520 mm downstream, $-\cdot-$non-linear $k-\omega$, $---k-\omega$, + Holzöpfel[13]